CENTRO DE INVESTIGACIÓN Y DE ESTUDIOS AVANZADOS DEL INSTITUTO POLITÉCNICO NACIONAL

UNIDAD ZACATENCO

PROGRAMA DE NANOCIENCIAS Y NANOTECNOLOGÍA

Funcionales Híbridos de Rango-Separado en la Teoría del Funcional de la Densidad Auxiliar

T E S I S

Que presenta

Francisco Antonio Delesma Díaz

Para obtener el grado de

DOCTOR EN CIENCIAS

En la especialidad de

NANOCIENCIAS Y NANOTECNOLOGÍA

Directores de la Tesis: Dr. Andreas M. Köster
Dra. Patrizia Calaminici

Ciudad de México   Marzo, 2020

CENTER FOR RESEARCH AND ADVANCED STUDIES

OF THE NATIONAL POLYTECHNIC INSTITUTE

ZACATENCO CAMPUS

NANOSCIENCE AND NANOTECHNOLOGY PROGRAM

Range-Separated Hybrid Functionals

in Auxiliary Density Functional Theory

T H E S I S

Presented by

Francisco Antonio Delesma Díaz

To obtain the degree of

DOCTOR IN SCIENCE

In the specialty of

IN NANOSCIENCE AND NANOTECHNOLOGY

Thesis advisors: Dr. Andreas M. Köster
Dr. Patrizia Calaminici

Mexico City   March, 2020

Acknowledgment

I gratefully acknowledge Dr. Andreas Köster and Dr. Patrizia Calaminici for their guidance and dedication to carry out the research work presented in this thesis. Also, for giving me their friendship.

Many thanks to Dr. Daniel Mejía-Rodríguez for his help in the early stage of this research, also, to Dr. Rogelio I. Delgado-Venegas and M.C. Jesús Naín Pedroza-Montero for the privilege of sharing valuable discussions during the development of this work.

Thanks to all the theoretical chemistry group members. For sharing discussions, good times and a great workplace. Special thanks to Dr. Gerald Geudtner for all the help provided.

I am thankful to Dr. Lars G. M. Pettersson, Dr. José Luis Morales, B.E. José René Gómez-Pérez, B.E. Sonia Margarita Chong-Aréchiga for the excellent collaboration established.

The valuable comments and corrections of the professors in the evaluation committee are also acknowledged, thanks to Dr. Aurelien de la Lande, Dr. Rito Daniel Olguín Melo, Dr. Luis Emilio Orgaz Baqué and Dr. Alberto Marcial Vela Amieva.

Agradezco en español a la familias Delesma y Díaz en Chiapas y Tabasco, gracias por su apoyo y la confianza puesta en mi persona. A la familia Aréchiga-Wong de Mazatán, Chiapas, muchas gracias por la calidez y el apoyo que he obtenido de ustedes. A la familia Citalán-Cruz en la Ciudad de México gracias por su hospitalidad. Agrezco profundamente mi gran amigo Gustavo Andrade y a mi tío Cornelio por alentarme y aconsejarme durante todo este tiempo. Hay una lista interminable de las personas a las que estoy muy agradecido a quienes les haré saber apropiadamente.

Dedicatory

To my parents.

To Magui.

To my siblings.

We live on a island
surrounded by a sea of ignorance.
As our island of knowledge grows,
so does the shore of our ignorance

J.A. Wheeler

Contents

List of Figures

List of Tables

List of Abbreviations

ADFT	Auxiliary density functional theory
ADPT	Auxiliary density pertubation theory
AO	Atomic orbital
aug-cc-pVTZ	Augmented correlation-consistent polarized valence triple-zeta basis
B88	Becke 88 exchange functional
BLYP	Becke, Lee, Yang and Parr functional
B3LYP	Becke, 3-parameter, Lee, Yang and Parr hybrid functional
CAM	Coulomb attenuating method
cc-pVTZ	Correlation-consistent polarized valence triple-zeta basis
CGTO	Cartesian Gaussian type orbital
def2-TZVPP	Triple-zeta valence with double polarization basis
deMon2k	density of Montreal computational chemistry code
DF-DFT	Density fitted density functional theory
DFA	Density functional approximation
EN	Eirola-Nevanlinna
ERI	Electron repulsion integral
GGA	Generalized gradient approximation
GPT	Gaussian product theorem
GTO	Gaussian type orbital
IRC	Intrinsic reaction coordinate
HSE03	Heyd, Scuseria, Ernzerhof functional (2003)
HSE06	Heyd, Scuseria, Ernzerhof functional (2006)
LAPACK	Linear Algebra PACKage
LC	Long-range correction scheme
LCAO	Linear combination of atomic orbital

LCGTO	Linear combination of Gaussian type orbital
LDA	Local density approximation
LMO	Localized molecular orbital
M06-2X	Minnesota meta-hybrid functional (2006)
MAD	Mean absolute deviation
meta-GGA	meta-generalized gradient approximation
MINRES	Minimal residual solver
MO	Molecular orbital
NWChem	Northwest computational Chemistry software package
OEP	Optimized effective potential
PBE	Perdew, Burke and Ernzerhof functional
PBE0	Perdew, Burke and Ernzerhof hybrid functional
QTP	Quantum Theory Project
RAM	Ramdon access memory
RI	Resolution of identity
SCAN	Strongly constrained and appropriately normed meta-GGA
SCF	Self-consistent field
SCP	Self-consistent perturbation theory
TDDFT	Time dependent density functional theory
TED	Truncated eigenvalue decomposition
VWN	Vosko, Wilk and Nusair functional

Resumen

Con el fin de alcanzar calculos de primeros principios a escala nanométrica en esta tesis se presentan la derivación e implementación de la aproximación del ajuste local de la densidad para el potencial de Fock de largo alcance, así como, su uso para realizar cálculos usando funcionales hibrídos de rango-separado en en marco de la teoría del funcional de la densidad auxiliar de densidad ajustada (DF-DFT por sus siglas en inglés) y la teoría del funcional de la densidad auxiliar (ADFT). En particular, las metodologías desarrollada en este trabajo permiten el cálculo del funcional de la densidad de forma rápida y eficiente con una notoria aceleración comparado con las implementaciones de la teoría del funcional de la densidad (DFT) estandar, esto debido a que las expresiones matemáticas obtenidas de la energía y los gradientes estan libre de las integrales de la repulsión electrónica de cuatro-centros, así como, de la integración númerica del producto de funciones. La exactitud y el desempeño de algunos funcionales híbridos de rango-separado, ya sea en cálculos serial o paralelo, son validados, evaluados y discutidos. También se presenta la extensión de la teoría de perturbación de la densidad auxiliar (ADPT) para funcionales híbridos globales y de rango-separado. Las contribuciones alcanzadas en esta tesis abren las puertas para cálculos de grandes sistemas moleculares usando los funcionales hibrido de rango-separado en un tiempo razonable. Más aún, estos permiten cálculos rápidos de las propiedades moleculares de sistemas nanométricos. Algunas aplicaciones de problemas actuales son seleccionadas para mostrar el potencial de la metodología presentada en esta tesis.

Abstract

To facilitate first principle nanoscale calculations, this thesis presents the derivation and implementation of the local density fitting long-range Fock exchange approach that can be used for the computation of range-separated hybrid functionals within density-fitted density functional theory (DF-DFT) and auxiliary density functional theory (ADFT). In particular, the latter methodology permits fast and efficient density functional calculations with remarkable speed-ups compared to standard density functional implementations because the obtained energy and gradient expressions are free of four-center integrals and the numerical integration of product functions. The accuracy and performance, either serial or parallel, of selected range-separated hybrid functionals are validated, benchmarked and discussed. The extension of auxiliary density perturbation theory (ADPT) to global and range-separated hybrid functionals is also presented. The contributions achieved in this thesis open an avenue for large-scale all-electron calculations with range-separated hybrid functionals in reasonable time. Moreover, they enable the fast computation of molecular properties of nanosystems. Selected applications to state-of-the-art problems exhibit the potential of the here presented methodology.

Introduction and Objectives

Nanotechnology, in which matter is studied and manipulated at the nanometric length scale, is currently attracting enormous attention. It has, and will continue to have, considerable impact on our lives as well as on the global economy. The main reason for the fascination in nanometer-sized structures are their interesting properties, which are fundamentally different to those of bulk materials. Surface effects and quantum mechanical effects arise in nanostructures due to their large surface-to-volume ratio and reduced dimensions comparable to the electron wavelength, respectively. Such effects are utilized to produce new improved materials, as well as novel medical, optical and electronic devices. Applications of some of these nanostructured materials are shown in Table 1.

Table 1: Nanostructured materials and their common applications in nanoscience and nanotechnology.

Nanostructured material	Application
Nanoparticles/Nanoclusters	Catalysis
Quantum dots	Sensors
Nano films	Adhesive and coating
Biological structures	Medicine/Drug delivery system
Nanocomposites	Material ceramics
Nano porous materials	Information storage
Nanowires	Magnetic, electrical and optical devices
Nanotubes	Separation technologies

At the present state of our scientific understanding, quantum mechanics plays a fundamental role in the description of natural phenomena. In fact, phenomena that occur on a very small scale cannot be explained without the framework of quantum physics. The bulk properties of materials often change dramatically when reduced to nanoscale dimensions. Starting roughly

at 100 nanometers, materials go through a size barrier below which quantization of energy for the electrons in solids becomes relevant. The bulk properties of any material, which are merely the average of all the quantum forces affecting all the atoms that make up the material, start to suffer from these so-called quantum size effects. As things get smaller and smaller, eventually a point is reached where averaging no longer works. From here on we have to deal with the specific behavior of individual atoms or molecules resulting in effects that are very different from those in macroscopic aggregates.

The applicability of quantum mechanics to study the properties of matter at the level of nuclear, atomic, molecular and condensed matter physics is both universal and so far unquestionable. In the last decades, Density Functional Theory (DFT) [1, 2] and its complementary time-dependent DFT (TDDFT) [3] have emerged as the leading electronic structure modeling techniques and are widely used in fields as diverse as chemistry, physic, material science and electronic engineering. The basic assumption in the quantum mechanical DFT description of many electron systems is the expression of the energy as a functional of the density. The ability to model the atomic and electronic structure of molecules, liquids, nanoparticles and solids has become a key part of modern research. However, almost all simulations are limited to a relatively small number of particles, here atoms. The principle reason for this restriction is the high order scaling of the computational demand with the number of electrons in the system. As an example, standard Kohn-Sham DFT implementations scale formally quartic in computational time and quadratic in memory with respect to the number of electrons. To overcome this computational bottleneck, density fitted Kohn-Sham DFT (DF-DFT) and auxiliary density functional theory (ADFT) have been established in recent years as computationally efficient alternatives to conventional four-center electron repulsion integral (ERI) Kohn-Sham implementations [4, 5], allowing the routine calculation of systems with hundreds of atoms and thousands of electrons [6, 7].

DFT, in form of the local density (LDA) and generalized gradient (GGA) approximation, is widely used to determine properties of a large variety of molecular systems including energies and thermodynamic data, geometries, charge distributions, vibrations, electric and magnetic response properties as well as reaction pathways, to name a few. However, several problems have been found in practical calculations. For example, LDA and GGA severely

overestimate the polarizabilities in certain conjugated systems. This overestimation increases with the size of the molecular systems and becomes even worse for hyperpolarizabilities of elongated conjugated molecules [8, 9]. Here the failure of LDA and GGA is catastrophic. For similar reasons, TDDFT calculations poorly estimate Rydberg excitations and their oscillator strengths [10–12] and often fail completely for charge-transfer excitations [13].

To overcome the errors in the calculation of polarizabilities and hyperpolarizabilities, a new class of density functional approximations (DFAs) has been proposed. These functionals, known as long-range corrected (LC) functionals, include a growing fraction of exact exchange as the distance between electrons increases. They are able to improve the agreement between calculated DFT and experimental polarizabilities and hyperpolarizabilities [14–17]. Moreover, Tawada et al. [18] applied the LC scheme within TDDFT and found that this methodology yields accurate Rydberg excitation energies within 0.5 eV of the measured experimental values, recovering oscillator strengths of the same order as the experimental values. Further improvements to LC functional, like the Coulomb attenuated method and the screening Coulomb method, generated a new family of DFAs named range-separated hybrid functionals.

One of the successes of the range-separated hybrid functionals are molecular polarizability calculations. Although, coupled-cluster (CC) [19] calculations are in principle more reliable for polarizabilities, their unfavorable computational scaling with system size makes them only partially suitable for systematic polarizability studies [20]. Thus, range-separated hybrid calculations of polarizabilities are the current state-of-art for systematic polarizability and hyperpolarizability studies. In fact, their results are closed to corresponding well-correlated CC calculations. For these calculations, the solution of the coupled-perturbed Kohn-Sham (CPKS) [21, 22] equations is needed. Due to the large dimension of the corresponding equation system, iterative solvers must be employed. As a result, the solution of the CPKS equation system can become computationally very demanding or even impossible, e.g. for nanosystems. A computationally more efficient alternative to CPKS is auxiliary density perturbation theory (ADPT), which recently has been successfully used to calculate response properties of nanosystems such as static and dynamic polarizabilities [23–26]. An important milestone in this respect was the development and implementation of a robust, iterative solver

for the non-symmetric, indefinite, ADPT equation system based on the Eirola-Nevanlinna (EN) algorithm in deMon2k. This iterative methodology, combined with an efficient parallel implementation, permitted the calculation of response properties on systems with more than 14,000 basis functions and 30,000 auxiliary functions in very reasonable times. So far these property calculations are limited to LDA and GGA and, therefore, are not generally suitable for the calculation of static and dynamic polarizabilities and hyperpolarizabilities of nanosystems. Following these argumentations it is rather straightforward to assume that the implementation of range-separated hybrid functionals into the DF-DFT and ADFT methodology, followed by a corresponding extension of ADPT, will permit fist-principle calculations of non-linear optical properties of nanosystems. This thesis aims to contribute to this long-term goal.

The first challenge in this respect is the efficient calculation of Fock or modified Fock exchange needed for global and range-separated hybrid DFAs. Because this step includes four-center ERI calculations, it usually represents the computational bottleneck for large-scale global and range-separated hybrid calculations. This is particularly true if the variational fitting of the Coulomb potential [27–29] is used and the obtained auxiliary density is employed for the calculation of the local or semilocal DFA, i.e. ADFT calculations are performed. Despite impressive progress in the scaling reduction of Fock calculations for increasing system sizes by algorithms like ONX [30] and LinK [31], its unfavorable $\mathcal{O}(N_{bas}^4)$ scaling with respect to the basis set size, N_{bas}, has for long time hampered the implementation of efficient linear combination of Gaussian type orbital hybrid DFT calculations. More recently, this bottleneck has been overcome by density fitting [32–35] algorithms for the Fock potential. These algorithms build on earlier resolution of the identity approaches [36–38] but improve their computational performance by efficient molecular orbital localizations. In this work the recently developed variational fitting of the Fock potential [34] is extended to the modified Fock potential needed for range-separated hybrid DFAs. Here we present the development and implementation of the new basic integrals used in the corresponding two- and three-center ERI recurrence relations [39–41]. Based on these ERI algorithms energy and gradient expressions for four-center ERI free range-separated hybrid DFAs are derived and their serial and parallel implementation and performance are discussed. It is shown that this approach

permits range-separated hybrid energy and gradient calculations of nanosystems.

After this milestone was reached, we focused on the extension of ADPT for global and range-separated hybrid functionals. To this end, we derive here new ADPT working equations, now including Fock exchange, and propose a corresponding modifications of the underlying EN algorithm. With a first proof-of-principle serial implementation we validate these new ADPT working equations in this thesis.

Whereas ADFT hybrid functional calculations of standard enthalpies of formation are already extensively validated, corresponding validations for activation and reaction enthalpies are less abundant. To the best of our knowledge attention has so far only been focused on reactions contained in the HTBH38/08 and NHTBH38/08 databases [42]. For these simple reactions the activation energies obtained from ADFT hybrid functional calculations compare very favorably with those from conventional four-center ERI Kohn-Sham calculations [43]. These results have encouraged us to investigate the accuracy of ADFT hybrid calculations for activation and reaction energies of more complex reactions. To this end, we followed Houk et al. [44] who provided a general protocol, based on critically evaluated experimental activation barriers for hydrocarbon pericyclic reactions, to test the performance of different levels of theory for the calculations of these barriers. Thus, the direct comparison of the experimental data with the calculated ones can be used to evaluate the performance of different DFAs. To bridge to nanostructures, we extended these studies to the [4+2] Diels-Alder cycloaddition of cyclopentadiene to C_{60}. Here we found that the accuracies of DFAs for small pericyclic reactions is not straightforward scalable to reactions involving nanosystems. This underlines the need for more extensive studies of classical reactions of nanosystems. Such calculations are facilitated by the methodological developments presented in this thesis.

Recently, the core-level shifts for the ESCA molecule were calculated by Van den Bossche et al. [45] and the importance of including exact exchange in the DFT functional for accurate results was pointed out. Here, we extend this work by evaluating the performance of various DFAs for standard full core-hole final-state calculations. As an alternative to the full core-hole calculations we also apply the chemically intuitive Z+1 approximation, i.e. replacing the core-ionized carbon by nitrogen and computing the total energy for the positively charged system. Our results shows that the Z+1 approximation yields similar results as the full

core-hole calculations and also benefits from the use of global and range-separated hybrid functionals.

Although the focus of this thesis is on the development of new methodologies for large scale calculations, it is important to note that several of the here presented benchmark calculations include molecules that contain hundreds of atoms and posses nanometric extensions. For example, the linear alkane chain $C_{150}H_{302}$ has 452 atoms and a length of approximately 18 nm, the $(\alpha$-D-glucose$)_{16}$ amylose fragment which consist of 339 atoms, has a diameter of around 1 nm and a length of 5 nm. The systematic study of these large molecular systems has been possible due to the new algorithms for hybrid ADFT and DF-DFT methodologies developed in this thesis.

The thesis is organized as follows. In chapter one the foundations of density functional theory starting from elementary quantum mechanics are outlined. In chapter two the variational fitting of the Coulomb and Fock potentials are derived and their use in the DF-DFT and ADFT methodologies are described. Chapter three details the range-separation methodology and its use in density functional approximations. The implementation, validation and benchmarking of range-separated hybrid functionals, in the framework of DF-DFT and ADFT, both in serial and parallel, are presented in chapter four. Selected applications of the here developed algorithms for the calculation of thermodynamic properties, electric response properties and X-ray photoemission spectroscopy are presented in chapter five. Final conclusions and perspectives of this work are drawn in the last chapter.

Objetives

The main objective of this thesis is to incorporate the range-separation methodology into the framework auxiliary density functional theory (ADFT) and auxiliary density perturbation theory (ADPT). Such an implementation will permit reliable energy and property calculations of nanosystems. To achieve this main objective the following milestones must be reached:

- Derivation of variational fitted long-range Fock exchange energy.

- Serial and parallel implementation of the long-range Foch exchange potential.

- Serial and parallel implementation of the long-range Fock exchange energy gradients.

- Serial and parallel implementation of range-separated hybrid functionals.

- Validation and benchmarking of the new range-separated hybrid functional implementation.

- Derivation of ADPT working equations for range-separated hybrid functionals.

- Validation of the new ADPT working equations.

Related Work

Selected results from this thesis were reported in the following publications:

1. F.A. Delesma, G. Geudtner, D. Mejía-Rodríguez; P. Calaminici, A.M. Köster, Range-separated hybrid functionals with variational fitted exact exchange, *J. Chem. Theory Comput.* **18**, 5608–5616 (2018) DOI: 10.1021/acs.jctc.8b00436

2. J.R. Gómez-Pérez, F.A. Delesma, P. Calaminici, A.M. Köster, Accuracy of Auxiliary Density Functional Theory Hybrid Calculations for Activation and Reaction Enthalpies of Pericyclic Reactions, *J. Mol. Model.* **24**, 223 (2018).
DOI: 10.1007/s00894-018-3759-8

3. F.A. Delesma, M. van den Bossche, H. Grönbeck, P. Calaminici, A.M. Köster, L.G.M. Pettersson, A Chemical View on X-ray Photoelectron Spectroscopy: the ESCA Molecule and Surface-to-Bulk XPS Shifts, *ChemPhysChem* **18**, 169–174 (2018)
DOI: 10.1002/cphc.201701135

4. J.N. Pedroza-Montero, F.A. Delesma, R.I. Delgado-Venegas, P. Calaminici, A.M. Köster, Static and dynamic polarizabilities of oligothiophenes, *Theor. Chem. Acc.* **135**, 230 (2016) DOI 10.1007/s00214-016-1984-8

They were also presented at national and international conferences, in the following talks:

1. F.A. Delesma, J.R. Gómez-Pérez, L.G.M. Pettersson, P. Calaminici, A.M. Köster, Range-Separated Hybrid Functionals, The deMon developer workshop 2018, June 5-10, Guadalajara, Jalisco, México. (2018).

2. F.A. Delesma, P. Calaminici, A.M. Köster, Range-Separated Hybrid Functionals, The deMon developer workshop 2017, May 5-10, Calgary, Alberta, Canada. (2017).

3. F.A. Delesma, Implementation of range-separated hybrid functionals in deMon2k, El seminario de Física y Cómputo de la Facultad de Ciencias de la UNAM, September 14, Mexico City, México. (2016)

and posters:

1. F.A. Delesma, P. Calaminici, A.M. Köster, L.G.M. Pettersson, X-ray photoelectron spectroscopy: bridging experiment and theory, The deMon developer workshop 2018, June 5-10, Guadalajara, Jalisco, México. (2018).

2. F.A. Delesma, P. Calaminici, A.M. Köster, L.G.M. Pettersson, X-ray photoelectron spectroscopy: Bridging experiment and theory, Segundo simposio interdisciplinario de materiales, Capitulo estudiantil CINVESTAV-Zacatenco de la Sociedad Mexicana de Materiales. 10 de Marzo de 2018

3. F.A. Delesma, J.N. Pedroza-Montero, P. Calaminici, A.M. Köster, Static and dynamic polarizabilities of oligothiophenes, Primer simposio interdisciplinario de materiales, Capitulo estudiantil CINVESTAV-Zacatenco de la Sociedad Mexicana de Materiales. 10 de Marzo de 2017

The algorithms presented in this PhD thesis are now part of the deMon2k software.

A.M. Koster, G. Geudtner, A. Alvarez-Ibarra, P. Calaminici, M.E. Casida, J. Carmona-Espindola, **F.A. Delesma**, R. Delgado-Venegas, V.D. Dominguez, R. Flores-Moreno, G.U. Gamboa, A. Goursot, T. Heine, A. Ipatov, A. de la Lande, F. Janetzko, J. Martin del Campo, N. Pedroza Montero, L.G.M. Pettersson, D. Mejia-Rodriguez, J. Reveles, J. Vasquez-Perez, A. Vela, B. Zuniga-Gutierrez and D.R. Salahub, *deMon2k*, The International deMon Developers, Cinvestav, México, version 6.0.8, 2019

Density Functional Theory

In this introductory chapter we will review some of the fundamental aspects of electronic structure theory in order to lay the foundations for the theoretical discussion of density functional theory presented in later parts of this thesis.

1.1 Quantum Mechanics

Classical mechanics is inadequate for describing systems composed of small particles such as electrons, atoms, and molecules. What is missing in classical mechanics is the description of wavelike properties for matter that predominates the physics of small particles. Quantum mechanics takes into account the wavelike properties of matter when solving mechanical problems. The mathematics and laws of quantum mechanics that must be used to explain wavelike properties cause a dramatic change in the way mechanical problems must be solved. In quantum mechanics, to yield something that can be observed experimentally, the *expectation value* of the measurable quantity is calculated. The expectation value can be interpreted as the average value of the measurable quantity that we would obtain from a large number of measurements or the simultaneous measurement of a large number of entities.

In quantum mechanics a system is described completely by the function $\Psi(\mathbf{r}, t)$ that depends on the coordinates of the particle, $\mathbf{r}$, and the time, t (for simplicity we ignore spin dependency here). This function is called the *wave function* or *state function*. In order to represent a viable physical state, the wave function must be single-valued, continuous and square-integrable. In the probabilistic interpretation of Born [46], the wave function of a single particle system is a function whose modulus $|\Psi(\mathbf{r}, t)|^2$ describes the *probability density*, i.e.

the probability to detect a particle at the position $\mathbf{r}$ as a result of a measurement at the time t. For a single particle quantum system the probability density function must satisfy the normalization condition

$$\langle\Psi|\Psi\rangle = \int \Psi^*(\mathbf{r},t)\Psi(\mathbf{r},t)d\mathbf{r} = 1 \tag{1.1}$$

In equation (1.1) Dirac's *bracket* notation has been used, where the *state* of a system is represented by a *ket* vector, $|\Psi\rangle$, which belongs to a Hilbert space [47], $\mathscr{H}$. For each *ket* there exist a *bra* vector, $\langle\Psi|$, which belongs to the dual of $\mathscr{H}$, $\mathscr{H}^*$, and represents its complex conjugate. Associated to Hilbert space exist operators, $\hat{A}$, such that their application on a *ket* yields a *ket* again

$$\hat{A}|\Psi\rangle = |\Phi\rangle \qquad\qquad \Psi, \Phi \in \mathscr{H} \tag{1.2}$$

The physical meaning of an operator in quantum mechanics is given by the definition of an *observable* (any measurable property of the system, i.e. position, momentum, energy, etc.). Quantum mechanics postulates that for each *observable* there exist an associate linear Hermitian operator, $\hat{A}$, and the only quantities that can ever be observed are the eigenvalues, a, that satisfy the eigenvalue equation

$$\hat{A}|\Psi\rangle = a|\Psi\rangle \tag{1.3}$$

If a system is in a state described by a normalized wave function Ψ, then the average value of the observable corresponding to $\hat{A}$ is given by

$$\langle A\rangle = \langle\Psi|\hat{A}|\Psi\rangle \tag{1.4}$$

The evolution of a quantum system is determined by the time dependent Schrödinger equation

$$\hat{H}\Psi(\mathbf{r},t) = i\hbar\frac{\partial}{\partial t}\Psi(\mathbf{r},t) \tag{1.5}$$

In Eq.(1.5) $\hat{H}$ is the Hamilton operator, i the imaginary unit and $\hbar$ the reduced Plank constant, $h/2\pi$. To solve the time-depended Schrödinger the method of variable separation is used. Therefore, we make the following ansatz

$$\Psi(\mathbf{r},t) = \Psi(\mathbf{r})X(t) \tag{1.6}$$

By inserting Eq. (1.6) into Eq. (1.5) it follows

$$
\begin{aligned}
\hat{H}\Psi(\mathbf{r})X(t) &= i\hbar\frac{\partial}{\partial t}\Psi(\mathbf{r})X(t) \\
X(t)\hat{H}\Psi(\mathbf{r}) &= i\hbar\Psi(\mathbf{r})\frac{\partial}{\partial t}X(t) \\
\frac{1}{\Psi(\mathbf{r})}\hat{H}\Psi(\mathbf{r}) &= \frac{i\hbar}{X(t)}\frac{\partial X(t)}{\partial t}
\end{aligned}
\tag{1.7}
$$

Since the right hand side in Eq. (1.7) only depends on t and the left hand side only on $\mathbf{r}$, both sides must be equal to a constant, which we name $\mathcal{E}$. Solving the right hand side of Eq. (1.7),

$$
\frac{i\hbar}{X(t)}\frac{\partial X(t)}{\partial t} = \mathcal{E}
\tag{1.8}
$$

yields

$$
X(t) = e^{-i\mathcal{E}t/\hbar}
\tag{1.9}
$$

By inserting Eq. (1.8) into Eq. (1.7) and multiplying from the left with $\Psi(\mathbf{r})$ we obtain

$$
\hat{H}\Psi(\mathbf{r}) = \mathcal{E}\Psi(\mathbf{r})
\tag{1.10}
$$

Eq. (1.10) is known as the time-independent Schrödinger equation. For a given potential $\hat{V}(\mathbf{r})$ in the Hamilton operator, $\hat{H}$, there are many solutions $\{\Psi_n\}$ with corresponding eigenvalue $\{\mathcal{E}_n\}$. Thus, a general solution for Eq. (1.5) is given by

$$
\Psi_n(\mathbf{r}, t) = \Psi_n(\mathbf{r})\, e^{-i\mathcal{E}_n t/\hbar}
\tag{1.11}
$$

For a particular state, e.g. $\Psi_1(\mathbf{r})$, the probability density becomes time independent

$$
|\Psi_1(\mathbf{r}, t)|^2 = |\Psi_1(\mathbf{r})|^2\, |e^{-i\mathcal{E}_1 t/\hbar}|^2 = |\Psi_1(\mathbf{r})|^2
\tag{1.12}
$$

These states are called *stationary states*. Therefore, a stationary state is a standing wave that oscillates with an overall complex phase factor, where its oscillation frequency is equal to its energy divided by $\hbar$.

Since stationary states form a complete orthonormal basis, we may write

$$
\Psi(\mathbf{r}, t) = \sum_{n=1}^{\infty} c_n \Psi_n(\mathbf{r}) e^{-i\mathcal{E}_n t/\hbar}
\tag{1.13}
$$

where the c_n are expansion coefficients. Thus, for the expectation value of the Hamilton operator follows

$$
\begin{aligned}
\langle \hat{H} \rangle &= \langle \Psi | \hat{H} | \Psi \rangle = \int \Psi(\mathbf{r}, t)^* \hat{H} \Psi(\mathbf{r}, t) \, d\mathbf{r} \\
&= \sum_{n,n'}^{\infty} \int c_n^* \Psi_n^*(\mathbf{r}) \, e^{i \mathcal{E}_n t / \hbar} \, \hat{H} \, c_{n'} \, \Psi_{n'}(\mathbf{r}) \, e^{-i \mathcal{E}_{n'} t / \hbar} \, d\mathbf{r} \\
&= \sum_{n,n'}^{\infty} c_n^* \, c_{n'} \, e^{i(\mathcal{E}_n - \mathcal{E}_{n'}) t / \hbar} \int \Psi_n^*(\mathbf{r}) \hat{H} \Psi_{n'}(\mathbf{r}) \, d\mathbf{r} \\
&= \sum_{n,n'}^{\infty} c_n^* \, c_{n'} \, e^{i(\mathcal{E}_n - \mathcal{E}_{n'}) t / \hbar} \, \delta_{n,n'} \, \mathcal{E}_n \\
&= \sum_{n=1}^{\infty} |c_n|^2 \, \mathcal{E}_n
\end{aligned}
\tag{1.14}
$$

As Eq. (1.14) shows, the expectation value of the Hamilton operator is time-independent. This is the quantum version of energy conservation.

1.2 Born-Oppenheimer Approximation

A molecular quantum system is characterized by the number of nuclei and electrons, M and N, respectively. The atomic mass of nucleus A is M_A and its charge Z_A. Therefore, the non-relativistic Hamilton operator for an isolated molecule (from now on all equations presented in this thesis are written using *atomic units*) is given by

$$
\begin{aligned}
\hat{H} &= -\frac{1}{2} \sum_i^N \nabla_i^2 - \sum_A^M \frac{1}{2M_A} \nabla_A^2 - \sum_A \sum_i \frac{Z_A}{|\mathbf{r}_i - \mathbf{A}|} + \sum_i^N \sum_{j>i}^N \frac{1}{|\mathbf{r}_i - \mathbf{r}_j|} + \\
&\quad \sum_A^M \sum_{B>A}^M \frac{Z_A Z_B}{|\mathbf{A} - \mathbf{B}|}
\end{aligned}
\tag{1.15}
$$

In Eq (1.15) the $\mathbf{r}_i$ and $\mathbf{r}_j$ denote the spatial coordinates of the electrons i and j, respectively. The position vectors $\mathbf{A}$ and $\mathbf{B}$ denote the spatial coordinates of the corresponding nuclei. The physical meaning of the terms on the right-hand-side of Eq. (1.15) are:
The kinetic energy of the N electrons,

$$
\hat{T}_e = -\frac{1}{2} \sum_i^N \nabla_i^2,
\tag{1.16}
$$

the kinetic energy of the M nuclei,

$$\hat{T}_n = -\sum_A^M \frac{1}{2M_A} \nabla_A^2,$$ (1.17)

the electrostatic attraction between the N electrons and the M nuclei,

$$\hat{V}_{ne} = -\sum_A^M \sum_i^N \frac{Z_A}{|\mathbf{r}_i - \mathbf{A}|},$$ (1.18)

the electrostatic repulsion between the electrons,

$$\hat{V}_{ee} = \sum_i^N \sum_{j>i}^N \frac{1}{|\mathbf{r}_i - \mathbf{r}_j|},$$ (1.19)

and the electrostatic repulsion between the nuclei,

$$\hat{V}_{nn} = \sum_A^M \sum_{B>A}^M \frac{Z_A Z_B}{|\mathbf{A} - \mathbf{B}|}.$$ (1.20)

Therefore, it is customary to express Eq. (1.15) as:

$$\hat{H} = \hat{T}_e + \hat{T}_n + \hat{V}_{ne} + \hat{V}_{ee} + \hat{V}_{nn}$$ (1.21)

The wave functions associated to the Hamilton operator of Eq (1.21) must be a function of the electron and nuclear coordinates. Thus, the concept of a molecular structure is not existing at this level of approximation. To overcomer this conceptional drawback an approximate separation of the differential equation based upon the very large difference between the mass of an electron and the masses of the nuclei is suggested by the following ansatz

$$\Psi(\mathbf{r}, \mathbf{R}) = \Psi_{\mathbf{R}}(\mathbf{r})\Theta(\mathbf{R})$$ (1.22)

In Eq. (1.22) $\Psi_{\mathbf{R}}(\mathbf{r})$ is the electronic wave function which is parametrically dependent from the nuclear configuration. The corresponding nuclear wave function is denoted by $\Theta(\mathbf{R})$. Due to the mass difference the nuclear components of the wave function are much more localized in space. Thus, only a small space around the nuclei must be considered. Only here the nuclear wave function is significantly different from zero. In this small region the nuclear wave function rises much more steeply than the electronic one, which means that

$\nabla_A \Theta(\mathbf{R}) \gg \nabla_A \Psi_{\mathbf{R}}(\mathbf{r})$. Thus, we may approximate according to Born and Oppenheimer [48]

$$
\begin{aligned}
\hat{T}_n \Psi(\mathbf{r}, \mathbf{R}) &= \hat{T}_n \Psi_{\mathbf{R}}(\mathbf{r}) \Theta(\mathbf{R}) \\
&= -\sum_A^M \frac{1}{2M_A} \left[\Psi_{\mathbf{R}}(\mathbf{r}) \nabla_A^2 \Theta(\mathbf{R}) + \Theta(\mathbf{R}) \nabla_A^2 \Psi_{\mathbf{R}}(\mathbf{r}) + 2 \nabla_A \Psi_{\mathbf{R}}(\mathbf{r}) \cdot \nabla_A \Theta(\mathbf{R}) \right] \\
&\approx -\sum_A^M \frac{1}{2M_A} \Psi_{\mathbf{R}}(\mathbf{r}) \nabla_A^2 \Theta(\mathbf{R}) = \Psi_{\mathbf{R}}(\mathbf{r}) \hat{T}_n \Theta(\mathbf{R})
\end{aligned}
\tag{1.23}
$$

Substitution of Eq. (1.22) into Eq. (1.10), considering the approximation obtained in Eq. (1.23) and, employing once again the method of variable separation yields

$$
\begin{aligned}
\left[\hat{T}_e + \hat{T}_n + \hat{V}_{ne} + \hat{V}_{ee} + \hat{V}_{nn} \right] \Psi_{\mathbf{R}}(\mathbf{r}) \Theta(\mathbf{R}) &= \mathcal{E} \, \Psi_{\mathbf{R}}(\mathbf{r}) \Theta(\mathbf{R}) \\
\Psi_{\mathbf{R}}(\mathbf{r}) \, \hat{T}_n \Theta(\mathbf{R}) + \Theta(\mathbf{R}) \left[\hat{T}_e + \hat{V}_{ne} + \hat{V}_{ee} + \hat{V}_{nn} \right] \Psi_{\mathbf{R}}(\mathbf{r}) &= \mathcal{E} \, \Psi_{\mathbf{R}}(\mathbf{r}) \Theta(\mathbf{R}) \\
\frac{\left[\hat{T}_e + \hat{V}_{ne} + \hat{V}_{ee} + \hat{V}_{nn} \right] \Psi_{\mathbf{R}}(\mathbf{r})}{\Psi_{\mathbf{R}}(\mathbf{r})} &= \mathcal{E} - \frac{\hat{T}_n \Theta(\mathbf{R})}{\Theta(\mathbf{R})}
\end{aligned}
\tag{1.24}
$$

Because the left hand side of Eq. (1.24) can only be a function of $\mathbf{R}$, we write

$$
\begin{aligned}
\frac{\left[\hat{T}_e + \hat{V}_{ne} + \hat{V}_{ee} + \hat{V}_{nn} \right] \Psi_{\mathbf{R}}(\mathbf{r})}{\Psi_{\mathbf{R}}(\mathbf{r})} &= E(\mathbf{R}) \\
\left[\hat{T}_e + \hat{V}_{ne} + \hat{V}_{ee} + \hat{V}_{nn} \right] \Psi_{\mathbf{R}}(\mathbf{r}) &= E(\mathbf{R}) \, \Psi_{\mathbf{R}}(\mathbf{r})
\end{aligned}
\tag{1.25}
$$

and

$$
\hat{T}_n \Theta(\mathbf{R}) + E(\mathbf{R}) \, \Theta(\mathbf{R}) = \mathcal{E} \, \Theta(\mathbf{R})
\tag{1.26}
$$

Eq (1.25) and (1.26) are called the electronic and nuclear Schrödinger equations, respectively. Classically, their separation by the Born-Oppenheimer approximation is often justified by stating that the heavy nuclei move more slowly than the light electrons. In quantum mechanics, a physical system remains in its instantaneous eigenstate if a given perturbation is acting on it slowly enough and if it is smaller than the corresponding eigenvalue gap. This quantum mechanical concept is known as the adiabatic theorem. Under these conditions the nuclear configuration can be assumed frozen for the solution of the electronic Schrödinger equation, Eq. (1.25). The corresponding electronic Hamilton operator is given by

$$
\hat{H}_e = \hat{T}_e + \hat{V}_{ee} + \hat{V}_{ne} + \hat{V}_{nn}
\tag{1.27}
$$

Thus, we can rewrite Eq. (1.25) as

$$\hat{H}_e \Psi_{\mathbf{R}}(\mathbf{r}) = E(\mathbf{R})\Psi_{\mathbf{R}}(\mathbf{r}) \qquad (1.28)$$

Eq (1.28) is also known as the *clamped-nuclei* Schrödinger equation. To avoid cluttering of notation we will drop from now on the subscripts on the electronic Hamilton operator and wave function. Note that the nuclear repulsion energy, $\hat{V}_{nn}$, was incorporated into the electronic Hamilton operator because it contributes to the potential energy surface (PES) and will be calculated by classical electrostatic repulsion between nuclear point charges. The solutions of the electronic Schrödinger equation form a set of orthogonalized eigenfunctions, $\Psi(\mathbf{r})$, with corresponding eigenvalues $E(\mathbf{R})$. In this thesis we focus on the energetically lowest solution of this set, i.e. the ground state solution. The usual procedure to solve Eq. (1.26) is then to solve first Eq. (1.28) for the electronic ground state and substitute its energy value into the nuclear Schrödinger equation where it serves as potential for the nuclei. In Born-Oppenheimer molecular dynamics (BOMD) the motions of the nuclei on the PES are solved by Newtonian mechanics. As a result, an on-the-fly propagation of molecular systems becomes possible.

1.3 Hohenberg-Kohn Theorems

The probabilistic interpretation of the electronic wave function leads directly to the (one particle) electron density $\rho(\mathbf{r})$. For a many electron system, neglecting spin dependencies, the one-electron density is defined as the multiple integral over all spatial electron coordinates, except one

$$\rho(\mathbf{r}) = N \int \cdots \int |\Psi(\mathbf{r}, \mathbf{r}_2, \ldots, \mathbf{r}_N)|^2 d\mathbf{r}_2 \ldots \mathbf{r}_N \qquad (1.29)$$

The electron density, $\rho(\mathbf{r})$, determines the probability of finding an electron at position $\mathbf{r}$, while the other $N-1$ electrons having arbitrary positions. For a system with N electrons the electronic wave function depends on $3N$ spatial coordinates while the corresponding electronic density depends only on 3 spatial coordinates. This dramatic reduction of spatial coordinates has stimulated the research on density functional models over many decades since the early thirties of the last century.

For obtaining information about the electronic structure, the earliest attempts to use the electron density rather than the wave function were made when quantum mechanics was emerging itself. The works of Thomas in 1926 [49] and Fermi in 1928 [50] pursued independently the same idea, namely to construct a model in which the kinetic and potential energy was expressed directly as a function of the electron density. Further works by Dirac [51] as well as Wigner and Seitz [52] improved the model by introducing a local expression for the exchange potential. However, in 1962, the Teller theorem [53] showed the intrinsic instability of the Thomas-Fermi model to describe molecular binding. Nevertheless, Slater successfully introduced the idea of approximating the non-local Fock exchange potential in the Hartree-Fock method by an average local potential based on the free-electron gas model. The result was an exchange potential expressed solely in terms of $\rho(\mathbf{r})$. Further development led to the so-called $X\alpha$ methodology of Slater and Johnson [54], which suggested that a theory based on $\rho(\mathbf{r})$ instead of $\Psi(\mathbf{r})$ seemed feasible. However, it was not before 1964 that a rigorous proof for the validity of the substitution of the wave function by the density as basic quantity was provided by Hohenberg and Kohn [1] with the following theorem:

First Hohenberg-Kohn theorem: *The external potential $v(\mathbf{r})$ is determined, within a trivial additive constant, by the electron density, $\rho(\mathbf{r})$.*

To proof this theorem, we assume, for a non-degenerate ground state, that two different external potentials, $v(\mathbf{r})$ and $v'(\mathbf{r})$, arise from the same electronic density $\rho(\mathbf{r})$. This implies two different Hamilton operators, $\hat{H}$ and $\hat{H}'$ with the corresponding different wave functions $\Psi(\mathbf{r})$ and $\Psi'(\mathbf{r})$. Taking $\Psi'(\mathbf{r})$ as a trial wave-function for $\hat{H}$ and using the variational principle yields

$$
\begin{aligned}
E_0 = \langle \Psi | \hat{H} | \Psi \rangle \;\; &< \;\; \langle \Psi' | \hat{H} | \Psi' \rangle = \langle \Psi' | \hat{H}' | \Psi' \rangle + \langle \Psi' | \hat{H} - \hat{H}' | \Psi' \rangle \\
&< \;\; E_0' + \int \rho(r)[v(\mathbf{r}) - v'(\mathbf{r})]d\mathbf{r}
\end{aligned}
\tag{1.30}
$$

Similar if we take $\Psi(\mathbf{r})$ as trial wave function for $\hat{H}'$

$$
\begin{aligned}
E_0' = \langle \Psi' | \hat{H}' | \Psi' \rangle \;\; &< \;\; \langle \Psi | \hat{H}' | \Psi \rangle = \langle \Psi | \hat{H} | \Psi \rangle - \langle \Psi | \hat{H} - \hat{H}' | \Psi \rangle \\
&< \;\; E_0 - \int \rho(r)[v(\mathbf{r}) - v'(\mathbf{r})]d\mathbf{r}
\end{aligned}
\tag{1.31}
$$

Adding the inequalities (1.30) and (1.31) leads to the contradiction

$$E_0 + E_0' < E_0' + E_0 \tag{1.32}$$

From this contradiction Hohenberg and Kohn concluded that the ground state density uniquely determines the external potential $v(\mathbf{r})$. Because the ground state density and its potential, $v(\mathbf{r})$, determine uniquely the Hamiltonian, $\hat{H}$, which yields the energy by solving the Schödinger equation, the following mapping can be established

$$\rho(\mathbf{r}) \leftrightarrow N, v(\mathbf{r}) \leftrightarrow \hat{H} \rightarrow \Psi[\rho] \rightarrow E[\rho] \tag{1.33}$$

A consequence of the one-to-one mapping between the electronic density $\rho(\mathbf{r})$ and the external potential $v(\mathbf{r})$ is that the wave function and the energy are functionals of the density. Hence all ground state properties of a system are entirely determined by the ground state electronic density. The variational energy principle can be used to obtain the ground state density as proven by the second Hohenberg-Kohn theorem.

Second Hohenberg-Kohn theorem: *The ground state density $\rho(\mathbf{r})$ can be determined from the ground state energy functional $E[\rho]$ via the variational principle.*

To proof this theorem we write the ground state energy, E_0, as a functional of the density

$$E_0 = E[\rho_0] = \langle \Psi[\rho_0] | \hat{H} | \Psi[\rho_0] \rangle \tag{1.34}$$

For a trial density $\rho_t(\mathbf{r})$ such that,

$$\int \rho_t(\mathbf{r}) d\mathbf{r} = N \quad \text{and} \quad \rho_t(\mathbf{r}) \geq 0 \,\forall\, \mathbf{r} \tag{1.35}$$

follows from the first Hohenberg-Kohn theorem the corresponding external potential $v_t(\mathbf{r})$. With $v_t(\mathbf{r})$ and $\rho_t(\mathbf{r})$ the Hamilton operator can be constructed and the trial wave function $\psi_t[\rho_t]$ is obtained from the Schrödinger equation. Based on the variational energy principle follows that

$$E[\rho_t] = \langle \Psi[\rho_t] | \hat{H} | \Psi[\rho_t] \rangle \geq E[\rho_0] = E_0 \tag{1.36}$$

The equality holds only when the trial density, $\rho_t(\mathbf{r})$, equals the true ground state density, $\rho_0(\mathbf{r})$, of the system.

1.4   Kohn-Sham Method

The energy functional $E[\rho]$ of the system can be written in terms of the external potential, $v(\mathbf{r})$, in the following way

$$E[\rho] = F[\rho] + \int \rho(\mathbf{r})v(\mathbf{r})d\mathbf{r} \tag{1.37}$$

Here $F[\rho]$ denotes the universal (unknow) Hohenberg-Kohn functional. In this context, universal means that the functional has the same form for all systems, i.e. atoms, molecules and solids. The ground state density $\rho_0(\mathbf{r})$ can be obtained by minimization of the functional $E[\rho]$ given in Eq. (1.37). The universal Hohenberg-Kohn functional $F[\rho]$ can be split into two terms, which are the kinetic energy functional $T[\rho]$ and a functional that contains all electron-electron interactions $v_{ee}[\rho]$

$$F[\rho] = T[\rho] + v_{ee}[\rho] \tag{1.38}$$

Here $v_{ee}[\rho]$ collects the classical Coulomb interaction and all the quantum interactions between the electrons. Thus

$$v_{ee} = \frac{1}{2} \iint \frac{\rho(\mathbf{r})\rho(\mathbf{r}')}{|\mathbf{r} - \mathbf{r}'|} d\mathbf{r} \, d\mathbf{r}' + v_{nc}[\rho] \tag{1.39}$$

The only part of Eq. (1.38) that is known is the classical Coulomb interaction between the electrons. The expressions for $T[\rho]$ and $v_{nc}[\rho]$ are unknown. But in 1965, Kohn and Sham provided a way to overcome this limitation with a trade-off between simplicity and accuracy [2] by the introduction of orbitals from a non-interacting reference system. For a non-interacting system the exact wave function is the antisymmetric product of orbitals $\psi_i(\mathbf{r})$, i.e. the Slater determinant of these orbitals. Therefore, the corresponding expression for the kinetic energy of the non-interacting Kohn-Sham system is just the sum od the single-particle kinetic energies given by

$$T_{\text{KS}}[\rho] = -\frac{1}{2}\langle \Psi[\rho]|\nabla^2|\Psi[\rho]\rangle = -\frac{1}{2}\sum_i^N \langle \psi_i|\nabla^2|\psi_i\rangle \tag{1.40}$$

Similar, the electronic density of the non interacting system, that must match by construction with the density of the real interacting system, can be calculated from these Kohn-Sham orbitals as

$$\rho(\mathbf{r}) = \sum_i^N |\psi_i(\mathbf{r})|^2 \tag{1.41}$$

Using the explicit expression for the classical Coulomb interaction between the electrons the energy functional of the interacting system can now be written as

$$E[\rho] = T_{\mathrm{KS}}[\rho] + \int v(\mathbf{r})\rho(\mathbf{r})d\mathbf{r} + \frac{1}{2}\iint \frac{\rho(\mathbf{r})\rho(\mathbf{r}')}{|\mathbf{r} - \mathbf{r}'|}d\mathbf{r}\,d\mathbf{r}' + E_{xc}[\rho] \tag{1.42}$$

All unknown energy functional components are collected in the exchange-correlation energy functional $E_{xc}[\rho]$. At this point, it is important to note that this functional is universal, i.e. it is the same functional for an atom, a molecule, and a solid. The orbitals of the non-interacting reference system are obtained by minimizing Eq. (1.42) imposing the restrictions of orbital orthonormality

$$\langle \psi_i | \psi_j \rangle = \delta_{ij} \tag{1.43}$$

As a result, we obtain single particle Kohn-Sham equations of the form

$$\left(-\frac{1}{2}\nabla^2 + v(\mathbf{r}) + \int \frac{\rho(\mathbf{r}')}{|\mathbf{r} - \mathbf{r}'|}d\mathbf{r}' + v_{xc}[\rho(\mathbf{r})] \right) \psi_i(\mathbf{r}) = \epsilon_i \psi_i(\mathbf{r}) \tag{1.44}$$

Here $v_{xc}[\rho(\mathbf{r})]$ is the exchange-correlation potential, which is defined as the functional derivative of the exchange-correlation energy

$$v_{xc}[\rho(\mathbf{r})] \equiv \frac{\delta E_{xc}[\rho]}{\delta \rho(\mathbf{r})} \tag{1.45}$$

In the Kohn-Sham method the exact form of the exchange-correlation functional $E_{xc}[\rho]$ is unknown. In fact, the quality of a DFT calculation employing the Kohn-Sham method is determined by the quality of the approximations for the exchange-correlation energy functional. Fundamental to these approximations is the universal nature of the exchange-correlation functional. The local density approximation (LDA) combines the Dirac exchange functional [51] with local correlation functional fits for the homogeneous electron gas. A popular choice is the local correlation from Vosko, Wilk and Nussair (VWN) [55]. A more sophisticated approach represents the generalized gradient approximation (GGA). Popular GGA functionals, besides others, are the ones from Becke, Lee, Yang, and Parr (BLYP) [56, 57] and the most popular Perdew, Burke, and Ernzerhof (PBE) [58].

More accurate functionals for the calculation of the exchange-correlation energy and potential include not only the density and its gradient, but also the kinetic energy density of the non-interacting system and/or the laplacian of the density [59, 60]. These functionals are called meta-GGA (m-GGA) functionals. Most recently a strongly constrained and appropriately normed (SCAN) m-GGA functional [61] was proposed that show improvements over other (semi-)local functionals and could be as accurate as a fully nonlocal hybrid functional with decreased computational cost in plane waves and traditional DFT [62].

Another class of functionals represent the so-called hybrid functionals. They combine LDA or GGA exchange with Fock exchange. Many of these functionals are highly parametrized and, therefore, yield excellent results for a certain class of molecules or properties. Unfortunately, this parametrization destroys the universal nature of these functionals. Therefore, care must be taken when applying these functionals to molecules outside their parametrization space. To overcome this problem range-separated hybrid functionals have been introduced. They solve some problems of the global hybrid functionals but others still remain.

An alternative approach represents the so-called exact exchange approach in which a Fock type exchange is calculated in the framework of the non-interactive system. If the corresponding potential is obtained in local form, e.g. by the optimized effective potential (OEP) method, a systematic extension of the Kohn-Sham approach can be pursued [63–68]. Unfortunately, the OEP method introduces a $(\mathcal{O}^5)$ scaling which renders this approach inefficient. Common to all hybrid and OEP approaches is the need to calculate Fock exchange, either in its global or range-separated form. Once a specific exchange-correlation functional is selected the Kohn-Sham equations have to be solved iteratively. They can be casted in matrix form yielding Roothaan-Hall like equations systems, similar to the Hartree-Fock equations. The details of such a formulation are given in the following sections.

1.5 Linear Combination of Gaussian Type Orbital Approximation

In the linear combination of atomic orbital (LCAO) DFT ansatz the Kohn-Sham molecular orbitals (MOs) are expanded into atomic orbitals as

$$\psi_i(\mathbf{r}) = \sum_\mu c_{\mu i} \mu(\mathbf{r}) \tag{1.46}$$

Here $\mu(\mathbf{r})$ denotes an atomic orbital, often also named a basis function. The sum in Eq. (1.46) runs over all atomic orbitals used in the calculation. In the linear combination of Gaussian type orbital (LCGTO) ansatz contracted (Cartesian) Gaussian type orbital (CGTO) are used as basis functions. The unnormalized form of such an orbital is given by

$$\mu(\mathbf{r}) = (x - A_x)^{a_x}\,(y - A_y)^{a_y}\,(z - A_z)^{a_z} \sum_k^K d_k e^{\zeta_k(\mathbf{r}-\mathbf{A})^2} \tag{1.47}$$

This function is uniquely defined by its atomic center $\mathbf{A}$, its angular momentum index $\mathbf{a} = (a_x, a_y, a_z)$, the degree of contraction K, the contraction coefficients d_k and the orbital exponents ζ_k. It should be noted that the contraction coefficients, orbital exponents and angular moment index remain constant during the electronic structure calculation. For a closed-shell system the LCGTO expansion of the electronic density is given by

$$\rho(\mathbf{r}) = 2\sum_i^{occ} \sum_{\mu,\nu} c_{\mu i} c_{\nu i} \mu(\mathbf{r})\nu(\mathbf{r}) = \sum_{\mu,\nu} P_{\mu\nu}\mu(\mathbf{r})\nu(\mathbf{r}) \tag{1.48}$$

Here $P_{\mu\nu}$ is an element of the density matrix, which, for a closed-shell system, is defined as

$$P_{\mu\nu} = 2\sum_i^{occ} c_{\mu i} c_{\nu i} \tag{1.49}$$

The upper sum limit, occ, in Eq. (1.49) denotes the number of doubly occupied molecular orbitals (MOs) in the system. Taking into account the LCGTO expansion for the Kohn-Sham orbitals, Eq. (1.46), and the electronic density, Eq. (1.48), the Kohn-Sham energy expression (1.42) takes the following form

$$E = \sum_{\mu,\nu} P_{\mu\nu} H_{\mu\nu} + \frac{1}{2}\sum_{\mu,\nu}\sum_{\sigma,\tau} P_{\mu\nu} P_{\sigma\tau} \langle \mu\nu \| \sigma\tau \rangle + E_{xc}[\rho] \tag{1.50}$$

The first term in Eq. (1.50) represents the one-electron energy, often named the core energy. $H_{\mu\nu}$ is an element of the mono-electronic Hamiltonian, that contains the kinetic and nuclear attraction energy of the electrons

$$H_{\mu\nu} = -\frac{1}{2}\langle \mu | \nabla^2 | \nu \rangle - \sum_A \left\langle \mu \left| \frac{Z_A}{\|\mathbf{r} - \mathbf{A}\|} \right| \nu \right\rangle \tag{1.51}$$

The second term in Eq. (1.50) is the Coulomb repulsion energy between the electrons. The here used four-center electron repulsion integral (ERI) short hand notation has the form

$$\langle \mu\nu \| \sigma\tau \rangle = \iint \frac{\mu(\mathbf{r})\nu(\mathbf{r})\sigma(\mathbf{r}')\tau(\mathbf{r}')}{|\mathbf{r} - \mathbf{r}'|} d\mathbf{r}\, d\mathbf{r}' \tag{1.52}$$

In this ERI notation the double vertical bar represents the two-electron operator

$$\| \equiv \frac{1}{|\mathbf{r} - \mathbf{r}'|} \tag{1.53}$$

It also separates the orbitals with the electronic coordinate $\mathbf{r}$ from the orbitals with the electronic coordinate $\mathbf{r}'$.

The third term in Eq. (1.50), the exchange-correlation energy, accounts for three distinct physical effects: The exchange energy E_x corrects the spurious self-interaction of one electron with itself and also contains the effects of the Pauli exclusion principle. The correlation energy $E_c = E_{xc} - E_x$ accounts for the effects of Coulomb and kinetic energy correlations upon the many-electron wave function [69].

The derivation of the Kohn-Sham equations starts with the minimization of the energy expression (1.50), under the constrain of molecular orbital orthonormality, Eq. (1.43). In the LCGTO method Eq. (1.43) is expanded as

$$\langle \psi_i | \psi_j \rangle = \sum_{\mu,\nu} c_{\mu i} \langle \mu | \nu \rangle c_{\nu j} = \sum_{\mu,\nu} c_{\mu i} S_{\mu\nu} c_{\nu j} = \delta_{ij} \tag{1.54}$$

Here $S_{\mu\nu}$ are elements of the atomic overlap matrix. The Lagrange function for the energy minimization is then defined by the following expression

$$L = E - 2\sum_{i,j} \lambda_{ij} \left(\sum_{\mu,\nu} c_{\mu i} S_{\mu\nu} c_{\nu j} - \delta_{ij} \right) \tag{1.55}$$

The energy E is given by Eq. (1.50). The variation of the Lagrange function with respect to MO coefficients yields

$$\frac{\partial L}{\partial c_{\mu i}} = 4\sum_{\nu} \left(H_{\mu\nu} + \sum_{\sigma,\tau} P_{\sigma\tau} \langle \sigma\tau \| \mu\nu \rangle + \langle \mu | v_{xc}[\rho] | \nu \rangle \right) c_{\nu i} - 4\sum_{j}\sum_{\nu} S_{\mu\nu} c_{\nu j} \lambda_{ji} \tag{1.56}$$

In the above equation, the variation of the exchange-correlation energy with respect to the MO coefficient, $c_{\mu i}$, was expanded as

$$\frac{\partial E_{xc}[\rho]}{\partial c_{\mu i}} = \int \frac{\delta E_{xc}[\rho]}{\delta \rho(\mathbf{r})} \frac{\partial \rho(\mathbf{r})}{\partial c_{\mu i}} d\mathbf{r} = 4 \sum_{\nu} \langle \mu | v_{xc}[\rho] | \nu \rangle \, c_{\nu i} \tag{1.57}$$

At this point of the derivation it is convenient to introduce the Kohn-Sham matrix elements that are given by the variation of the electronic energy with respect to the density matrix

$$K_{\mu\nu} \equiv \frac{\partial E}{\partial P_{\mu\nu}} = H_{\mu\nu} + \sum_{\sigma,\tau} P_{\sigma\tau} \langle \sigma\tau \| \mu\nu \rangle + \langle \mu | v_{xc}[\rho] | \nu \rangle. \tag{1.58}$$

Substitution of Eq. (1.58) into the Eq. (1.56) yields

$$\sum_{\nu} K_{\mu\nu} c_{\nu i} = \sum_{j} \sum_{\nu} S_{\mu\nu} c_{\nu j} \lambda_{ji} \quad \forall\, \mu; \forall\, i \tag{1.59}$$

which is a generalized eigenvalue equation. By collecting all equations into a single matrix equation we find

$$\mathbf{Kc} = \mathbf{Sc\lambda} \tag{1.60}$$

This set of equations has a closed resemblance to the Roothaan-Hall equation [70, 71]. Here **c** is a square matrix composed from the occupied and virtual molecular orbital coefficients. Because the electronic density is invariant under unitary transformations of the occupied molecular orbitals, it is possible to choose a set of molecular orbitals for which the off-diagonal undefined Lagrange multipliers, λ_{ji}, are zero. Thus, we can use a molecular orbital representation $\mathbf{cU}$, where $\mathbf{U}$ is an orthogonal transformation matrix, such that $\mathbf{U\lambda U}^T$ becomes a diagonal matrix

$$\mathbf{KcU} = \mathbf{ScU} \underbrace{\mathbf{U}^T \mathbf{\lambda U}}_{\varepsilon} \tag{1.61}$$

These transformed molecular orbitals are called canonical, and they are solutions of the *canonical* Kohn-Sham equations,

$$\mathbf{Kc} = \mathbf{Sc\varepsilon} \tag{1.62}$$

To proceed we now analyze the computational complexity for solving the Kohn-Sham equations: The computation of the core Hamiltonian, $H_{\mu\nu}$, scales formally quadratic, $\mathcal{O}(N_{bas}^2)$,

with the number of basis functions, N_{bas}. The second term in the Kohn-Sham matrix, Eq. (1.58), represents the Coulomb repulsion energy between the electrons. It introduces a formal $\mathcal{O}(N_{bas}^4)$ scaling. For the calculation of the exchange-correlation energy a numerical integration has to be performed. This integration scales formally as $\mathcal{O}(N_{bas}^2 \times N_{grd})$, where N_{grd} is the number of grid points necessary for the numerical integration. From this discussion follows, that the calculation of the Coulomb repulsion energy and exchange-correlation energy in the Kohn-Sham matrix represent the computationally most demanding tasks.

Auxiliary Density Functional Theory

To overcome the computational bottleneck associated to the calculation of the four-center ERIs the so-called variational fitting of the Coulomb potential is introduced. We now describe this methodology as implemented in the LCGTO-DFT program deMon2k [72].

2.1 Variational Fitting of the Coulomb Potential

The variational fitting of the Coulomb potential as introduced by Dunlap and coworkers [27, 28] is a popular technique to reduce the formal scaling for the computation of the two electron Coulomb repulsion energy. It was inspired by a previous work from Sambe and Felton [73]. This approach became available more than 30 years ago in the deMon-KS program [74]. It also is equivalent with the so-called truncated resolution of identity (RI) [36–38] for Coulomb integrals used in other programs.

The variational Coulomb energy fitting, is based on the minimization of the following second order energy error

$$\epsilon_2^{\mathrm{H}} = \iint \frac{[\rho(\mathbf{r}) - \tilde{\rho}(\mathbf{r})][\rho(\mathbf{r}') - \tilde{\rho}(\mathbf{r}')]}{|\mathbf{r} - \mathbf{r}'|} \, d\mathbf{r} \, d\mathbf{r}'. \tag{2.1}$$

Here, we introduce the approximated electronic density which is often called the auxiliary density, $\tilde{\rho}(\mathbf{r})$. It is calculated as a linear combination of auxiliary functions

$$\tilde{\rho}(\mathbf{r}) = \sum_{\bar{k}} x_{\bar{k}} \bar{k}(\mathbf{r}) \tag{2.2}$$

In deMon2k primitive Hermite Gaussian functions, indicated by a bar, are used in this expansion. An unnormalized primitive Hermite Gaussian auxiliary function, located on atom

A with exponent $\zeta_{\bar{k}}$, has the form

$$\bar{k}(\mathbf{r}) = \left(\frac{\partial}{\partial A_x}\right)^{\bar{k}_x} \left(\frac{\partial}{\partial A_y}\right)^{\bar{k}_y} \left(\frac{\partial}{\partial A_z}\right)^{\bar{k}_z} e^{-\zeta_{\bar{k}}(\mathbf{r}-\mathbf{A})^2} \tag{2.3}$$

In deMon2k the auxiliary functions are grouped into s, spd and $spdfg$ sets. The exponents are shared within each of these sets. Thus, a spd auxiliary function set contains ten functions, namely one s, three p and six d functions. Also, the auxiliary functions are normalized with respect to the Coulomb norm.

Since ϵ_2^{H} is positive semi-definite [75] the following inequality holds

$$\begin{aligned}
\epsilon_2^{\mathrm{H}} &= \frac{1}{2}\langle\rho-\tilde{\rho}\|\rho-\tilde{\rho}\rangle \geq 0 \\
&= \frac{1}{2}\langle\rho\|\rho-\tilde{\rho}\rangle - \frac{1}{2}\langle\tilde{\rho}\|\rho-\tilde{\rho}\rangle \geq 0 \\
&= \frac{1}{2}\langle\rho\|\rho\rangle - \frac{1}{2}\langle\rho\|\tilde{\rho}\rangle - \frac{1}{2}\langle\tilde{\rho}\|\rho\rangle + \frac{1}{2}\langle\tilde{\rho}\|\tilde{\rho}\rangle \geq 0 \\
&= \frac{1}{2}\langle\rho\|\rho\rangle - \langle\rho\|\tilde{\rho}\rangle + \frac{1}{2}\langle\tilde{\rho}\|\tilde{\rho}\rangle \geq 0
\end{aligned} \tag{2.4}$$

Therefore,

$$\frac{1}{2}\langle\rho\|\rho\rangle \geq \langle\rho\|\tilde{\rho}\rangle - \frac{1}{2}\langle\tilde{\rho}\|\tilde{\rho}\rangle \tag{2.5}$$

Eq. (2.5) shows that the minimization of the error will produce a maximization of the approximated Coulomb energy. Employing the LCGTO expansion for $\rho(\mathbf{r})$ and $\tilde{\rho}(\mathbf{r})$ yields the following expression,

$$\frac{1}{2}\sum_{\mu,\nu}\sum_{\sigma,\tau} P_{\mu\nu}P_{\sigma\tau}\langle\mu\nu\|\sigma\tau\rangle \geq \sum_{\mu,\nu}\sum_{\bar{k}} P_{\mu\nu}\langle\mu\nu\|\bar{k}\rangle x_{\bar{k}} - \frac{1}{2}\sum_{\bar{k},\bar{l}} x_{\bar{k}}\langle\bar{k}\|\bar{l}\rangle x_{\bar{l}} \tag{2.6}$$

With this inequality an approximated SCF energy, which is based on Eq. (1.50), can be formulated as

$$E = \sum_{\mu,\nu} P_{\mu\nu}H_{\mu\nu} + \sum_{\mu,\nu}\sum_{\bar{k}} P_{\mu\nu}\langle\mu\nu\|\bar{k}\rangle x_{\bar{k}} - \frac{1}{2}\sum_{\bar{k},\bar{l}} x_{\bar{k}}\langle\bar{k}\|\bar{l}\rangle x_{\bar{l}} + E_{xc}[\rho] \tag{2.7}$$

In the context of deMon2k calculations this is often called the BASIS approach [76] because the basis set density, $\rho(\mathbf{r})$, is used for the calculation of the exchange-correlation energy.

Variation of Eq. (2.7) with respect to the density matrix yields the corresponding Kohn-Sham matrix which now includes the variational fitting of the Coulomb potential

$$K_{\mu\nu} \equiv \left(\frac{\partial E}{\partial P_{\mu\nu}} \right)_{x_{\bar{k}}} = H_{\mu\nu} + \sum_{\bar{k}} \langle \mu\nu \| \bar{k} \rangle x_{\bar{k}} + \langle \mu | v_{xc}[\rho] | \nu \rangle \tag{2.8}$$

The fitting coefficients, $x_{\bar{k}}$, are obtained from the minimization of ϵ_2^{H} keeping the density matrix constant

$$\left(\frac{\partial \epsilon_2^{\mathrm{H}}}{\partial x_{\bar{m}}} \right)_{P_{\mu\nu}} = -\sum_{\mu,\nu} P_{\mu\nu} \langle \mu\nu \| \bar{m} \rangle + \sum_{\bar{l}} x_{\bar{l}} \langle \bar{l} \| \bar{m} \rangle \equiv 0 \quad \forall \; \bar{m} \tag{2.9}$$

Thus, the following inhomogeneous equations system is obtained for the determination of the fitting coefficients, collected in the vector $\mathbf{x}$

$$\mathbf{G}\mathbf{x} = \mathbf{J}, \tag{2.10}$$

where the Coulomb matrix elements are defined as,

$$G_{\bar{l}\bar{m}} = \langle \bar{l} \| \bar{m} \rangle \tag{2.11}$$

and the Coulomb vector elements are given by

$$J_{\bar{m}} = \sum_{\mu,\nu} P_{\mu\nu} \langle \mu\nu \| \bar{m} \rangle = \langle \rho \| \bar{m} \rangle \tag{2.12}$$

A straightforward solution can be obtained by the inversion of the Coulomb matrix

$$\mathbf{x} = \mathbf{G}^{-1}\mathbf{J} \tag{2.13}$$

Because the Kohn-Sham density changes in each SCF step the auxiliary density must be fitted in each SCF step, too. For large auxiliary functions sets with high angular momentum functions the direct inversion of $\mathbf{G}$ is numerically unstable. To stabilize the solution of the linear equation system truncated eigenvalue decomposition (TED) [77] is used in deMon2k. This requires the diagonalization of the Coulomb matrix $\mathbf{G}$. For very large systems with tens of thousands of auxiliary functions this diagonalization becomes a computational bottleneck. To avoid this bottleneck an iterative procedures for solving linear equation system based

on the minimal residual method (MINRES) for symmetric indefinite equation systems was recently implemented in deMon2k [78]. This method avoids the explicit diagonalization of $\mathbf{G}$ and, therefore, permits rapid calculations of nanosized macro-molecules with hundreds of atoms on parallel architectures.

2.2 Variational Fitting of the Fock Exchange Potential

The variational potential fitting can be extended to the Fock exchange energy defined as

$$
\begin{aligned}
E_x^{\mathrm{F}} &= -\sum_{i,j}^{\mathrm{occ}} \iint \frac{\psi_i(\mathbf{r})\psi_j(\mathbf{r})\psi_i(\mathbf{r}')\psi_j(\mathbf{r}')}{|\mathbf{r}-\mathbf{r}'|}\, d\mathbf{r}\, d\mathbf{r}' \\
&= -\sum_{i,j}^{\mathrm{occ}} \langle \psi_i\psi_j \| \psi_i\psi_j \rangle \\
&= -\sum_{i,j}^{\mathrm{occ}} \langle \rho_{ij} \| \rho_{ij} \rangle
\end{aligned}
\tag{2.14}
$$

In the framework of Kohn-Sham this energy is also named exact exchange (EXX) if the Kohn-Sham orbitals are used for its calculations. In Eq (2.14) we introduce the orbital transition densities defined as

$$
\rho_{ij}(\mathbf{r}) = \psi_i(\mathbf{r})\psi_j(\mathbf{r}) = \sum_{\mu,\sigma} c_{\mu i} c_{\sigma j} \mu(\mathbf{r})\sigma(\mathbf{r})
\tag{2.15}
$$

Within the LCGTO expansion, Eq. (2.14) transforms to

$$
E_x^{\mathrm{F}} = -\frac{1}{4}\sum_{\mu,\nu}\sum_{\sigma,\tau} P_{\mu\nu}P_{\sigma\tau}\langle\mu\sigma\|\nu\tau\rangle
\tag{2.16}
$$

where we have used the definition of the closed-shell density matrix, Eq. (1.49). The total Hartree-Fock [79] energy employing the variational fitting of the Coulomb potential is given by

$$
E^{\mathrm{HF}} = \sum_{\mu,\nu} P_{\mu\nu}H_{\mu\nu} + \sum_{\mu,\nu}\sum_{\bar{k}} P_{\mu\nu}\langle\mu\nu\|\bar{k}\rangle x_{\bar{k}} - \frac{1}{2}\sum_{\bar{k},\bar{l}} x_{\bar{k}}G_{\bar{k}\bar{l}}x_{\bar{l}} - \frac{1}{4}\sum_{\mu,\nu}\sum_{\sigma,\tau} P_{\mu\nu}P_{\sigma\tau}\langle\mu\sigma\|\nu\tau\rangle \tag{2.17}
$$

There are two main problems with the energy expression given by Eq. (2.17). First, computing the Fock term introduces a formal $\mathcal{O}(N_{bas}^4)$ scaling that renders the approach unsuitable for large systems. Second, the energy is not self-interaction free. The self-interaction appears because the variational fitted Coulomb energy represents a lower bound to the real Coulomb

energy. This difference, albeit small, will make the potential for each particle a little bit too attractive. Similar as for the variational fitting of the Coulomb potential, the orbital product, ρ_{ij}, can be approximated as a linear combination of atom-centered auxiliary functions

$$\tilde{\rho}_{ij}(\mathbf{r}) = \sum_{\bar{k}} x_{\bar{k}ij} \bar{k}(\mathbf{r}) \tag{2.18}$$

The variational fitting of the Fock energy is based on the minimization of the negative-definite error functional

$$\epsilon_2^{\mathrm{F}} = -\sum_{i,j}^{occ} \iint \frac{[\rho_{ij}(\mathbf{r}) - \tilde{\rho}_{ij}(\mathbf{r})][\rho_{ij}(\mathbf{r}') - \tilde{\rho}_{ij}(\mathbf{r}')]}{|\mathbf{r} - \mathbf{r}'|} d\mathbf{r}\, d\mathbf{r}' \tag{2.19}$$

Due to the negative-definite nature of ϵ_2^{F} [80] the following inequality holds

$$\begin{aligned}
\epsilon_2^{\mathrm{F}} &= -\sum_{i,j}^{occ} \langle \rho_{ij} - \tilde{\rho}_{ij} \| \rho_{ij} - \tilde{\rho}_{ij} \rangle \leq 0 \\
&= -\sum_{i,j}^{occ} \left(\langle \rho_{ij} \| \rho_{ij} \rangle + 2\langle \rho_{ij} \| \tilde{\rho}_{ij} \rangle - \langle \tilde{\rho}_{ij} \| \tilde{\rho}_{ij} \rangle \right) \leq 0
\end{aligned} \tag{2.20}$$

Therefore

$$-\sum_{i,j}^{occ} \langle \rho_{ij} \| \rho_{ij} \rangle \leq -2\sum_{i,j}^{occ} \langle \rho_{ij} \| \tilde{\rho}_{ij} \rangle + \sum_{i,j}^{occ} \langle \tilde{\rho}_{ij} \| \tilde{\rho}_{ij} \rangle \tag{2.21}$$

Employing the LCGTO approximation yields

$$E_x^{\mathrm{F}} = -\sum_{i,j}^{occ} \langle \psi_i \psi_j \| \psi_i \psi_j \rangle \leq -2\sum_{i,j}^{occ} \sum_{\bar{k}} \langle \psi_i \psi_j \| \bar{k} \rangle x_{\bar{k}ij} + \sum_{i,j}^{occ} \sum_{\bar{k},\bar{l}} x_{\bar{k}ij} G_{\bar{k}\bar{l}} x_{\bar{l}ij} = \tilde{E}_x^{\mathrm{F}} \tag{2.22}$$

In this case the maximization of the negative fitting error goes along with the minimization of the approximated Fock exchange energy. This suggests that the simultaneous variational fitting of the Coulomb and Fock potentials should benefit from systematic error compensation if the same auxiliary function set is used for both fits. In fact, if the variational nature of both potential fits is preserved, the resulting four-center ERI free Hartree-Fock energy is nearly indistinguishable (≤ 1 kcal/mol) from its four-center ERI counterpart. The variation of the error functional ϵ_2^{F} with respect to the fitting coefficients $x_{\bar{k}ij}$ along with the maximization condition yields

$$\frac{\partial \epsilon_2^{\mathrm{F}}}{\partial x_{\bar{k}ij}} = -\langle \psi_i \psi_j \| \bar{k} \rangle + \sum_{\bar{l}} G_{\bar{k}\bar{l}} x_{\bar{l}ij} = 0 \tag{2.23}$$

Form Eq. (2.23), one can define a set of linear equation systems,

$$\mathbf{G}\mathbf{x}_{ij} = \mathbf{J}_{ij} \tag{2.24}$$

with

$$J_{\bar{k}ij} = \langle \psi_i \psi_j \| \bar{k} \rangle = \langle \rho_{ij} \| \bar{k} \rangle. \tag{2.25}$$

The solution for the fitting coefficients $x_{\bar{k}ij}$ is obtained as

$$x_{\bar{k}ij} = \sum_{\bar{l}} G_{\bar{k}\bar{l}}^{-1} \langle \bar{l} \| \psi_i \psi_j \rangle \tag{2.26}$$

After the fitting equations have been solved, the fitted Fock exchange can be written in a more compact form as

$$\tilde{E}_x^{\mathrm{F}} = -\sum_{i,j}^{\mathrm{occ}} \sum_{\bar{k},\bar{l}} \langle \psi_i \psi_j \| \bar{k} \rangle G_{\bar{k}\bar{l}}^{-1} \langle \bar{l} \| \psi_i \psi_j \rangle = -\frac{1}{4} \sum_{\mu,\nu} \sum_{\sigma\tau} P_{\mu\nu} P_{\sigma\tau} \langle \mu\sigma \| \bar{k} \rangle G_{\bar{k}\bar{l}}^{-1} \langle \bar{l} \| \tau\nu \rangle \tag{2.27}$$

The direct use of Eq. (2.27) avoids the explicit calculation of the three-index Fock exchange fitting coefficients appearing in Eq. (2.22). Note, however, that this is the result of solving the set of fitting equations given by Eq. (2.24). If this fitted Fock exchange energy is added to the Hartree energy with Coulomb fitting, the self-interaction-free density fitting Hartree-Fock energy expression is obtained [34]

$$\begin{aligned} \tilde{E}^{\mathrm{HF}} &= \sum_{\mu,\nu} P_{\mu\nu} H_{\mu\nu} + \sum_{\mu,\nu} \sum_{\bar{k}} P_{\mu\nu} \langle \mu\nu \| \bar{k} \rangle x_{\bar{k}} - \frac{1}{2} \sum_{\bar{k},\bar{l}} x_{\bar{k}} G_{\bar{k}\bar{l}} x_{\bar{l}} - \\ &\quad \frac{1}{4} \sum_{\mu,\nu} \sum_{\sigma\tau} P_{\mu\nu} P_{\sigma\tau} \langle \mu\sigma \| \bar{k} \rangle G_{\bar{k}\bar{l}}^{-1} \langle \bar{l} \| \tau\nu \rangle \end{aligned} \tag{2.28}$$

It is important to note that $\tilde{E}^{\mathrm{HF}}$ is self-interaction free only when the same auxiliary function set is used for both Coulomb and Fock exchange fittings [80]. Variation of Eq. (2.28) with respect to the density matrix yields the corresponding Fock matrix elements, $F_{\mu\nu}$, which now includes the variational fitting of the Coulomb and Fock potential

$$F_{\mu\nu} \equiv \left(\frac{\partial \tilde{E}^{\mathrm{HF}}}{\partial P_{\mu\nu}} \right)_{x_{\bar{k}}} = H_{\mu\nu} + \sum_{\bar{k}} \langle \mu\nu \| \bar{k} \rangle x_{\bar{k}} + X_{\mu\nu}^{\mathrm{F}} \tag{2.29}$$

Here the Fock potential contribution is defined as

$$\begin{aligned} X_{\mu\nu}^{\mathrm{F}} = \frac{\partial \tilde{E}_x^{\mathrm{F}}}{\partial P_{\mu\nu}} &= -\frac{1}{2} \sum_{\sigma\tau} \sum_{\bar{k},\bar{l}} P_{\sigma\tau} \langle \mu\sigma \| \bar{k} \rangle G_{\bar{k}\bar{l}}^{-1} \langle \bar{l} \| \tau\nu \rangle \\ &= -\sum_i^{\mathrm{occ}} \sum_{\bar{k},\bar{l}} \langle \mu\psi_i \| \bar{k} \rangle G_{\bar{k}\bar{l}}^{-1} \langle \bar{l} \| \psi_i\nu \rangle \end{aligned} \tag{2.30}$$

Straightforward implementation of Eq. (2.30) leads to an algorithm that scales as $\mathcal{O}(N_{aux} \times N_{bas}^2 \times N_{occ})$ with N_{aux} and N_{occ} being the number of auxiliary functions and occupied MOs, respectively. Such an algorithm is useful only when $\mathcal{O}(N_{bas}) \gg \mathcal{O}(N_{occ})$ [37, 38]. Note, however, that Eq. (2.30) is invariant under orthogonal transformation of the MOs, because the density matrix is invariant under such transformations. Thus, any set of molecular orbitals obtained by an unitary transformation of the canonical MOs can be used in (2.30). In this way, the canonical molecular orbitals (CMOs) can be transformed into spatially localized molecular orbitals (LMOs) by minimizing, or maximizing, an appropriated functional.

The recently developed variational fitting of the Fock potential [34] based on Foster-Boys localization shows an improved computational performance for the calculation of variational fitted Fock exchange energy. In this implementation a two step localization is used: First an incomplete Cholesky decomposition [81] is performed followed by a tighter Foster-Boys localization [82, 83]. The molecular orbital localization permits a variational fitting of Fock exchange by defining fitting domains around each localized molecular orbital. In particular, we define fitting domains around each localized MO in terms of atomic centers. To this end, we calculate the atomic Löwdin population for each atom A in a given localized MO i according to

$$n_{iA} = \sum_{\mu \in A} \sum_{\nu} S_{\mu\nu}^{1/2} c_{\nu i} \tag{2.31}$$

After ordering these atomic populations from the largest to the smallest, we sum them up until a threshold value (0.9995 for final energy calculation) is reached. All atoms that contribute to this sum define the atomic domain for the given localized MO i. The auxiliary functions on these atoms define the local auxiliary function set. The corresponding local basis function set is defined by all basis functions of the domain atoms and augmented by the basis functions from neighboring atoms with significant overlap ($\geq 10^{-6}$) into the domain. As a consequence of this localization each LMO has a particular Coulomb matrix. The computational cost for computing all these local $\mathbf{G}$ and $\mathbf{G}^{-1}$ matrices for all occupied LMOs is in larger systems more than overcompensated by the reduced dimensionality of these matrices.

2.3 Exchange-Correlation Potential from the Auxiliary Density

If the variational fitting of the Coulomb and Fock potential is used in the construction of the Kohn-Sham matrix for hybrid functionals, the most time-demanding computational step corresponds to the numerical integration of the exchange-correlation potential. This has motivated the use of auxiliary functions for the calculation of the exchange-correlation potential, too. A serious drawback of this approximation is that neither the fit nor the energy expression are variational and, therefore, only approximated gradients (and higher order derivatives) are available. As an alternative to this approach the direct use of the auxiliary function density from the variational fitting of the Coulomb potential for the calculation of the exchange-correlation potential has been investigated over the last two decades.

If the auxiliary function density is used for the evaluation of the exchange-correlation potential it is desirable that it is positive semi-definite and integrates to the number of electrons of the system. The normalization to the number of electrons can be included in the construction of the approximated density. Even without such a constraint the approximated density conserves the electron number to a high degree. In fact, in the latest deMon2k version this constraint is not used. On the other hand, the positive definiteness of the approximated density cannot be guaranteed by constraints. However, the construction of the approximated density avoids by itself the accumulation of larger areas with negative densities. As soon as a region accumulates negative fitted density it acts as an attractive potential for the remaining electron density. Because the fitting is variational in the Coulomb energy error, Eq. (2.1), negative fitted density regions almost never occur. In practice, during the numerical integration of the approximated density, grid points with negative density values can be screened without sacrificing the accuracy of the integrated electron number. This clearly indicates that the effect of artificial negative fitted density values is much smaller than the usually used grid accuracy for the numerical integration.

We now derive the basic working equations for the energy calculation using the auxiliary function density, $\tilde{\rho}(\mathbf{r})$, from the variational fitting of the Coulomb potential for the calculation of the exchange-correlation energy and potential. In this approach, which we name auxiliary density functional theory (ADFT), the energy, Eq. (2.7), is modified as follows:

$$E = \sum_{\mu,\nu} P_{\mu\nu} H_{\mu\nu} + \sum_{\mu,\nu} \sum_{\bar{k}} P_{\mu\nu} \langle \mu\nu \| \bar{k} \rangle x_{\bar{k}} - \frac{1}{2} \sum_{\bar{k},\bar{l}} x_{\bar{k}} G_{\bar{k}\bar{l}} x_{\bar{l}} + E_{xc}[\tilde{\rho}] \tag{2.32}$$

In the context of deMon2k calculations this energy expression is often named the AUXIS approach [76] because the auxiliary function density is used for the calculation of the exchange-correlation energy. The variation of this energy expression with respect to density matrix elements yields the corresponding Kohn-Sham matrix elements

$$K_{\mu\nu} = H_{\mu\nu} + \sum_{\bar{k}} \langle \mu\nu \| \bar{k} \rangle x_{\bar{k}} + \frac{\partial E_{xc}[\tilde{\rho}]}{\partial P_{\mu\nu}} \tag{2.33}$$

For the derivative of the exchange-correlation energy, assuming a local functional (the generalization to GGA functionals is straightforward [84]), follows

$$\frac{\partial E_{xc}[\tilde{\rho}]}{\partial P_{\mu\nu}} = \int \frac{\delta E_{xc}[\tilde{\rho}]}{\delta \tilde{\rho}(\mathbf{r})} \frac{\partial \tilde{\rho}(\mathbf{r})}{\partial P_{\mu\nu}} d\mathbf{r} = \sum_{\bar{k}} \frac{\partial x_{\bar{k}}}{\partial P_{\mu\nu}} \int v_{xc}[\tilde{\rho}(\mathbf{r})] \bar{k}(\mathbf{r}) d\mathbf{r} \tag{2.34}$$

Here we have introduced the exchange-correlation potential calculated from the auxiliary function density as:

$$v_{xc}[\tilde{\rho}(\mathbf{r})] = \frac{\delta E_{xc}[\tilde{\rho}]}{\delta \tilde{\rho}(\mathbf{r})} \tag{2.35}$$

The differentiation of the variational fitting coefficients with respect to the density matrix is given by

$$\frac{\partial x_{\bar{k}}}{\partial P_{\mu\nu}} = \sum_{\bar{l}} G_{\bar{k}\bar{l}} \langle \bar{l} \| \mu\nu \rangle \tag{2.36}$$

By inserting this result into Eq. (2.34) we find

$$\frac{\partial E_{xc}[\tilde{\rho}]}{\partial P_{\mu\nu}} = \sum_{\bar{k},\bar{l}} \langle \mu\nu \| \bar{k} \rangle G_{\bar{k}\bar{l}}^{-1} \langle \bar{l} | v_{xc}[\tilde{\rho}] \rangle \tag{2.37}$$

At this point, it is convenient to introduce the exchange-correlation fitting coefficients, $z_{\bar{l}}$, defined as

$$z_{\bar{l}} = \sum_{\bar{k}} G_{\bar{k}\bar{l}}^{-1} \langle \bar{k} | v_{xc}[\tilde{\rho}] \rangle \tag{2.38}$$

It is important to note that $\mathbf{z}$ is spin-dependent and accounts for the difference between the α and β Kohn-Sham matrices in open-shell calculations. We can reformulate Eq. (2.38) as an inhomogeneous equation system of the form

$$\mathbf{Gz} = \mathbf{L} \tag{2.39}$$

The vector $\mathbf{L}$ collects the numerical integrals $\langle \bar{k} | v_{xc}[\tilde{\rho}] \rangle$. Thus, in ADFT two inhomogeneous equation systems, (2.10) and (2.39), have to be solved. Because these two equation systems share the same coefficient matrix, namely $\mathbf{G}$, Domínguez-Soria et $al.$ [85] proposed a preconditioned conjugate gradient iterative solver for Eq (2.39) coupled to the Coulomb fitting solver. Recently, Pedroza-Montero et $al.$ [78] implemented an iterative solver based on a Krylov subspace method for solving these two linear system of equations in the de-Mon2k code. Once the Coulomb and exchange-correlation fitting coefficients are calculated the Kohn-Sham matrix elements can be expressed solely in terms of these coefficients

$$K_{\mu\nu} = H_{\mu\nu} + \sum_{\bar{k}} \langle \mu\nu \| \bar{k} \rangle \left(x_{\bar{k}} + z_{\bar{k}} \right) \tag{2.40}$$

Because the explicit derivative of the approximated density with respect to the density matrix elements can be calculated, the energy expression remains variational. For the implementation it is important to note that the fitting coefficients defined by Eq.(2.13) have to be used directly for the evaluation of the exchange-correlation potential in order to keep the calculation variational. Any manipulation of these coefficients, e.g. the mixing with previous coefficients, destroys the variational nature of the described approach. Of course, the coefficient mixing can still be used for the Coulomb term in the SCF energy expression.

Range-Separated Hybrid Functionals in Auxiliary Density Functional Theory

3.1 Range-Separation Schemes

Based on the early ideas of Savin [86], in 2001 Iikura *et al.* [87] proposed a long-range correction (LC) scheme where the Coulomb operator is separated into two terms by using the error function

$$\frac{1}{|\mathbf{r} - \mathbf{r}'|} = \frac{\text{erfc}(\omega|\mathbf{r} - \mathbf{r}'|)}{|\mathbf{r} - \mathbf{r}'|} + \frac{\text{erf}(\omega|\mathbf{r} - \mathbf{r}'|)}{|\mathbf{r} - \mathbf{r}'|} \tag{3.1}$$

In Eq. (3.1) the left-hand side is the Coulomb operator and the first term of the right-hand side is the short-range Coulomb operator. Consequently the last term on the right-hand side is the long-range Coulomb operator.
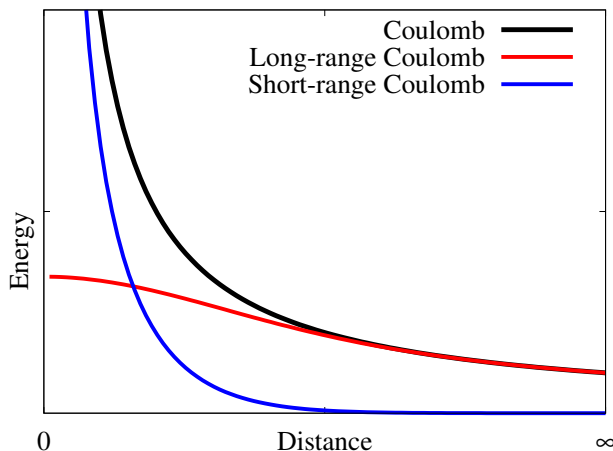
Figure 3.1: Schematic separation of the Coulomb operator into its short- and long-range contributions, respectively.

36

The parameter ω in Eq. (3.1) determines the ratio between short-range (SR) and long-range (LR) contribution. Fig. 3.1 shows the splitting of the Coulomb operator (red line) into a SR (green line) and LR (blue line) contribution defined in Eq. (3.1) with $\omega = 0.3$. For $\omega = \infty$ it follows SR $= 0$ and the LR contribution becomes the Coulomb operator. On the other hand, for $\omega = 0$ the SR contribution becomes the Coulomb operator and LR $= 0$ follows.

In long-range correction scheme the SR contribution is generally expressed by an appropriate modified GGA functional of the form [87]

$$E_x^{\text{SR-GGA}} = -\frac{3}{4} \left(\frac{3}{\pi}\right)^{1/3} \int \rho(\mathbf{r})^{4/3} F_x(s) \left(1 - \frac{8}{3}a \left[\sqrt{\pi}\operatorname{erf}\left(\frac{1}{2a}\right) + 2a(b-c)\right]\right) d\mathbf{r} \qquad (3.2)$$

where

$$a = \frac{\omega\sqrt{F_x}}{2\pi^{2/3}(6\rho)^{1/3}} \qquad (3.3)$$

$$b = \exp\left(-\frac{1}{4a^2}\right) - 1, \qquad (3.4)$$

$$c = 2a^2b + \frac{1}{2} \qquad (3.5)$$

In Eqs. (3.2) and (3.3) F_x is the enhancement factor of the GGA exchange. In the here discussed functionals either the B88 or the PBE exchange is used. The LR contribution is usually expressed by the corresponding Fock energy as

$$E_x^{\text{LR-F}} = -\sum_{i,j}^{\text{occ}} \iint \psi_i(\mathbf{r})\psi_j(\mathbf{r})\frac{\operatorname{erf}(\omega|\mathbf{r} - \mathbf{r}'|)}{|\mathbf{r} - \mathbf{r}'|}\psi_i(\mathbf{r}')\psi_j(\mathbf{r}')\, d\mathbf{r}\, d\mathbf{r}', \qquad (3.6)$$

Using the LCGTO approximation the LR Fock energy can be written as

$$E_x^{\text{LR-F}} = -\frac{1}{4}\sum_{\mu,\nu}\sum_{\sigma,\tau} P_{\mu\nu}P_{\sigma\tau}\langle\mu\sigma\underline{\|}\nu\tau\rangle \qquad (3.7)$$

In this notation we used the underlined double vertical bar to represents the LR Coulomb operator

$$\underline{\|} \equiv \frac{\operatorname{erf}(\omega|\mathbf{r} - \mathbf{r}'|)}{|\mathbf{r} - \mathbf{r}'|} \qquad (3.8)$$

Similar to the Coulomb operator, Eq. (1.53), this operator also separates the functions of electron 1, on the left, from those of electron 2, on the right.

Therefore, long-range corrected exchange-correlation functionals have the general form

$$E_{xc}^{\text{LC}} = E_x^{\text{SR-GGA}} + E_x^{\text{LR-F}} + E_c^{\text{GGA}} \qquad (3.9)$$

The two bound limits for the range-separation parameter ω are the used GGA exchange for $\omega = 0$ and the standard Fock exchange for $\omega = \infty$.

Later on, in 2004, Yanai *et al.* [88] extended the LC approach by the following separation of the Coulomb operator

$$\frac{1}{|\mathbf{r} - \mathbf{r}'|} = \frac{1 - [\alpha + \beta\,\mathrm{erf}(\omega|\mathbf{r} - \mathbf{r}'|)]}{|\mathbf{r} - \mathbf{r}'|} + \frac{\alpha + \beta\,\mathrm{erf}(\omega|\mathbf{r} - \mathbf{r}'|)}{|\mathbf{r} - \mathbf{r}'|} \tag{3.10}$$

Again the first term on the right-hand side of Eq. (3.10) represents the SR and the second term the LR part of the Coulomb operator. This approach is called *Coulomb attenuating method* (CAM). In the CAM α and β satisfy the conditions $0 \leq \alpha + \beta \leq 1$, $0 \leq \alpha \leq 1$ and $0 \leq \beta \leq 1$. In Eq. (3.10) the parameter α allows the incorporation of global Fock exchange while decreasing the contribution of global GGA exchange. As a result, the SR GGA contribution also depends from α and β in the CAM. The SR CAM GGA energy expression is given by [88]

$$E_x^{\text{SR-GGA}} = -\frac{3}{4}\left(\frac{3}{\pi}\right)^{1/3}\int \rho(\mathbf{r})^{4/3}F_x(s)\left(1 - \alpha - \frac{8}{3}a\beta\left[\sqrt{\pi}\,\mathrm{erf}\left(\frac{1}{2a}\right) + 2a(b - c)\right]\right)d\mathbf{r} \tag{3.11}$$
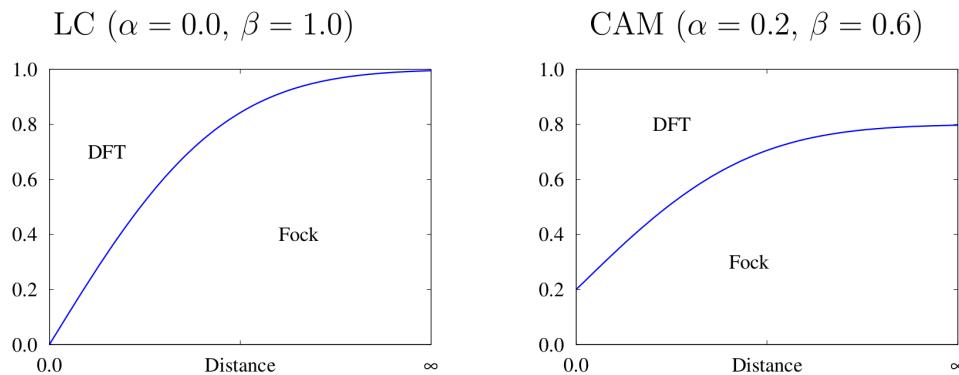
Figure 3.2: Schematic plots of the contribution of DFT and Fock exchange to the total exchange regarding the distance increase for LC (left) and CAM (right) functionals.

The original LC scheme corresponds to the CAM with $\alpha = 0.0$ and $\beta = 1.0$. The schematic diagrams in Figure 3.2 illustrate the partitioning of the DFT and Fock exchange components for the LC ($\alpha = 0.0$, $\beta = 1.0$, $\omega = 0.33$), on the left, and the CAM ($\alpha = 0.2$, $\beta = 0.6$, $\omega = 0.33$) on the right side. In the LC functionals Fock and DFT exchanges vanish at $\mathbf{r} = 0$

and $\mathbf{r} = \infty$, respectively. On the other hand, in the CAM functionals there exist always a mixing of Fock and DFT exchange. The Fock exchange contribution at $\mathbf{r} = 0$ is given by the α parameter and increases until a limit given by the amount $\alpha + \beta$ for $\mathbf{r} = \infty$. The behavior of the DFT exchange is opposite to that described for the Fock exchange. As we will see later, this exchange mixing in the CAM improves the results that can be obtained with LC. In this thesis we will discuss a family of B88 range-separated hybrid functionals with the general form given by [18, 88–91]

$$E_{xc}^{\text{RS-B88}} = \alpha E_x^{\text{F}} + \beta E_x^{\text{LR-F}} + E_x^{\text{SR-B88}} + \gamma \Delta E_x^{\text{B88}} + \delta E_c^{\text{LYP}} + (1 - \delta)E_c^{\text{VWN5}} \qquad (3.12)$$

The values for the different parameters are given in Table 3.1 for the here used functionals of this type.

Table 3.1: Parameter values for the here discussed family of B88 range-separated hybrid functionals.

Functional	Exchange			Correlation	
	α	β	δ	γ	ω
LCBLYP	0.00000	1.00000	1.00	0.0000	0.33
CAMB3LYP	0.19000	0.46000	0.81	0.0000	0.33
CAMQTP00	0.54000	0.37000	0.80	0.0000	0.29
CAMQTP01	0.23000	0.77000	0.80	0.0000	0.31
rCAMB3LYP	0.18352	0.94979	0.81	0.1359	0.33

The value of $\omega = 0.33$ was originally determined for the LCBLYP [18] functional so as to minimize the mean absolute deviation of the calculated equilibrium distance for dimers of first and second-row atoms (except rare-gas dimers) with the 6-311G++(2d,2p) basis set. For CAMB3LYP [88] the α and β parameters were determined through a fit to the atomization energy of the G2 set of molecules. Notice that if $\beta = 0$ in Eq. (3.11), the first three exchange energy terms in Eq. (3.12) reduce to $\alpha E_x^F + (1 - \alpha)E_x^{B88}$, demonstrating that CAMB3LYP has a closed connection to the B3LYP functional ($\alpha = 0.20$). The parameters α, β and ω for the CAMQTP00 [89] functional were optimized to reproduce best the experimental vertical ionization potentials for the following molecules: H_2O, CO, HF, N_2, F_2, H_2CO, CH_4, pyridine, CHF=CF_2, thiophene, CH_2=CF_2, O_3, H_2C-CCl_2, CH_3CN, CH_3F, C_2H_4, $HCONH_2$, HCOOH, NH_3, CH_3COCH_3, CH_3CCH, CH_3NC, CH_2F_2, C_2H_6, P_2, HCN, C_2H_2, HCCN, NCCCN, C_2N_2, CO_2, C_3O_2, OCS, FCN, s-tetrazine, furan, acrolein, CS, SiO, HCl, CHF_3,

and N_2O using a cc-pVTZ basis set. The range-separation parameters in CAMQTP01 [90] functional were optimized to improve the accuracy over CAMQTP00, especially in the vertical excitation energies for Rydberg states of the above mentioned molecular systems. QTP stands for the Quantum Theory Project at University of Florida by R. Bartlett. Finally, the rCAMB3LYP [91] (r stands for revised) α, β and ω parameters were optimized by considering the performance of the functional for systems with fractional numbers of electrons as well as standard thermochemical tests. This parametrization aims to minimize the many-electron self-interaction error. It additionally includes a fraction of global semi-local B88 exchange, ΔE_x^{B88}.

Also we will discuss a family of PBE range-separated hybrids with the general form [92, 93]

$$E_{xc}^{\text{RS-PBE}} = \alpha E_x^{\text{F}} + \beta E_x^{\text{LR-F}} + E_x^{\text{SR-PBE}} + E_c^{\text{PBE}} \tag{3.13}$$

Table 3.2: Parameter values for the here discussed family of PBE range-separated hybrid functionals

Functional	α	β	ω
LCPBE	0.00	1.00	0.30
CAMPBE0	0.25	0.75	0.30

Here the parameter $\omega = 0.30$ for LCPBE [92] and CAMPBE0 [93] functionals was calibrated to provide reasonable accuracy for both ground-state properties (atomization energies, barrier heights, electron affinities and ionization energies) as well as for time-dependent DFT vertical excitation energies (localized and charge-transfer). The parameters α and β in CAMPBE0 were taken to recover the PBE0 $(0.25E_x^{\text{F}} + 0.75E_x^{\text{PBE}} + E_c^{\text{PBE}})$ functional for $\omega = 0$.

In 2003 Heyd and coworkers [94] proposed a new family of range-separated hybrid functional which utilize Fock exchange for short-range interactions. This allows the exchange hole to become delocalized among the near neighbors of a reference point, but not beyond. Since in real system, polarization effects screen the interactions between distant electrons, the corresponding contribution to the long-range exchange disappears. Thus, this part of exchange is modeled by the long-range GGA exchange.

The SR Fock exchange energy is defined as

$$E_x^{\text{SR-F}} = -\sum_{i,j}^{occ} \iint \psi_i(\mathbf{r})\psi_j(\mathbf{r})\frac{\text{erfc}(\omega|\mathbf{r} - \mathbf{r}'|)}{|\mathbf{r} - \mathbf{r}'|}\psi_i(\mathbf{r}')\psi_j(\mathbf{r}')\,d\mathbf{r}\,d\mathbf{r}' \tag{3.14}$$

Employing the LCGTO approximation the SR Fock energy can be expressed as

$$E_x^{\text{SR-F}} = -\frac{1}{4} \sum_{\mu,\nu} \sum_{\sigma,\tau} P_{\mu\nu} P_{\sigma\tau} \langle \mu\sigma \overline{\|} \nu\tau \rangle \tag{3.15}$$

The overlined double vertical bar represents the SR Coulomb operator

$$\overline{\|} \equiv \frac{\text{erfc}(\omega|\mathbf{r} - \mathbf{r}'|)}{|\mathbf{r} - \mathbf{r}'|} \tag{3.16}$$

Alike to the Coulomb and LR Coulomb operators, the SR Coulomb operator separates the functions of electron 1, on the left, from those of electron 2, on the right. The short-range component of Fock exchange can be obtained by using the global and long-range Coulomb potential

$$E_x^{\text{SR-F}} = E_x - E_x^{\text{LR-F}} \tag{3.17}$$

This represent a straightforward implementation for SR electron repulsion integrals (ERIs) by small modifications of the recurrence relations for the three-center ERI calculation [40]. Evaluating the short range ERIs is only slightly more time consuming than the regular ERIs since only the primitive integrals are modified.

The corresponding LR-GGA contribution can be calculated by the definition of GGA and short-range GGA exchange functionals, Eq. (3.2), as follows

$$E_x^{\text{LR-GGA}} = E_x^{\text{GGA}} - E_x^{\text{SR-GGA}} \tag{3.18}$$

Eq. (3.18) is an easy way to program the LR-GGA contribution for the screened hybrid functional. This particular range separation is nowadays referred to as Heyd-Scuseria-Ernzerhof (HSE) functional which has the general form

$$E_{xc}^{\text{HSE}} = 0.25 E_x^{\text{SR-F}} + 0.75 E_x^{\text{LR-PBE}} + E_c^{PBE} \tag{3.19}$$

The ω parameter was optimized with respect to a benchmark data set of molecules [94, 95], which yielded $\omega = 0.15$ (Erroneously in the original implementation two ω parameters were introduced $\omega = 0.15/\sqrt{2}$ for Fock exchange and $\omega = 0.15 \times 2^{1/3}$ for the PBE part). Krukau *et al.* [96] later redefined this value for solids to a value of $\omega = 0.11$. To differentiate between the different screening parameters, the corresponding functionals are labeled HSE03 [95] and HSE06 [96] for $\omega = 0.15$ and $\omega = 0.11$, respectively. The amount of SR-Fock and

LR-PBE exchange in (3.19) was chosen to recover the PBE0 hybrid functional for $\omega = 0$ and asymptotically reaches PBE for $\omega = \infty$. The calculation of the LR-PBE exchange in Eq. (3.18) involves the computation of the SR-PBE exchange. This implicates the use of the range-separation parameters α and β. For this particular case the values for α and β are 0.0 and 1.0, respectively. This approach permits the use of a common subroutine for evaluating Eq. (3.2) for SR and LR GGA contributions.

3.2   Variational Fitting of Fock Potential with Range-Separation

A variational local density fitting approach for the Fock exchange energy and potential was presented in section 2.2. Fock exchange is necessary for the computation of global and range-separated hybrid functionals. In combination with ADFT a computational efficient approach for global hybrid functional calculations was achieved [43]. By construction, the long-range correction scheme and the Coulomb attenuating methodology need to compute the long-range Fock exchange energy and potential. In this section we develop the local density fitting for the LR Fock exchange by using the orbital product, ρ_{ij}, and auxiliary orbital product, $\tilde{\rho}_{ij}$, given by Eqs. (2.15) and (2.18), respectively. Similar as for the Fock exchange energy, the variational fitting of the LR Fock exchange energy is based on the maximization of the following negative semi-definite (see Appendix A) error functional

$$\epsilon_2^{\text{LR-F}} = -\sum_{i,j}^{\text{occ}} \langle \rho_{ij} - \tilde{\rho}_{ij} \| \rho_{ij} - \tilde{\rho}_{ij} \rangle \leq 0 \tag{3.20}$$

Here, for convenience of notation, we used the short-hand notation for the long-range Coulomb operator $\|$, Eq. (3.8). Due to the negative definiteness of the error functional, Eq. (3.20), it follows

$$-\sum_{i,j}^{\text{occ}} \langle \rho_{ij} \| \rho_{ij} \rangle \leq -2 \sum_{i,j}^{\text{occ}} \langle \rho_{ij} \| \tilde{\rho}_{ij} \rangle + \sum_{i,j}^{\text{occ}} \langle \tilde{\rho}_{ij} \| \tilde{\rho}_{ij} \rangle \tag{3.21}$$

Employing the LCGTO approximation yields

$$E_x^{\text{LR-F}} = -\sum_{i,j}^{\text{occ}} \langle \psi_i \psi_j \| \psi_i \psi_j \rangle \leq -2 \sum_{i,j}^{\text{occ}} \sum_{\bar{k}} \langle \psi_i \psi_j \| \bar{k} \rangle x_{\bar{k}ij} + \sum_{i,j}^{\text{occ}} \sum_{\bar{k},\bar{l}} x_{\bar{k}ij} G_{\bar{k}\bar{l}}^{\text{LR}} x_{\bar{l}ij} = \tilde{E}_x^{\text{LR-F}} \tag{3.22}$$

where we introduce the long-range Coulomb matrix defined as

$$G_{\bar{k}\bar{l}}^{\text{LR}} = \langle \bar{k} \| \bar{l} \rangle \tag{3.23}$$

The maximization of the error functional $\epsilon_2^{\text{LR-F}}$ with respect to the fitting coefficients, $x_{\bar{k}ij}$,

$$\frac{\partial \epsilon_2^{\text{LR-F}}}{\partial x_{\bar{k}ij}} = -2\langle \psi_i \psi_j \| \bar{k}\rangle + 2\sum_{\bar{l}} x_{\bar{l}ij} G_{\bar{k}\bar{l}}^{\text{LR}} = 0, \tag{3.24}$$

yields an inhomogeneous equation system for each occupied MO combination ij similar to the Fock exchange, Eq. (2.24). Solving the corresponding equation system yields for the long-range fitting coefficients

$$x_{\bar{k}ij}^{\text{LR}} = \sum_{\bar{l}} G_{\bar{k}\bar{l}}^{\text{LR}^{-1}} \langle \bar{l} \| \psi_i \psi_j\rangle \tag{3.25}$$

According to the maximization of ϵ_2^{LR}, the variationally approximated LR Fock exchange energy is given by

$$\tilde{E}_x^{\text{LR-F}} = -\sum_{i,j}^{\text{occ}} \sum_{\bar{k},\bar{l}} \langle \psi_i \psi_j \| \bar{k}\rangle G_{\bar{k}\bar{l}}^{\text{LR}^{-1}} \langle \bar{l} \| \psi_i \psi_j\rangle = -\frac{1}{4} \sum_{\mu,\nu} \sum_{\sigma,\tau} P_{\mu\nu} P_{\sigma\tau} \langle \mu\sigma \| \bar{k}\rangle G_{\bar{k}\bar{l}}^{\text{LR}^{-1}} \langle \bar{l} \| \tau\nu\rangle \tag{3.26}$$

Eq. (3.26) is LR four-center ERI free and depends only from LR three-center ERIs and the inverse of the LR Coulomb matrix. Note that the MOs in the long-range ERIs in Eq. (3.26) are localized and the corresponding atomic orbitals and auxiliary functions are selected according to the same criteria as for the Fock exchange fitting described in the section 2.2. The validity of the fitting domains around each localized MO will be discussed later on in section 4.2.2 of this thesis. Because of the different domains the long-range Coulomb matrix will be different for each occupied MO, ψ_i, in Eq (3.26).

The long-range Fock potential contribution that enters the Kohn-Sham matrix with LC and CAM functionals can be directly calculated by differentiation of $\tilde{E}_x^{\text{LR-F}}$, Eq. (3.26), with respect to density matrix elements

$$X_{\mu\nu}^{\text{LR-F}} \equiv \frac{\partial \tilde{E}_x^{\text{LR-F}}}{\partial P_{\mu\nu}} = -\sum_i^{\text{occ}} \sum_{\bar{k},\bar{l}} \langle \mu\psi_i \| \bar{k}\rangle G_{\bar{k}\bar{l}}^{\text{LR}^{-1}} \langle \bar{l} \| \psi_i \nu\rangle \tag{3.27}$$

Having developed the variational fitted long-range Fock exchange energy and its corresponding potential in combination with the previously discussed variational fitted Fock exchange potential, a variational fitted short-range Fock potential, that enters to the Kohn-Sham matrix in HSE functionals, can be defined as follows

$$X_{\mu\nu}^{\text{SR-F}} = X_{\mu\nu}^{\text{F}} - X_{\mu\nu}^{\text{LR-F}} \tag{3.28}$$

By the combination of fitted global and long-range Fock exchange energies with exchange-correlation energy functionals calculated with auxiliary densities, range-separated hybrid ADFT energy expressions without four-center ERIs are obtained. In particular, we find the following generic ADFT energy expressions for the here discussed functionals

$$
\begin{aligned}
E^{\text{RS-B88}} \;=\; & \sum_{\mu,\nu} P_{\mu\nu} H_{\mu\nu} + \sum_{\mu,\nu}\sum_{\bar{k}} P_{\mu\nu}\langle\mu\nu\|\bar{k}\rangle x_{\bar{k}} - \frac{1}{2}\sum_{\bar{k},\bar{l}} x_{\bar{k}} G_{\bar{k}\bar{l}} x_{\bar{l}} - \\
& \alpha \sum_{i,j}^{\text{occ}}\sum_{\bar{k},\bar{l}} \langle\psi_i\psi_j\|\bar{k}\rangle G_{\bar{k}\bar{l}}^{-1}\langle\bar{l}\|\psi_i\psi_j\rangle - \beta \sum_{i,j}^{\text{occ}}\sum_{\bar{k},\bar{l}} \langle\psi_i\psi_j\underline{\|}\bar{k}\rangle G_{\bar{k}\bar{l}}^{\text{LR}^{-1}}\langle\bar{l}\underline{\|}\psi_i\psi_j\rangle + \\
& E_x^{\text{SR-B88}}(\omega)[\tilde{\rho}] + \gamma\Delta E_x^{\text{B88}}[\tilde{\rho}] + \delta E_c^{\text{LYP}}[\tilde{\rho}] + (1-\delta)E_c^{\text{VWN5}}[\tilde{\rho}] \qquad (3.29)
\end{aligned}
$$

$$
\begin{aligned}
E^{\text{RS-PBE}} \;=\; & \sum_{\mu,\nu} P_{\mu\nu} H_{\mu\nu} + \sum_{\mu,\nu}\sum_{\bar{k}} P_{\mu\nu}\langle\mu\nu\|\bar{k}\rangle x_{\bar{k}} - \frac{1}{2}\sum_{\bar{k},\bar{l}} x_{\bar{k}} G_{\bar{k}\bar{l}} x_{\bar{l}} - \\
& \alpha \sum_{i,j}^{\text{occ}}\sum_{\bar{k},\bar{l}} \langle\psi_i\psi_j\|\bar{k}\rangle G_{\bar{k}\bar{l}}^{-1}\langle\bar{l}\|\psi_i\psi_j\rangle - \beta \sum_{i,j}^{\text{occ}}\sum_{\bar{k},\bar{l}} \langle\psi_i\psi_j\underline{\|}\bar{k}\rangle G_{\bar{k}\bar{l}}^{\text{LR}^{-1}}\langle\bar{l}\underline{\|}\psi_i\psi_j\rangle + \\
& E_x^{\text{SR-PBE}}[\tilde{\rho}] + E_c^{\text{PBE}}[\tilde{\rho}] \qquad (3.30)
\end{aligned}
$$

$$
\begin{aligned}
E^{\text{HSE}} \;=\; & \sum_{\mu,\nu} P_{\mu\nu} H_{\mu\nu} + \sum_{\mu,\nu}\sum_{\bar{k}} P_{\mu\nu}\langle\mu\nu\|\bar{k}\rangle x_{\bar{k}} - \frac{1}{2}\sum_{\bar{k},\bar{l}} x_{\bar{k}} G_{\bar{k}\bar{l}} x_{\bar{l}} + \\
& 0.25\left(-\sum_{i,j}^{\text{occ}}\sum_{\bar{k},\bar{l}} \langle\psi_i\psi_j\|\bar{k}\rangle G_{\bar{k}\bar{l}}^{-1}\langle\bar{l}\|\psi_i\psi_j\rangle + \sum_{i,j}^{\text{occ}}\sum_{\bar{k},\bar{l}} \langle\psi_i\psi_j\underline{\|}\bar{k}\rangle G_{\bar{k}\bar{l}}^{\text{LR}^{-1}}\langle\bar{l}\underline{\|}\psi_i\psi_j\rangle\right) + \\
& 0.75\left(E_x^{\text{PBE}}[\tilde{\rho}] - E_x^{\text{SR-PBE}}[\tilde{\rho}]\right) + E_c^{\text{PBE}}[\tilde{\rho}] \qquad (3.31)
\end{aligned}
$$

Here α and β denotes the fraction of Fock and long-range Fock exchange, respectively, to be used in the range-separated hybrid functionals.

A generalization of these ADFT energy expressions (Eqs. 3.29, 3.30 and 3.31) can be formulated as follows

$$
\begin{aligned}
E \;=\; & \sum_{\mu,\nu} P_{\mu\nu} H_{\mu\nu} + \sum_{\mu,\nu}\sum_{\bar{k}} P_{\mu\nu}\langle\mu\nu\|\bar{k}\rangle x_{\bar{k}} - \frac{1}{2}\sum_{\bar{k},\bar{l}} x_{\bar{k}} G_{\bar{k}\bar{l}} x_{\bar{l}} + E_{xc}[\tilde{\rho}] + \\
& c_{\text{F}}\left(-\alpha\sum_{i,j}^{\text{occ}}\sum_{\bar{k},\bar{l}} \langle\psi_i\psi_j\|\bar{k}\rangle G_{\bar{k}\bar{l}}^{-1}\langle\bar{l}\|\psi_i\psi_j\rangle - \beta\sum_{i,j}^{\text{occ}}\sum_{\bar{k},\bar{l}} \langle\psi_i\psi_j\underline{\|}\bar{k}\rangle G_{\bar{k}\bar{l}}^{\text{LR}^{-1}}\langle\bar{l}\underline{\|}\psi_i\psi_j\rangle\right) \qquad (3.32)
\end{aligned}
$$

In Eq. (3.32) we have introduced the c_F factor, which scales the total amount of Fock exchange, e.g. for the RS-B88 and RS-PBE functionals c_F=1.0 and for HSE functionals c_F=0.25. The short-range Fock exchange energy in Eq. (3.32) can be obtained by setting $\alpha = 1.0$ and $\beta = -1.0$. Note however, that for the calculation of the SR-PBE exchange contribution in HSE functionals $\alpha = 0.0$ and $\beta = 1.0$ must be used. These non Fock exchange contributions, i.e. the corresponding DFT exchange and correlation functional contribution are collected in $E_{xc}[\tilde{\rho}]$ and are specific to each family of range-separated hybrid functionals. The variation of the generic energy expressions, Eq. (3.32), with respect to the MO coefficients, under the MO orthonormality constraints, leads to Roothaan-Hall equation systems. The generic ADFT Kohn-Sham matrix elements for range-separated hybrid functionals is then given by

$$
\begin{aligned}
K_{\mu\nu} = {} & H_{\mu\nu} + \sum_{\bar{k}} \langle \mu\nu \| \bar{k} \rangle (x_{\bar{k}} + z_{\bar{k}}) + c_F \left(-\alpha \sum_{i}^{\text{occ}} \sum_{\bar{k},\bar{l}} \langle \mu\psi_i \| \bar{k} \rangle \langle \bar{k} \| \bar{l} \rangle^{-1} \langle \bar{l} \| \psi_i \nu \rangle - \right. \\
& \left. \beta \sum_{i}^{\text{occ}} \sum_{\bar{k},\bar{l}} \langle \mu\psi_i \| \underline{\bar{k}} \rangle \langle \underline{\bar{k}} \| \underline{\bar{l}} \rangle^{-1} \langle \underline{\bar{l}} \| \psi_i \nu \rangle \right)
\end{aligned}
\tag{3.33}
$$

Note that the exchange-correlation fitting coefficients appearing in Eq. (3.33) absorb the contribution from all exchange-correlation functionals wired into the corresponding functional. The implementation of Eqs. (3.32) and (3.33) into deMon2k allows for self-consistent energy calculations with range-separated hybrid functionals.

3.3 Energy Gradients of Range-Separated Functionals

Analytic energy derivatives with respect to nuclear positions play a fundamental role for structure optimizations and vibrational frequency analyses. To formulate ADFT energy derivatives for range-separated hybrid functionals we use the generic energy expression of Eq. (3.32) written in the form

$$
E = \sum_{\mu,\nu} P_{\mu\nu} H_{\mu\nu} + \sum_{\mu,\nu} \sum_{\bar{k}} P_{\mu\nu} \langle \mu\nu \| \bar{k} \rangle x_{\bar{k}} - \frac{1}{2} \sum_{\bar{k},\bar{l}} x_{\bar{k}} G_{\bar{k}\bar{l}} x_{\bar{l}} + E_{xc}[\tilde{\rho}] + c_F \left(\alpha E_x^{\text{F}} + \beta E_x^{\text{LR-F}} \right) \tag{3.34}
$$

Thus, the ADFT energy derivative with respect to a nuclear coordinate, indicated by the (λ) superscript, is given by [80, 97, 98]

$$
\begin{aligned}
E^{(\lambda)} &= \sum_{\mu,\nu} P_{\mu\nu}^{(\lambda)} H_{\mu\nu} + \sum_{\mu,\nu} P_{\mu\nu} H_{\mu\nu}^{(\lambda)} + \sum_{\mu,\nu} \sum_{\bar{k}} P_{\mu\nu} \langle \mu\nu \| \bar{k} \rangle^{(\lambda)} x_{\bar{k}} + \sum_{\mu,\nu} \sum_{\bar{k}} P_{\mu\nu}^{(\lambda)} \langle \mu\nu \| \bar{k} \rangle x_{\bar{k}} - \\
&\quad \frac{1}{2} \sum_{\bar{k},\bar{l}} x_{\bar{k}} G_{\bar{k}\bar{l}}^{(\lambda)} x_{\bar{l}} + E_{xc}^{(\lambda)} + c_{\mathrm{F}} \left(\alpha E_x^{\mathrm{F}(\lambda)} + \beta E_x^{\mathrm{LR\text{-}F}(\lambda)} \right)
\end{aligned}
\tag{3.35}
$$

The derivatives of the elements of $\mathbf{H}$, $\mathbf{G}$ and the three-center ERIs are obtained through integral recurrence relations. The derivative of E_{xc} is obtained via the chain rule and is given by [4]

$$
\begin{aligned}
E_{xc}[\tilde{\rho}]^{(\lambda)} &= \sum_{\mu,\nu} \sum_{\bar{k}} P_{\mu\nu}^{(\lambda)} \langle \mu\nu \| \bar{k} \rangle z_{\bar{k}} + \sum_{\mu,\nu} \sum_{\bar{k}} P_{\mu\nu} \langle \mu\nu \| \bar{k} \rangle^{(\lambda)} z_{\bar{k}} - \\
&\quad \sum_{\bar{k},\bar{l}} x_{\bar{k}} G_{\bar{k}\bar{l}}^{(\lambda)} z_{\bar{l}} + \sum_{\bar{k}} x_{\bar{k}} \langle v_{xc}[\tilde{\rho}] | \bar{k}^{(\lambda)} \rangle
\end{aligned}
\tag{3.36}
$$

The derivative of $E_x^{\mathrm{F}(\lambda)}$ can be expressed as [80]

$$
E_x^{\mathrm{F}(\lambda)} = \sum_{\mu,\nu} P_{\mu\nu}^{(\lambda)} X_{\mu\nu}^{\mathrm{F}} + \sum_{\bar{k},\bar{l}} \Gamma_{\bar{k}\bar{l}} G_{\bar{k}\bar{l}}^{(\lambda)} - \sum_i^{\mathrm{occ}} \sum_{\bar{k}} \sum_{\sigma} \sum_{\mu,\nu} P_{\mu\nu} x_{\bar{k}\mu i} \langle \bar{k} \| \nu\sigma \rangle^{(\lambda)} c_{\sigma i}
\tag{3.37}
$$

where

$$
\Gamma_{\bar{k}\bar{l}} = \frac{1}{2} \sum_i^{\mathrm{occ}} \sum_{\mu\nu} x_{\bar{k}\mu i} P_{\mu\nu} x_{\bar{l}\nu i}
\tag{3.38}
$$

and

$$
x_{\bar{k}\mu i} = \sum_{\bar{l}} G_{\bar{k}\bar{l}}^{-1} \langle \bar{k} \| \mu\psi_i \rangle
\tag{3.39}
$$

It should be noted that all these terms are readily available in deMon2k and we will not further discuss them. For a competent discussion of the calculation and implementation of these terms we refer the interested reader to references [80], [97] and [98].

Now we will develop the analytic energy gradients for the variational fitted long-range Fock potential. In order to ease notation we rewrite the LR Fock exchange energy, Eq. (3.26), in terms of fitting domains of LMOs as follow

$$
E_x^{\mathrm{LR\text{-}F}} = -\frac{1}{2} \sum_{\mu,\nu} P_{\mu\nu} \sum_i^{\mathrm{occ}} \sum_{\bar{k}} x_{\bar{k}\mu i}^{\mathrm{LR}} J_{\bar{k}\nu i}^{\mathrm{LR}}
\tag{3.40}
$$

where

$$
J_{\bar{k}\nu i}^{\mathrm{LR}} = \langle \bar{k} \underline{\|} \nu\psi_i \rangle
\tag{3.41}
$$

and

$$x_{\bar{k}\mu i}^{\mathrm{LR}} = \sum_{\bar{l}} G_{\bar{k}\bar{l}}^{\mathrm{LR}\,-1} J_{\bar{l}\mu i}^{\mathrm{LR}} \tag{3.42}$$

The derivative of Eq (3.40) is

$$
\begin{aligned}
E_x^{\mathrm{LR\text{-}F}(\lambda)} &= -\frac{1}{2}\sum_{\mu,\nu} P_{\mu\nu}^{(\lambda)} \sum_i^{\mathrm{occ}} \sum_{\bar{k}} x_{\bar{k}\mu i}^{\mathrm{LR}} J_{\bar{k}\nu i}^{\mathrm{LR}} - \frac{1}{2}\sum_{\mu,\nu} P_{\mu\nu} \sum_i^{\mathrm{occ}} \sum_{\bar{k}} x_{\bar{k}\mu i}^{\mathrm{LR}\,(\lambda)} J_{\bar{k}\nu i}^{\mathrm{LR}} - \\
&\quad \frac{1}{2}\sum_{\mu,\nu} P_{\mu\nu} \sum_i^{\mathrm{occ}} \sum_{\bar{k}} x_{\bar{k}\mu i}^{\mathrm{LR}} J_{\bar{k}\nu i}^{\mathrm{LR}(\lambda)}
\end{aligned} \tag{3.43}
$$

The $x_{\bar{k}\mu i}^{\mathrm{LR}\,(\lambda)}$ are obtained by differentiation of Eq. (3.42). This yields

$$
\begin{aligned}
E_x^{\mathrm{LR\text{-}F}(\lambda)} &= -\frac{1}{2}\sum_{\mu,\nu} P_{\mu\nu}^{(\lambda)} \sum_i^{\mathrm{occ}} \sum_{\bar{k}} x_{\bar{k}\mu i}^{\mathrm{LR}} J_{\bar{k}\nu i}^{\mathrm{LR}} + \frac{1}{2}\sum_{\mu,\nu} P_{\mu\nu} \sum_i^{\mathrm{occ}} \sum_{\bar{k},\bar{l}} x_{\bar{k}\mu i}^{\mathrm{LR}} G_{\bar{k}\bar{l}}^{\mathrm{LR}(\lambda)} x_{\bar{l}\nu i}^{\mathrm{LR}} - \\
&\quad \frac{1}{2}\sum_{\mu,\nu} P_{\mu\nu} \sum_i^{\mathrm{occ}} \sum_{\bar{k}} J_{\bar{k}\mu i}^{\mathrm{LR}(\lambda)} x_{\bar{k}\nu i}^{\mathrm{LR}} - \frac{1}{2}\sum_{\mu,\nu} P_{\mu\nu} \sum_i^{\mathrm{occ}} \sum_{\bar{k}} x_{\bar{k}\mu i}^{\mathrm{LR}} J_{\bar{k}\nu i}^{\mathrm{LR}(\lambda)}
\end{aligned} \tag{3.44}
$$

With the substitution,

$$J_{\bar{k}\mu i}^{\mathrm{LR}(\lambda)} = \sum_{\mu} \langle \bar{k}\|\mu\nu\rangle^{(\lambda)} c_{\mu i} + \sum_{\mu} \langle \bar{k}\|\mu\nu\rangle c_{\mu i}^{(\lambda)}, \tag{3.45}$$

Eq. (3.44) can be rewritten as

$$E_x^{\mathrm{LR\text{-}F}(\lambda)} = \sum_{\mu,\nu} P_{\mu\nu}^{(\lambda)} X_{\mu\nu}^{\mathrm{LR}} + \sum_{\bar{k},\bar{l}} \Gamma_{\bar{k}\bar{l}}^{\mathrm{LR}} G_{\bar{k}\bar{l}}^{\mathrm{LR}(\lambda)} - \sum_i^{\mathrm{occ}} \sum_{\bar{k}} \sum_{\sigma} \sum_{\mu,\nu} P_{\mu\nu} x_{\bar{k}\mu i}^{\mathrm{LR}} \langle \bar{k}\|\nu\sigma\rangle^{(\lambda)} c_{\sigma i} \tag{3.46}$$

Here we have introduced the auxiliary matrix $\mathbf{\Gamma}^{\mathrm{LR}}$ with elements

$$\Gamma_{\bar{k}\bar{l}}^{\mathrm{LR}} = \frac{1}{2}\sum_i^{\mathrm{occ}} \sum_{\mu\nu} x_{\bar{k}\mu i}^{\mathrm{LR}} P_{\mu\nu} x_{\bar{l}\nu i}^{\mathrm{LR}} \tag{3.47}$$

Substituting Eqs. (3.36), (3.37) and (3.46) into Eq. (3.35) yields

$$
\begin{aligned}
E^{(\lambda)} &= \sum_{\mu,\nu} P_{\mu\nu}^{(\lambda)} K_{\mu\nu} + \sum_{\mu,\nu} P_{\mu\nu} H_{\mu\nu}^{(\lambda)} + \sum_{\mu,\nu} \sum_{\bar{k}} P_{\mu\nu} \langle \mu\nu\|\bar{k}\rangle^{(\lambda)} \left(x_{\bar{k}} + z_{\bar{k}} \right) + \\
&\quad \sum_{\bar{k},\bar{l}} x_{\bar{k}} G_{\bar{k}\bar{l}}^{(\lambda)} \left(\frac{1}{2} x_{\bar{l}} + z_{\bar{l}} \right) + \sum_{\bar{k}} x_{\bar{k}} \langle v_{xc}[\tilde{\rho}]\|\bar{k}^{(\lambda)}\rangle + c_{\mathrm{F}} \left(\alpha \sum_{\bar{k},\bar{l}} \Gamma_{\bar{k}\bar{l}} G_{\bar{k}\bar{l}}^{(\lambda)} + \right. \\
&\quad \left. \beta \sum_{\bar{k},\bar{l}} \Gamma_{\bar{k}\bar{l}}^{\mathrm{LR}} G_{\bar{k}\bar{l}}^{\mathrm{LR}(\lambda)} - \alpha \sum_i^{\mathrm{occ}} \sum_{\bar{k}} \sum_{\sigma} \sum_{\mu,\nu} P_{\mu\nu} x_{\bar{k}\mu i} \langle \bar{k}\|\nu\sigma\rangle^{(\lambda)} c_{\sigma i} - \right. \\
&\quad \left. \beta \sum_i^{\mathrm{occ}} \sum_{\bar{k}} \sum_{\sigma} \sum_{\mu,\nu} P_{\mu\nu} x_{\bar{k}\mu i}^{\mathrm{LR}} \langle \bar{k}\|\nu\sigma\rangle^{(\lambda)} c_{\sigma i} \right)
\end{aligned} \tag{3.48}
$$

The first term in Eq. (3.48) collects all derivatives of the molecular orbital coefficients and is absorbed in the Pulay forces [99]. Thus, the final expression for an ADFT energy gradient component, including global and range-separated Fock exchange is given by

$$
\begin{aligned}
E^{(\lambda)} \;=\; & -\sum_{\mu,\nu} W_{\mu\nu} S^{(\lambda)}_{\mu\nu} + \sum_{\mu,\nu} P_{\mu\nu} H^{(\lambda)}_{\mu\nu} + \sum_{\mu,\nu}\sum_{\bar{k}} P_{\mu\nu}\langle\mu\nu\|\bar{k}\rangle^{(\lambda)}\left(x_{\bar{k}}+z_{\bar{k}}\right) + \\
& \sum_{\bar{k},\bar{l}} x_{\bar{k}} G^{(\lambda)}_{\bar{k}\bar{l}}\left(\frac{1}{2}x_{\bar{l}}+z_{\bar{l}}\right) + \sum_{\bar{k}} x_{\bar{k}}\langle v_{xc}[\tilde{\rho}]|\bar{k}^{(\lambda)}\rangle + c_{F}\left(\alpha\sum_{\bar{k},\bar{l}}\Gamma_{\bar{k}\bar{l}} G^{(\lambda)}_{\bar{k}\bar{l}} + \right. \\
& \beta\sum_{\bar{k},\bar{l}}\Gamma^{LR}_{\bar{k}\bar{l}} G^{LR(\lambda)}_{\bar{k}\bar{l}} - \alpha\sum_{i}^{occ}\sum_{\bar{k}}\sum_{\sigma}\sum_{\mu,\nu} P_{\mu\nu} x_{\bar{k}\mu i}\langle\bar{k}\|\nu\sigma\rangle^{(\lambda)} c_{\sigma i} - \\
& \left. \beta\sum_{i}^{occ}\sum_{\bar{k}}\sum_{\sigma}\sum_{\mu,\nu} P_{\mu\nu} x^{LR}_{\bar{k}\mu i}\langle\bar{k}\|\nu\sigma\rangle^{(\lambda)} c_{\sigma i}\right)
\end{aligned}
$$

(3.49)

Here $W_{\mu\nu}$ is an element of the closed-shell energy-weighted density matrix

$$
W_{\mu\nu} = 2\sum_{i}^{occ}\varepsilon_{i} c_{\mu i} c_{\nu i}
$$

(3.50)

The last terms in brackets on the right hand side of Eq. (3.49) are the additions to the energy derivative when performing a range-separated hybrid calculation in comparison to pure ADFT ones. Notice that an efficient algorithm for the calculation of Fock type energy gradients was already developed in [80] and is here adapted for the derivatives of long-range Fock exchanges.

3.4   Perturbation Theory with Hybrid Functionals

In order to include Fock exchange into the auxiliary density perturbation theory (ADPT) formalism a modification of the Eirola-Nevanlinna (EN) algorithm is suggested. Because the inclusion of the external field frequency is not trivial, we start our discussion with the frequency dependent perturbed molecular orbital (MO) coefficients [21]

$$
c^{(\lambda)}_{\sigma j}(\pm\omega) = \sum_{b}^{uno} c_{\sigma b} U^{(\lambda)}_{bj}(\pm\omega)
$$

(3.51)

Here the MO transformation matrices are given by [22]

$$
U^{(\lambda)}_{bj}(\pm\omega) = \frac{\mathcal{K}^{(\lambda)}_{bj}(\pm\omega)}{\epsilon_{j}-\epsilon_{b}\mp\omega}
$$

(3.52)

Throughout this discussion, we adopt the usual convention from the literature for MO indexing, i.e. p, q, ... denote general MOs, i, j, ... are occupied (*occ*) and a, b, ... are unoccupied (*uno*) MOs. In Eq. (3.52) $\mathcal{K}_{bj}^{(\lambda)}(\pm\omega)$ refers to a perturbed Kohn-Sham matrix element in MO representation and ϵ_j and ϵ_b are the corresponding occupied and unoccupied MO energies, respectively. The external field frequencies are given by $\pm\omega$ with a phase convention accordingly to Karna and Dupuis [22]. Assuming that the basis functions are perturbation independent, i.e. $S_{\mu\nu}^{(\lambda)} = 0$, we find for the zeroth and first order orthonormality condition

$$\sum_{\mu\nu} c_{\mu p} S_{\mu\nu} c_{\mu q} = \delta_{pq} \quad \forall \quad p, q \tag{3.53}$$

$$\sum_{\mu,\nu} c_{\mu p} S_{\mu\nu} c_{\nu q}^{(\lambda)}(\pm\omega) + \sum_{\mu,\nu} c_{\mu p}^{(\lambda)}(\mp\omega) S_{\mu\nu} c_{\nu q} = 0 \quad \forall \quad p, q \tag{3.54}$$

Expanding the perturbed MO coefficients yields

$$\sum_b \sum_{\mu,\nu} c_{\mu p} S_{\mu\nu} c_{\nu b} U_{bq}^{(\lambda)}(\pm\omega) + \sum_b \sum_{\mu,\nu} U_{pb}^{(\lambda)}(\mp\omega)^T c_{\mu b} S_{\mu\nu} c_{\nu q} = 0 \quad \forall \quad p, q \tag{3.55}$$

$$\sum_b \delta_{pb} U_{bq}^{(\lambda)}(\pm\omega) + \sum_b U_{pb}^{(\lambda)}(\mp\omega)^T \delta_{bq} = 0 \quad \forall \quad p, q \tag{3.56}$$

From Eq. (3.56) follows as general relationship between the transformation matrices

$$U_{pq}^{(\lambda)}(\pm\omega) + U_{pq}^{(\lambda)}(\mp\omega)^T = 0 \quad \forall \quad p, q \tag{3.57}$$

Based on this relationship, we use the following parametrization for the MO transformation matrices

1. Case: $p \in occ$ and $q \in occ$

$$U_{ij}^{(\lambda)}(+\omega) = U_{ij}^{(\lambda)}(-\omega)^T = U_{ij}^{(\lambda)}(-\omega) = U_{ij}^{(\lambda)}(+\omega)^T \equiv 0 \tag{3.58}$$

2. Case: $p \in uno$ and $q \in uno$

$$U_{ab}^{(\lambda)}(+\omega) = U_{ab}^{(\lambda)}(-\omega)^T = U_{ab}^{(\lambda)}(-\omega) = U_{ab}^{(\lambda)}(+\omega)^T \equiv 0 \tag{3.59}$$

3. Case: $p \in uno$ and $q \in occ$

$$U_{ai}^{(\lambda)}(+\omega) + U_{ia}^{(\lambda)}(-\omega) = 0 \quad \text{and} \quad U_{ai}^{(\lambda)}(-\omega) + U_{ia}^{(\lambda)}(+\omega) = 0 \tag{3.60}$$

This parametrization yields the following structures for the transformation matrices

$$\mathbf{U}^{(\lambda)}(+\omega) = \quad
\begin{array}{cc}
 & \begin{array}{cc} i & a \end{array} \\
\begin{array}{c} i \\[2em] a \end{array} &
\left(\begin{array}{c|c}
0 & -\oplus \\ \hline
 & \\
\otimes & 0 \\
 &
\end{array} \right)
\end{array}
\quad \begin{array}{c} occ \\[2em] uno \end{array}$$

$$\mathbf{U}^{(\lambda)}(-\omega) = \quad
\begin{array}{cc}
 & \begin{array}{cc} i & a \end{array} \\
\begin{array}{c} i \\[2em] a \end{array} &
\left(\begin{array}{c|c}
0 & -\otimes \\ \hline
 & \\
\oplus & 0 \\
 &
\end{array} \right)
\end{array}
\quad \begin{array}{c} occ \\[2em] uno \end{array}$$

Based on the symmetry of the transformation matrices we need to determine $U_{ai}^{(\lambda)}(+\omega)$ and $U_{ai}^{(\lambda)}(-\omega) \; \forall \; a \in uno$ and $i \in occ$ to obtain both transformation matrices. Alternatively, we also can determine $U_{ai}^{(\lambda)}(+\omega)$ and $U_{ia}^{(\lambda)}(+\omega) \; \forall \; a \in uno$ and $i \in occ$. These both approaches are equivalent. Thus, for a given pair of frequencies, for example $\pm\omega$, we only need to compute either the $\mathcal{K}$ matrix for $+\omega$ or $-\omega$.

Following this argumentation, we use McWeeny's self-consistent perturbation (SCP) theory [100–102] for the $+\omega$ branch to obtain the elements of the dynamic first-order perturbed closed-shell density matrix as

$$P_{\mu\nu}^{(\lambda)}(\omega) = 2 \sum_{i}^{occ} \sum_{a}^{uno} \frac{\mathcal{K}_{ai}^{(\lambda)}(\omega)}{\epsilon_i - \epsilon_a - \omega} c_{\mu a} c_{\nu i} + 2 \sum_{i}^{occ} \sum_{a}^{uno} \frac{\mathcal{K}_{ia}^{(\lambda)}(\omega)}{\epsilon_i - \epsilon_a + \omega} c_{\mu i} c_{\nu a} \qquad (3.61)$$

Here

$$\mathcal{K}_{ai}^{(\lambda)}(\omega) = \sum_{\mu,\nu} c_{\mu a} K_{\mu\nu}^{(\lambda)}(\omega) c_{\nu i} \qquad (3.62)$$

and

$$\mathcal{K}_{ia}^{(\lambda)}(\omega) = \sum_{\mu,\nu} c_{\mu i} K_{\mu\nu}^{(\lambda)}(\omega) c_{\nu a} \qquad (3.63)$$

denote first-order perturbed Kohn-Sham matrix elements in molecular orbital representation. The $c_{\mu i}$ and $c_{\nu a}$ are the canonical MO coefficients and ϵ_i and ϵ_a are the corresponding orbital

energies of the ith occupied and a^{th} unoccupied MO, respectively. The first-order perturbed range-separated hybrid ADFT Kohn-Sham matrix elements are given by

$$K_{\mu\nu}^{(\lambda)}(\omega) = H_{\mu\nu}^{(\lambda)} + \sum_{\bar{k}} \langle \mu\nu \| \bar{k} \rangle \left[x_{\bar{k}}^{(\lambda)}(\omega) + z_{\bar{k}}^{(\lambda)}(\omega) \right] + c_{\mathrm{F}} \left[\alpha X_{\mu\nu}^{F\,(\lambda)}(\omega) + \beta X_{\mu\nu}^{\mathrm{LR\text{-}F}(\lambda)}(\omega) \right] \quad (3.64)$$

The here appearing perturbed core-Hamilton matrix elements, $H_{\mu\nu}^{(\lambda)}$, depend on the particular perturbation being studied. In Eq. (3.64) $\mathbf{x}^{(\lambda)}(\omega)$ corresponds to the first-order perturbed Coulomb fitting coefficients. The corresponding first-order perturbed exchange correlation fitting coefficients can be expressed as

$$z_{\bar{k}}^{(\lambda)}(\omega) = \sum_{\bar{l}} F_{\bar{k}\bar{l}} x_{\bar{l}}^{(\lambda)}(\omega) \quad (3.65)$$

with the kernel response matrix

$$F_{\bar{k}\bar{l}} = \sum_{\bar{m}} G_{\bar{k}\bar{m}}^{-1} \langle \bar{m} | f_{xc}[\tilde{\rho}] | \bar{l} \rangle \quad (3.66)$$

where $f_{xc}[\tilde{\rho}]$ is the second functional derivative of the exchange-correlation energy functional. The perturbed (closed-shell) global and long-range Fock potentials are given by

$$X_{\mu\nu}^{\mathrm{F}\,(\lambda)}(\omega) = -\frac{1}{2} \sum_{\sigma,\tau} \sum_{\bar{k},\bar{l}} P_{\sigma\tau}^{(\lambda)}(\omega) \langle \mu\sigma \| \bar{k} \rangle G_{\bar{k}\bar{l}}^{-1} \langle \bar{l} \| \tau\nu \rangle \quad (3.67)$$

$$X_{\mu\nu}^{\mathrm{LR\text{-}F}(\lambda)}(\omega) = -\frac{1}{2} \sum_{\sigma,\tau} \sum_{\bar{k},\bar{l}} P_{\sigma\tau}^{(\lambda)}(\omega) \langle \mu\sigma \underline{\|} \bar{k} \rangle G_{\bar{k}\bar{l}}^{\mathrm{LR}\,-1} \langle \bar{l} \underline{\|} \tau\nu \rangle \quad (3.68)$$

The here appearing perturbed density matrix elements have the form

$$P_{\sigma\tau}^{(\lambda)}(\omega) = 2 \sum_{i}^{occ} c_{\sigma i}^{(\lambda)}(+\omega) c_{\tau i} + 2 \sum_{i}^{occ} c_{\sigma i} c_{\tau i}^{(\lambda)}(-\omega) \quad (3.69)$$

with

$$c_{\sigma i}^{(\lambda)}(+\omega) = \sum_{a}^{uno} \frac{\mathcal{K}_{ai}^{(\lambda)}(\omega)}{\epsilon_i - \epsilon_a - \omega} c_{\sigma a} \quad (3.70)$$

and

$$c_{\sigma i}^{(\lambda)}(-\omega) = \sum_{a}^{uno} \frac{\mathcal{K}_{ia}^{(\lambda)}(\omega)}{\epsilon_i - \epsilon_a + \omega} c_{\sigma a} \quad (3.71)$$

At this point we emphasize that $c_{\sigma i}^{(\lambda)}(+\omega)$ and $c_{\sigma i}^{(\lambda)}(-\omega)$ are used merely as a convenient notation and that they are calculated within the $+\omega$ branch. Substituting Eq. (3.69) into

Eq. (3.67) yields

$$
\begin{aligned}
X_{\mu\nu}^{\mathrm{F}\ (\lambda)}(\omega) &= -\sum_{\bar{k},\bar{l}}\sum_{i}^{occ} c_{\sigma i}^{(\lambda)}(+\omega)c_{\tau i}\langle\mu\sigma\|\bar{k}\rangle G_{\bar{k}\bar{l}}^{-1}\langle\bar{l}\|\tau\nu\rangle \\
&\quad -\sum_{\bar{k},\bar{l}}\sum_{i}^{occ} c_{\sigma i}c_{\tau i}^{(\lambda)}(-\omega)\langle\mu\sigma\|\bar{k}\rangle G_{\bar{k}\bar{l}}^{-1}\langle\bar{l}\|\tau\nu\rangle \\
&= -\sum_{\bar{k},\bar{l}}\sum_{i}^{occ}\langle\mu\psi_{i}^{(\lambda)}(+\omega)\|\bar{k}\rangle G_{\bar{k}\bar{l}}^{-1}\langle\bar{l}\|\psi_{i}\nu\rangle \\
&\quad -\sum_{\bar{k},\bar{l}}\sum_{i}^{occ}\langle\mu\psi_{i}\|\bar{k}\rangle G_{\bar{k}\bar{l}}^{-1}\langle\bar{l}\|\psi_{i}^{(\lambda)}(-\omega)\nu\rangle
\end{aligned}
\tag{3.72}
$$

Analogously, we find for the perturbed long-range Fock exchange potential

$$
\begin{aligned}
X_{\mu\nu}^{\mathrm{LR\text{-}F}(\lambda)}(\omega) &= -\sum_{\bar{k},\bar{l}}\sum_{i}^{occ}\langle\mu\psi_{i}^{(\lambda)}(+\omega)\|\underline{\bar{k}}\rangle G_{\bar{k}\bar{l}}^{\mathrm{LR}^{-1}}\langle\underline{\bar{l}}\|\psi_{i}\nu\rangle \\
&\quad -\sum_{\bar{k},\bar{l}}\sum_{i}^{occ}\langle\mu\psi_{i}\|\underline{\bar{k}}\rangle G_{\bar{k}\bar{l}}^{\mathrm{LR}^{-1}}\langle\underline{\bar{l}}\|\psi_{i}^{(\lambda)}(-\omega)\nu\rangle
\end{aligned}
\tag{3.73}
$$

Note that the localization of $\psi_i(\mathbf{r})$ is possible in the calculation of $X_{\mu\nu}^{\mathrm{F}\ (\lambda)}(\omega)$ and $X_{\mu\nu}^{\mathrm{LR\text{-}F}(\lambda)}(\omega)$. To do so $\psi_i^{(\lambda)}(\pm\omega,\mathbf{r})$ must be transformed with the localization matrix for the canonical MOs obtained from the foregoing SCF.

To find an expression for the calculation of the first-order perturbed Coulomb fitting coefficients we combine Eq. (3.61) with the derivative of the fitting equation, Eq. (2.10)

$$
\sum_{\bar{k}} G_{\bar{n}\bar{k}} x_{\bar{k}}^{(\lambda)}(\omega) = \sum_{\mu,\nu}\langle\bar{n}\|\mu\nu\rangle P_{\mu\nu}^{(\lambda)}(\omega)
\tag{3.74}
$$

Inserting the perturbed density matrix elements of Eq. (3.61) into Eq. (3.74) and expanding the perturbed Kohn-Sham matrix elements yields

$$
\begin{aligned}
\sum_{\bar{k}} G_{\bar{n}\bar{k}} x_{\bar{k}}^{(\lambda)}(\omega) &= 2\sum_{i}^{occ}\sum_{a}^{uno} \langle \bar{n}\| \, ai\rangle \frac{\mathcal{K}_{ai}^{(\lambda)}(\omega)}{\epsilon_i - \epsilon_a - \omega} + 2\sum_{i}^{occ}\sum_{a}^{uno}\langle \bar{n}\|ia\rangle \frac{\mathcal{K}_{ia}^{(\lambda)}(\omega)}{\epsilon_i - \epsilon_a + \omega} \\
&= 2\sum_{i}^{occ}\sum_{a}^{uno} \frac{\langle \bar{n}\|ai\rangle}{\epsilon_i - \epsilon_a + \omega}\left(\mathcal{H}_{ai}^{(\lambda)} + \sum_{\bar{k}} \langle ai\|\bar{k}\rangle \left[x_{\bar{k}}^{(\lambda)}(\omega) + z_{\bar{k}}^{(\lambda)}(\omega)\right] + \right. \\
&\quad \left. c_{\mathrm{F}}\left[\alpha \mathcal{X}_{ai}^{F(\lambda)}(\omega) + \beta \mathcal{X}_{ai}^{\mathrm{LR}\text{-}\mathrm{F}(\lambda)}(\omega)\right]\right) + \\
&\quad 2\sum_{i}^{occ}\sum_{a}^{uno}\frac{\langle \bar{n}\|ia\rangle}{\epsilon_i - \epsilon_a + \omega}\left(\mathcal{H}_{ia}^{(\lambda)} + \sum_{\bar{k}}\langle ia\|\bar{k}\rangle \left[x_{\bar{k}}^{(\lambda)}(\omega) + z_{\bar{k}}^{(\lambda)}(\omega)\right] + \right. \\
&\quad \left. c_{\mathrm{F}}\left[\alpha \mathcal{X}_{ia}^{F(\lambda)}(\omega) + \beta \mathcal{X}_{ia}^{\mathrm{LR}\text{-}\mathrm{F}(\lambda)}(\omega)\right]\right) \\
&= 4\sum_{i}^{occ}\sum_{a}^{uno}\langle \bar{n}\|ia\rangle \frac{\omega_{ia}}{\omega_{ia}^2 + \omega^2}\mathcal{H}_{ia}^{(\lambda)} + \\
&\quad 4\sum_{\bar{k}}\sum_{i}^{occ}\sum_{a}^{uno}\langle \bar{n}\|ia\rangle \frac{\omega_{ia}}{\omega_{ia}^2 + \omega^2}\langle ia\|\bar{k}\rangle x_{\bar{k}}^{(\lambda)}(\omega) + \\
&\quad 4\sum_{\bar{k},\bar{l}}\sum_{i}^{occ}\sum_{a}^{uno}\langle \bar{n}\|ia\rangle \frac{\omega_{ia}}{\omega_{ia}^2 + \omega^2}\langle ia\|\bar{k}\rangle F_{\bar{k}\bar{l}} x_{\bar{l}}^{(\lambda)}(\omega) + \\
&\quad 2c_{\mathrm{F}}\sum_{i}^{occ}\sum_{a}^{uno}\langle \bar{n}\|ia\rangle \left[\frac{\alpha \mathcal{X}_{ai}^{F(\lambda)}(\omega) + \beta \mathcal{X}_{ai}^{\mathrm{LR}\text{-}\mathrm{F}(\lambda)}(\omega)}{\omega_{ia} - \omega} + \right. \\
&\quad \left. \frac{\alpha \mathcal{X}_{ia}^{F(\lambda)}(\omega) + \beta \mathcal{X}_{ia}^{\mathrm{LR}\text{-}\mathrm{F}(\lambda)}(\omega)}{\omega_{ia} + \omega}\right]
\end{aligned}
\tag{3.75}
$$

To ease notation we used $\omega_{ia} = \epsilon_i - \epsilon_a$. The perturbed Fock potential terms in molecular orbital representation are given by

$$
\mathcal{X}_{ai}^{\mathrm{F}(\lambda)}(\omega) = \sum_{\mu,\nu} c_{\mu a} X_{\mu\nu}^{\mathrm{F}\,(\lambda)}(\omega) c_{\nu i}
\tag{3.76}
$$

$$
\mathcal{X}_{ia}^{\mathrm{LR}\text{-}\mathrm{F}(\lambda)}(\omega) = \sum_{\mu,\nu} c_{\mu i} X_{\mu\nu}^{\mathrm{F}\,(\lambda)}(\omega) c_{\nu a}
\tag{3.77}
$$

$$
\mathcal{X}_{ai}^{\mathrm{LR}\text{-}\mathrm{F}(\lambda)}(\omega) = \sum_{\mu,\nu} c_{\mu a} X_{\mu\nu}^{\mathrm{F}\,(\lambda)}(\omega) c_{\nu i}
\tag{3.78}
$$

$$
\mathcal{X}_{ia}^{\mathrm{LR}\text{-}\mathrm{F}(\lambda)}(\omega) = \sum_{\mu,\nu} c_{\mu i} X_{\mu\nu}^{\mathrm{LR}\text{-}\mathrm{F}(\lambda)}(\omega) c_{\nu a}
\tag{3.79}
$$

To proceed, we now introduce the elements of the Coulomb response matrix $\mathbf{A}(\omega)$ and the perturbation vectors $\mathbf{b}^{(\lambda)}(\omega)$ and $\overset{\bullet}{\mathbf{b}}^{(\lambda)}(\omega)$

$$A_{\bar{n}\bar{k}}(\omega) = \sum_i^{occ} \sum_a^{uno} \langle \bar{n}\|ia\rangle \frac{\omega_{ia}}{\omega_{ia}^2 + \omega^2} \langle ia\|\bar{k}\rangle \tag{3.80}$$

$$b_n^{(\lambda)}(\omega) = \sum_i^{occ} \sum_a^{uno} \langle \bar{n}\|ia\rangle \frac{\omega_{ia}}{\omega_{ia}^2 + \omega^2} \mathcal{H}_{ia}^{(\lambda)} \tag{3.81}$$

$$\overset{\bullet}{b}_{\bar{n}}^{(\lambda)}(\omega) = c_{\mathrm{F}} \sum_i^{occ} \sum_a^{uno} \langle \bar{n}\|ia\rangle \left[\frac{\alpha \mathcal{X}_{ai}^{F(\lambda)}(\omega) + \beta \mathcal{X}_{ai}^{\mathrm{LR}\text{-}\mathrm{F}(\lambda)}(\omega)}{\omega_{ia} - \omega} + \frac{\alpha \mathcal{X}_{ia}^{F(\lambda)}(\omega) + \beta \mathcal{X}_{ia}^{\mathrm{LR}\text{-}\mathrm{F}(\lambda)}(\omega)}{\omega_{ia} + \omega} \right] \tag{3.82}$$

Rearranging Eq. (3.75) yields the following linear equation system for $\mathbf{x}^{(\lambda)}(\omega)$ in matrix form

$$[\mathbf{G} - 4\mathbf{A}(\omega) - 4\mathbf{A}(\omega)\mathbf{F}]\,\mathbf{x}^{(\lambda)}(\omega) = \mathbf{R}(\omega)\,\mathbf{x}^{(\lambda)}(\omega) = 4\mathbf{b}^{(\lambda)}(\omega) + 2\overset{\bullet}{\mathbf{b}}^{(\lambda)}(\omega) \tag{3.83}$$

This is the ADPT equation system for global and range-separated hybrid functionals. Note that the perturbation vector $\overset{\bullet}{\mathbf{b}}^{(\lambda)}(\omega)$ depends on the perturbed fitting coefficients. Therefore, Eq (3.83) must be solved iteratively. To this end, we use the Eirola-Nevanlinna (EN) algorithm [103, 104] in order to obtain the perturbed Coulomb fitting coefficients, $\mathbf{x}^{(\lambda)}(\omega)$. Once these coefficients are obtained, the perturbed exchange correlation fitting coefficients, $\mathbf{z}^{(\lambda)}(\omega)$, are readily available via Eq. (3.65). The basic quantity for the calculation of $\overset{\bullet}{\mathbf{b}}^{(\lambda)}(\omega)$ are the perturbed global and long-range Fock potentials given by Eqs. (3.67) and (3.68). These matrix elements are also needed for the calculation of the perturbed Kohn-Sham matrix elements, Eq. (3.64). With the perturbed Kohn-Sham matrix elements the pertubed MO coefficients $c_{\sigma i}^{(\lambda)}(+\omega)$ and $c_{\sigma i}^{(\lambda)}(-\omega)$ can be calculated according to Eq. (3.70) and (3.71) which in turn permits the calculation of new perturbed global and long-range Fock potentials. This closes the iterative loop for the perturbed Fock potential calculation.

A flowchart of the modified EN algorithm is depicted in Fig. 3.3. The ADPT equation systems solved by EN micro iterations are dark violet underlaid. In the initialization step (top of Fig. 3.3) a LDA/GGA like ADPT equation system is solved, i.e. $\overset{\bullet}{\mathbf{b}}^{(\lambda)}(\omega) = 0$ is used. From this solution the first set of perturbed MO coefficients is calculated according to Eq. (3.70) and (3.71). Note that the Fock contribution is still set to zero. Once the perturbed MO coefficients are calculated, the corresponding perturbed Fock potentials are calculated according to (3.72) and (3.73) and stored on tape. In turn the Fock dependent

part of the perturbation vector, $\overset{\bullet}{\mathbf{b}}{}^{(\lambda)}(\omega)$, is calculated and a new ADPT equation system is solved with the EN algorithm. The obtained perturbed fitting coefficients, together with the reloaded perturbed Fock potentials (top HD in Fig 3.3), are used for the calculations of the new perturbed Kohn-Sham matrix elements and the new perturbed MO coefficients. Thus, the perturbed Fock potentials are always 1 macro iteration behind the perturbed fitting coefficients. With the calculation of the new perturbed Fock potential a new macro iteration starts. After the new Fock dependent part of the perturbation vector is calculated, the new ADPT equation system is solved by EN micro iterations. Convergence is reached after the calculation of the next perturbed Kohn-Sham matrix. Once the convergence is reached the perturbed density matrix is calculated according to (3.61).

There are several particular cases worth mentioning. If $\alpha = 1.0$ and $\beta = 0.0$ we obtain the perturbation vector $\overset{\bullet}{\mathbf{b}}{}^{(\lambda)}(\omega)$ for global hybrid functionals. If additionally $z_{\tilde{k}}^{(\lambda)}(\omega) = 0$ and $c_\mathrm{F} = 1.0$ Hartree-Fock perturbation theory is recovered. Thus, the here discussed ADPT formalism can be also used as an alternative to the coupled perturbed Hartree-Fock (CPHF) approach. Of course, if no Fock exchange potential exists Eq. (3.83) reduces to the well-known ADPT equation system for LDA and GGA functionals

$$\left[\mathbf{G} - 4\mathbf{A}(\omega) - 4\mathbf{A}(\omega)\mathbf{F} \right] \mathbf{x}^{(\lambda)}(\omega) = 4\mathbf{b}^{(\lambda)}(\omega) \tag{3.84}$$

For $\omega = 0$ the equation system for global and range-separated hybrid functionals, Eq. (3.83), reduces to its static counterpart. In fact, the ω dependency of the Coulomb coupling matrix and of the perturbation vector can be easily incorporated into the static matrix and vector element calculations. As a result, the computational performance for static and dynamic ADPT polarizabilities is very similar.
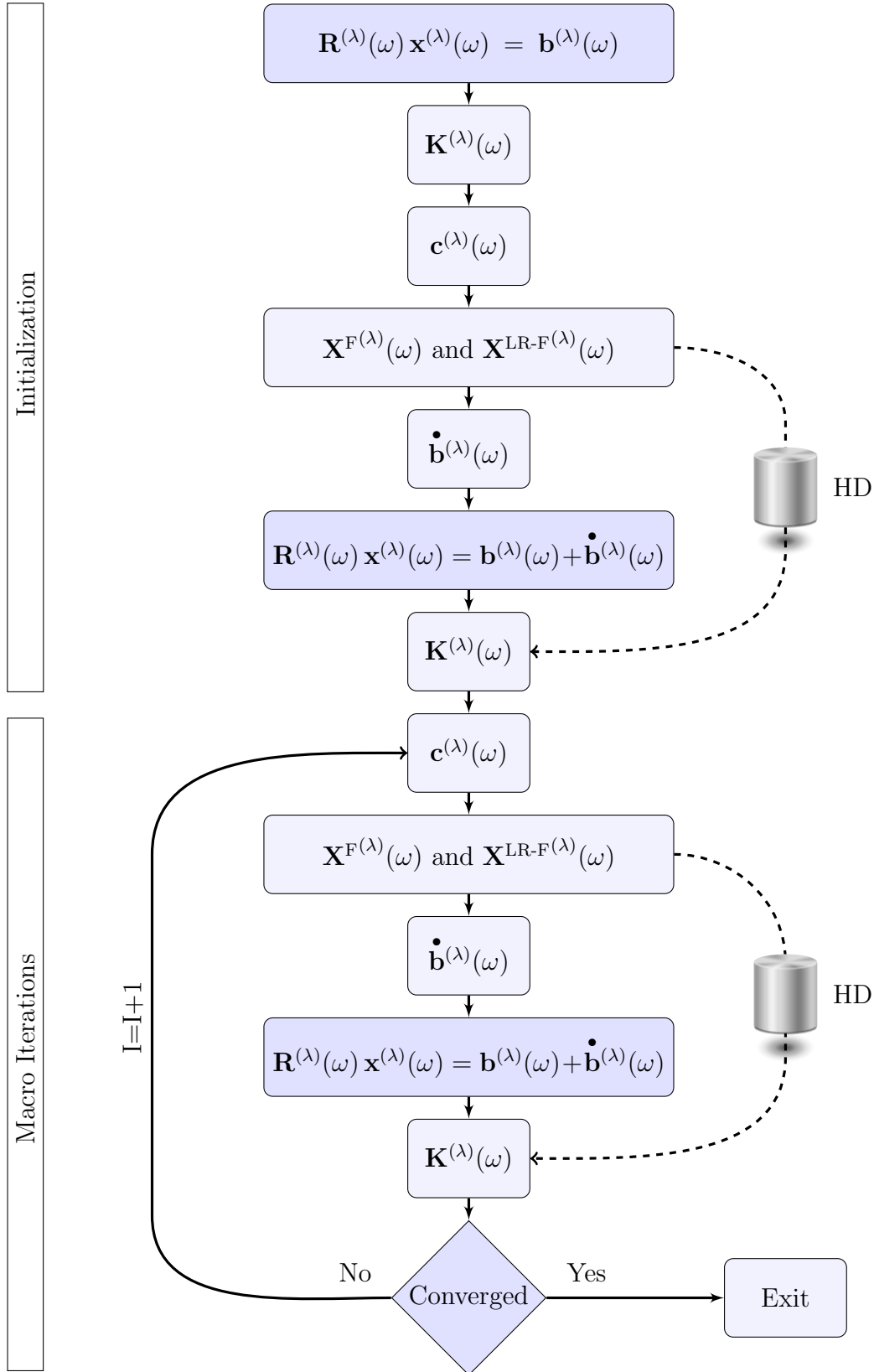
Figure 3.3: Flow chart of the modified EN algorithm for global and range-separated hybrid calculations. Dashed lines indicate storage/loading operations from hard drive (HD). See text for further details.

Implementation, Validation and Benchmarks

In this chapter we will give the details for the implementation as well as the validation of the range-separated hybrid functionals in the ADFT and ADPT frameworks. Also, a parallel implementation is presented and benchmarked.

4.1 Implementation

4.1.1 Basic Integrals for Range-Separated Fock Exchange

In our variational fitting approach the basic primitive three-center LR ERI is given as

$$[\mathbf{ab}\|\bar{\mathbf{c}}] = \iint \mathbf{a}(\mathbf{r})\mathbf{b}(\mathbf{r})\frac{\mathrm{erf}(\omega|\mathbf{r}-\mathbf{r}'|)}{|\mathbf{r}-\mathbf{r}'|}\bar{\mathbf{c}}(\mathbf{r}')\ d\mathbf{r}\ d\mathbf{r}' \tag{4.1}$$

Here $\mathbf{a}$ and $\mathbf{b}$ denote (unnormalized) primitive atom centered Cartesian Gaussian type functions of the form

$$\mathbf{a}(\mathbf{r}) = (x-A_x)^{a_x}(y-A_y)^{a_y}(z-A_z)^{a_z}e^{-\zeta_a(\mathbf{r}-\mathbf{A})^2} \tag{4.2}$$

and $\bar{\mathbf{c}}$ is a atom centered (unnormalized) primitive Hermite Gaussian function given by Eq. (2.3). Using the definition of the error function, the long-range Coulomb operator, Eq. (3.8), can be rewritten as

$$\| = \frac{2}{\sqrt{\pi}|\mathbf{r}-\mathbf{r}'|}\int_0^{\omega|\mathbf{r}-\mathbf{r}'|} e^{-t^2}dt \tag{4.3}$$

With the variable substitution

$$u = \frac{t}{\omega|\mathbf{r}-\mathbf{r}'|} \tag{4.4}$$

follows for the long-range Coulomb operator

$$\| = \frac{2\omega}{\sqrt{\pi}}\int_0^1 e^{-u^2\omega^2(\mathbf{r}-\mathbf{r}')^2}du \tag{4.5}$$

In Eq. (4.5), the long-range Coulomb operator is written in Gaussian form. Therefore, we can apply the Gaussian product theorem (GPT). The GPT states that the product of two Gaussian functions at centers $\mathbf{A}$ and $\mathbf{B}$ yields a Gaussian function with center $\mathbf{P}$ on the line that connects $\mathbf{A}$ and $\mathbf{B}$ [105]. Thus, the basic integral, Eq. (4.1), over s functions takes the form

$$[\bar{s}]^{(0)} = \iiint_0^1 e^{-\zeta_a(\mathbf{r}-\mathbf{A})^2} e^{-\zeta_b(\mathbf{r}-\mathbf{B})^2} e^{-u^2\omega^2(\mathbf{r}-\mathbf{r}')^2} e^{-\zeta_{\bar{c}}(\mathbf{r}'-\mathbf{C})^2}\, du\, d\mathbf{r}\, d\mathbf{r}' \tag{4.6}$$

Applying the GPT to compute new centers, the final expression for the basic integral of the long-range three-center ERIs is given by [106]

$$[\bar{s}]^{(n)} = \frac{2\omega\pi^{5/2}}{\sqrt{(\zeta_a+\zeta_b)\zeta_{\bar{c}} + \omega^2(\zeta_a+\zeta_b+\zeta_{\bar{c}})}} \frac{(-2\eta_\omega)^n}{(\zeta_a+\zeta_b)\zeta_{\bar{c}}} e^{-\xi(\mathbf{A}-\mathbf{B})^2} F_n(T_{\eta_\omega}) \tag{4.7}$$

with

$$\eta_\omega = -\frac{\omega^2(\zeta_a+\zeta_b)\zeta_{\bar{c}}}{(\zeta_a+\zeta_b)\zeta_{\bar{c}} + \omega^2(\zeta_a+\zeta_b+\zeta_{\bar{c}})}, \qquad T_{\eta_\omega} = \eta_\omega(\mathbf{P}-\mathbf{C})^2, \tag{4.8}$$

where

$$\mathbf{P} = \frac{\zeta_a\mathbf{A}+\zeta_b\mathbf{B}}{\zeta_a+\zeta_b}, \qquad \xi = \frac{\zeta_a\zeta_b}{\zeta_a+\zeta_b}. \tag{4.9}$$

Here $\mathbf{A}$ and $\mathbf{B}$ are the centers of the primitive Cartesian Gaussian functions with exponents ζ_a and ζ_b respectively, and $\mathbf{C}$ is the center of the primitive Hermite Gaussian type auxiliary function with exponent $\zeta_{\bar{c}}$. The so-called Boys function in Eq. (4.7) is ω dependent over its argument and has the form

$$F_n(T_{\eta_\omega}) = \int_0^1 t^{2n} e^{T_{\eta_\omega}t^2} dt \tag{4.10}$$

Similar to standard three-center ERIs, LR three-center ERIs can also be asymptotically expanded by introducing a LR electrostatic potential for the primitive Hermite Gaussian auxiliary functions,

$$\phi_{\bar{c}}(\mathbf{r}) = \int \frac{\mathrm{erf}(\omega|\mathbf{r}-\mathbf{r}'|)}{|\mathbf{r}-\mathbf{r}'|} \bar{c}(\mathbf{r}')\, d\mathbf{r}' \tag{4.11}$$

Following the same arguments as in reference [40] the asymptotic expansion for the LR electrostatic potential of a $\bar{s}$ type auxiliary function is given by

$$\|\bar{s}]^{(0)} \sim \left(\frac{\pi}{\zeta_{\bar{c}}}\right)^{3/2} \frac{1}{|\mathbf{r}-\mathbf{C}|} \tag{4.12}$$

Thus, LR three-center ERIs have the same asymptotic expansion as their standard counterpart. However, it should be noted that the number of asymptotically expanded ERIs [41] is

much smaller for LR Fock exchange fitting than for the corresponding Coulomb fitting due to the intrinsic local nature of LR Fock exchange, that is exploited in our algorithm by the use of localized MOs.

For the calculation of the long-range Coulomb matrix elements, appearing in Eq. (3.23), two-center LR ERIs over primitive Hermite Gaussian functions are needed. These (unnormalized) integrals are

$$[\bar{\mathbf{c}}\underline{\|}\bar{\mathbf{d}}] = \iint \bar{\mathbf{c}}(\mathbf{r})\frac{\mathrm{erf}(\omega|\mathbf{r}-\mathbf{r}'|)}{|\mathbf{r}-\mathbf{r}'|}\bar{\mathbf{d}}(\mathbf{r}')\ d\mathbf{r}\ d\mathbf{r}' \tag{4.13}$$

Using Eq. (4.5) the above basic integral over $\bar{s}$ functions takes the form

$$[\bar{s}]^{(0)} = \iint\int_0^1 e^{-\zeta_{\bar{c}}(\mathbf{r}-\mathbf{C})^2}e^{-u^2\omega^2(\mathbf{r}-\mathbf{r}')^2}e^{-\zeta_{\bar{d}}(\mathbf{r}'-\mathbf{D})^2}\ du\ d\mathbf{r}\ d\mathbf{r}' \tag{4.14}$$

The basic LR integral of the corresponding recurrence relation is given by

$$[\bar{s}]^{(n)} = \frac{2\pi^{5/2}}{\zeta_{\bar{c}}\zeta_{\bar{d}}}\frac{\omega(-2\vartheta_\omega)^n}{[\zeta_{\bar{c}}\zeta_{\bar{d}}+\omega^2(\zeta_{\bar{c}}+\zeta_{\bar{d}})]^{1/2}}F_n(T_{\vartheta_\omega}) \tag{4.15}$$

with

$$\vartheta_\omega = -\frac{\omega^2\zeta_{\bar{c}}\zeta_{\bar{d}}}{\zeta_{\bar{c}}\zeta_{\bar{d}}+\omega^2(\zeta_{\bar{c}}+\zeta_{\bar{d}})}\quad\text{and}\quad T_{\vartheta_\omega}=\vartheta_\omega(\mathbf{C}-\mathbf{D})^2 \tag{4.16}$$

In range-separated hybrid ADFT calculations, Fock exchange energy, potential, gradient and perturbed potential depend on the computation of two- and three-center ERIs. The expression of the basic ERIs, Eqs. (4.7) and (4.15) have the same form as for conventional ERIs [39, 40], except for a correction term depending on the attenuation parameter ω. Thus, we can combine conventional and range-separated ERIs at the level of basic integrals. This yields for the three-center ERIs

$$[\bar{s}]^{(n)} = \left(\frac{\alpha(-2\eta)^nF_n(T_\eta)}{\sqrt{\zeta_a+\zeta_b+\zeta_{\bar{c}}}} - \frac{\beta\omega(-2\eta_\omega)^nF_n(T_{\eta_\omega})}{\sqrt{(\zeta_a+\zeta_b)\zeta_{\bar{c}}+\omega^2(\zeta_a+\zeta_b+\zeta_{\bar{c}})}}\right)\left(\frac{2\pi^{5/2}}{\zeta_{\bar{c}}(\zeta_a+\zeta_b)}e^{-\xi(\mathbf{A}-\mathbf{B})^2}\right) \tag{4.17}$$

with

$$\eta = -\frac{(\zeta_a+\zeta_b)\zeta_{\bar{c}}}{\zeta_a+\zeta_b+\zeta_{\bar{c}}},\qquad T_\eta=\eta(\mathbf{P}-\mathbf{C})^2, \tag{4.18}$$

The corresponding basic two-center range-separated ERIs are given by

$$[\bar{s}]^{(n)} = \frac{2\pi^{5/2}}{\zeta_{\bar{c}}\zeta_{\bar{d}}}\left(\frac{\alpha(-2\vartheta)^nF_n(T_\vartheta)}{\sqrt{\zeta_{\bar{c}}+\zeta_{\bar{d}}}} - \frac{\beta\omega(-2\vartheta_\omega)^nF_n(T_{\theta_\omega})}{\sqrt{\zeta_{\bar{c}}\zeta_{\bar{d}}+\omega^2(\zeta_{\bar{c}}+\zeta_{\bar{d}})}}\right) \tag{4.19}$$

with

$$\vartheta = -\frac{\zeta_{\bar{c}}\zeta_{\bar{d}}}{\zeta_{\bar{c}} + \zeta_{\bar{d}}}, \qquad T = \vartheta(\mathbf{C} - \mathbf{D})^2 \qquad (4.20)$$

In Eqs. (4.17) and (4.19), α and β are the range-separation parameters. With these basic integrals the standard recurrence relations [40, 41] can be used to compute the ERIs for range-separated Fock exchange. Therefore, ERI calculations for range-separated Fock exchange is of similar computational demand as for standard Fock exchange.

4.1.2   Parallelization Scheme for Fock Exchange ERI Calulation

To improve workload balance with respect to the octree parallelization algorithm [80] a new two step parallelization scheme was developed. In the first step the three-center ERIs $\langle \mu\nu \| \bar{k} \rangle$ are calculated. Here the workload is distributed over the shell combinations to which the atomic orbitals μ and ν belong. The different shell combinations are distributed equally over the computational cores and the calculated integrals are stored locally as partial contributions to the ERIs $\langle \mu\psi_i \| \bar{k} \rangle$ in RAM. These contributions from different cores are then summed up to build the target ERIs $\langle \mu\psi_i \| \bar{k} \rangle$. After this step the work is redistributed over the occupied LMO index i in such a way that at the end each core processes about the same number of $\langle \mu\psi_i \| \bar{k} \rangle$ integrals. This distribution over the LMO index i is also used for the calculation of the long-range Fock potential $X_{\mu\nu}^{LR}$. Note that the first distribution for the calculation of the $\langle \mu\nu \| \bar{k} \rangle$ integrals can become RAM demanding due to the storage of $\langle \mu\psi_i \| \bar{k} \rangle$ ERIs [107]. Therefore, integral batching is introduced. In case RAM demand exceeds the physical available memory, the occupied LMOs are split into batches and the $\langle \mu\nu \| \bar{k} \rangle$ ERIs are recalculated for each batch. The final results of each batch are added sequentially to the long-range Fock potential $X_{\mu\nu}^{LR}$. This approach provides a good compromise between RAM demand and computational efficiency.

Serial and parallel calculations have shown that the computation of the inverse of the local Coulomb matrix, $\mathbf{G}_i$, i denoting the corresponding occupied LMO, can be a bottleneck in the computation of range-separated Fock potentials [106]. In the original deMon2k implementation of the variational fitting of Fock exchange this inverse was calculated either by Cholesky decomposition or, when this fails, by TED. From a computational point of view it is desirable to avoid TED altogether. To this end, we propose here the use of a modified

Cholesky decomposition for the calculation of the inverse of the $\mathbf{G}_i$ matrices. To ease the notation, we introduce a set of matrices $\mathbf{E}_i$ with elements

$$E_{\mu\bar{k},i} = \langle \mu i \| \bar{k} \rangle \tag{4.21}$$

In general, all $\mathbf{E}_i$ matrices have different dimensions due to the local fitting domains. In addition, each LMO has an associate Coulomb matrix $\mathbf{G}_i$ either global or range separated, $\mathbf{G}^{\mathrm{F}}/\mathbf{G}^{\mathrm{LR}}$. The contribution of each LMO to the Fock potential matrix $\mathbf{X}$ is given by

$$\mathbf{X}_i = -\mathbf{E}_i \mathbf{G}_i^{-1} \mathbf{E}_i^T \tag{4.22}$$

We use $\mathbf{X}_i$ or $\mathbf{X}$ as generic representation for $\mathbf{X}_i^{\mathrm{F}}/\mathbf{X}_i^{\mathrm{LR}}$ and $\mathbf{X}^{\mathrm{F}}/\mathbf{X}^{\mathrm{LR}}$. Note that in general $\mathbf{X}_i$ and $\mathbf{X}$ will have different dimensions.

If the matrix $\mathbf{G}_i$ is positive definite we can always find a decomposition of the form $\mathbf{G}_i = \mathbf{L}_i \mathbf{D}_i \mathbf{L}_i^T$, where $\mathbf{L}_i$ is a unit lower triangular matrix and $\mathbf{D}_i$ is a diagonal matrix with strictly positive diagonal entries. However, if $\mathbf{G}_i$ is positive semidefinite, $\mathbf{D}_i$ may have zero elements on the diagonal and the decomposition is no longer unique [108]. We can, however, find a permutation matrix $\mathbf{P}_i$ such that $\mathbf{P}_i \mathbf{G}_i \mathbf{P}_i^T$ has a unique decomposition of the form $\mathbf{L}_i \mathbf{D}_i \mathbf{L}_i^T$, with

$$\mathbf{D}_i = \begin{pmatrix} \mathbf{D}_1 & 0 \\ 0 & 0 \end{pmatrix} \tag{4.23}$$

where $\mathbf{D}_1$ is a square diagonal matrix with positive diagonal elements. The dimension of $\mathbf{D}_1$ is r, where r is the rank of $\mathbf{G}_i$. Thus, this decompostion is useful for its rank-revealing property [108] and extends the Cholesky decomposition to all positive semidefinite matrices. Several *modified* Cholesky algorithms exist that aim to compensate for the lack of positive definiteness. The basic idea is to perturb $\mathbf{G}_i$, i.e. add a matrix $\mathbf{H}_i$ to it, to make it positive definite and then find a Cholesky decomposition of this perturbed matrix instead. The challenge is to do this in such a way that the perturbed matrix remains pertinent to the original application.

In practice, we usually need to perform pivoting on the matrix being decomposed to ensure numerical stability. Thus, we actually calculate the decomposition

$$\mathbf{P}_i(\mathbf{G}_i + \mathbf{H}_i)\mathbf{P}_i^T = \mathbf{L}_i \mathbf{D}_i \mathbf{L}_i^T \tag{4.24}$$

where $\mathbf{P}_i$ is an appropriate permutation matrix according to Eq. (4.23). Here we use the particular pivoting strategy proposed by Cheng and Higham [109] for the modified Cholesky algorithm. They recommend using the bounded Bunch-Kaufman (rook) diagonal pivoting method [110] to find the indefinite factorization of $\mathbf{P}_i\mathbf{G}_i\mathbf{P}_i^T = \mathbf{L}_i\tilde{\mathbf{D}}_i\mathbf{L}_i$. After the decomposition has been found the symmetric indefinite block diagonal matrix $\tilde{\mathbf{D}}_i$ is perturbed in the Frobenius norm $\Delta\tilde{\mathbf{D}}_i$ such that $\lambda_{\min}\left(\tilde{\mathbf{D}}_i + \Delta\tilde{\mathbf{D}}_i\right) \leq \delta$ using the Higham theorem [111]. In the deMon2k implementation we set $\delta = 1.0 \times 10^{-9}$ for this tolerance [112]. Using the modified Cholesky decomposition, we can transform equation Eq. (4.22) into

$$\mathbf{X}_i = -\mathbf{E}_i\mathbf{B}_i, \tag{4.25}$$

where $\mathbf{B}_i$ is the matrix solution of the following equation system,

$$(\mathbf{L}_i\mathbf{D}_i\mathbf{L}_i^T)\mathbf{B}_i = \mathbf{E}_i^T. \tag{4.26}$$

The advantage of employing Eq. (4.25) instead of Eq. (4.22) is that solving Eq. (4.26) avoids the computation of the inverse of $\mathbf{G}_i$. In practical implementation we take advantages of LAPACK [113] libraries for solving Eq. (4.26), as well as, for the computation of the modified Cholesky decomposition.

4.2 Validation

The validation calculations for the here discussed range-separated hybrid functionals with DF-DFT and ADFT were performed in a developer version of deMon2k using the Cartesian def2-TZVPP [114] basis set in combination with the automatically generated GEN-A2* auxiliary function sets [115]. The structures of the first 56 molecules from the original G2 [116, 117] test set were optimized at the DFT, DF-DFT, and ADFT levels of theory to validate the total energy and energy gradients. The n-alkane chains $C_{10}H_{22}$, $C_{20}H_{32}$, and $C_{30}H_{62}$ were used for the validation of domain cutoffs. Formation enthalpies of the 223 molecules of the G3 [118, 119] test set in their B3LYP/6-31G(2df,p) optimized geometries were used for further validation of energies. For four-center ERI DFT calculations, the NWChem [120] code was used. To facilitate the comparison to NWChem, we used the fixed coarse grid with the Mura-Knowles [121] radial quadrature in deMon2k. Furthermore, unscreened Becke atomic

weights [122] were used in the validation calculations. For all other keywords, the default deMon2k settings are used.

4.2.1   Total Energies and Energy Gradients

For the validation of the total energies and analytic energy gradients of range-separated hybrid functionals we use a modified G2 set, which contains 122 bond lengths, 64 bond angles and 34 dihedral angles. Fig. 4.1 shows the linear correlation plots of converged total energies between four-center ERI DFT and DF-DFT as well as four-center ERI DFT and ADFT for the modified G2 set using the CAMPBE0, HSE06 and LCPBE range-separated hybrid functionals. The energy differences found in the modified G2 set are less than 1.0×10^{-4} a.u. for all comparisons. Moreover, the values found for the correlation coefficient are around 0.9999 in all cases.

The mean absolute deviations (MADs) in bond lengths, angles and dihedral angles with respect to standard four-center ERI DFT optimized structures are reported in Table. 4.1 for the CAMPBE0, HSE06 and LCPBE functionals. Table 4.1 shows MADs of around 10^{-4} Å for bond lengths, 10^{-2} degrees for bond angles, and 10^{-1} degrees for dihedral angles for both, DF-DFT and ADFT, methodologies. We note that these deviations are within the accuracy of the used numerical integration and optimization thresholds. Although we compare here optimized DF-DFT and ADFT structure parameters only for 3 functionals explicitly with four-center ERI results we note that the other functionals discussed in this thesis show similar results for total energies and gradientes.

Table 4.1: MADs of the bond lengths, bond angles and dihedral angles of the DF-DFT and ADFT optimized CAMPBE0, HSE06 and LCPBE structures with respect to corresponding NWChem optimized structures for the modified G2 set.

		Bond [pm]	Angle [deg]	Dihedral [deg]
DF-DFT	CAMPBE0	1.2×10^{-4}	2.0×10^{-2}	1.5×10^{-1}
	HSE06	2.3×10^{-4}	3.5×10^{-2}	1.5×10^{-1}
	LCPBE	1.9×10^{-4}	5.6×10^{-2}	1.4×10^{-1}
ADFT	CAMPBE0	2.5×10^{-4}	2.3×10^{-2}	2.7×10^{-1}
	HSE06	2.0×10^{-4}	3.5×10^{-2}	2.5×10^{-1}
	LCPBE	4.2×10^{-4}	6.9×10^{-2}	1.4×10^{-1}

We finish our discussion on the accuracy of the variational fitted (long-range) Fock exchange
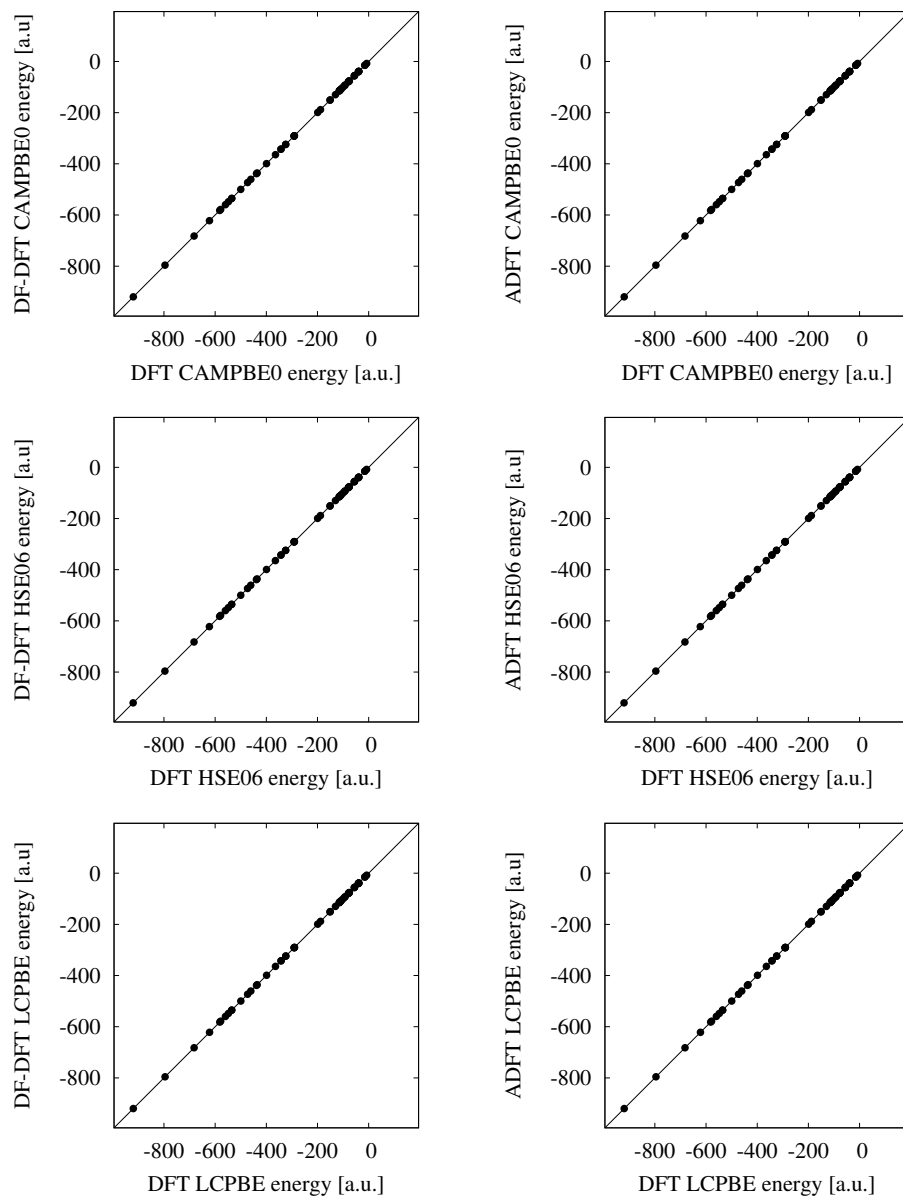
Figure 4.1: Linear correlation plots between the energies [a.u] calculated with four-center ERI density functional theory of the modified G2 test set molecules with density fitted DFT (DF-DFT) and auxiliary density functional theory (ADFT) for the CAMPBE0, HSE06 and LCPBE range-separated hybrid functionals.

with the asymptotic expansion of the involved three-center ERIs. Due to the underlying implementation structure only the first asymptotic ERI expansion [41] is used for the variational fitted Fock exchange. Nevertheless, the same asymptotic radii as for the double asymptotic Coulomb ERIs are used. Although this has no effect on the converged SCF energies, it became problematic for gradient calculations as detailed in Appendix B for the $C_{54}H_{20}$ graphene flake. A straightforward solution is to double the asymptotic radii of the atoms for the gradient calculation of the variational fitted (long-range) Fock exchange.

4.2.2 Domain Selection

In order to demonstrate that our domain cutoffs are also reliable for increasing system sizes we report in Table 4.2 energy differences of global and range-separated Fock exchange, DF-DFT and ADFT calculations with respect to corresponding four-center ERI calculations for the n-alkanes $C_{10}H_{22}$, $C_{20}H_{42}$ and $C_{30}H_{62}$. Table 4.2 shows that the energy differences are in the range of 10^{-3} a.u. or below, indicating that the here used cutoffs are also appropriate for larger systems. We note that due to slightly different physical constant definitions and standard SCF convergence thresholds total energy differences of 10^{-4} a.u. between deMon2k and NWChem are common for these system sizes. Furthermore, we also point out that the convergence limits of (four-center ERI) Kohn-Sham DFT and ADFT are slightly different which is included in a total energy comparison.

Table 4.2: Converged Fock, CAMPBE0, HSE06 and LCPBE total energy differences [a.u.] with respect to four-center ERI DFT total energies for $C_{10}H_{22}$, $C_{20}H_{42}$ and $C_{30}H_{62}$ alkane chains.

		$C_{10}H_{22}$	$C_{20}H_{42}$	$C_{30}H_{62}$
	Global	1.2×10^{-3}	2.6×10^{-3}	4.0×10^{-3}
Fock	Long-range	2.6×10^{-4}	5.0×10^{-4}	7.4×10^{-4}
	Short-range	7.3×10^{-4}	1.5×10^{-3}	2.7×10^{-3}
	CAMPBE0	7.7×10^{-5}	6.0×10^{-5}	1.2×10^{-4}
DF-DFT	HSE06	2.0×10^{-4}	3.1×10^{-4}	5.0×10^{-4}
	LCPBE	5.4×10^{-4}	1.0×10^{-3}	1.5×10^{-3}
	CAMPBE0	1.6×10^{-3}	2.9×10^{-3}	4.3×10^{-3}
ADFT	HSE06	1.8×10^{-3}	3.2×10^{-3}	4.5×10^{-3}
	LCPBE	2.5×10^{-3}	4.6×10^{-3}	6.8×10^{-3}

Further calculations were performed on the $C_{30}H_{62}$ alkane chain in order to evidence the

behavior of the domain and overlap cutoffs. In Fig. 4.2 the converged long-range Fock exchange energy differences [a.u.] of $C_{30}H_{62}$ with respect to a domain cutoff of 1.000 and an overlap cutoff of 1.0×10^{-8} a.u. are plotted.
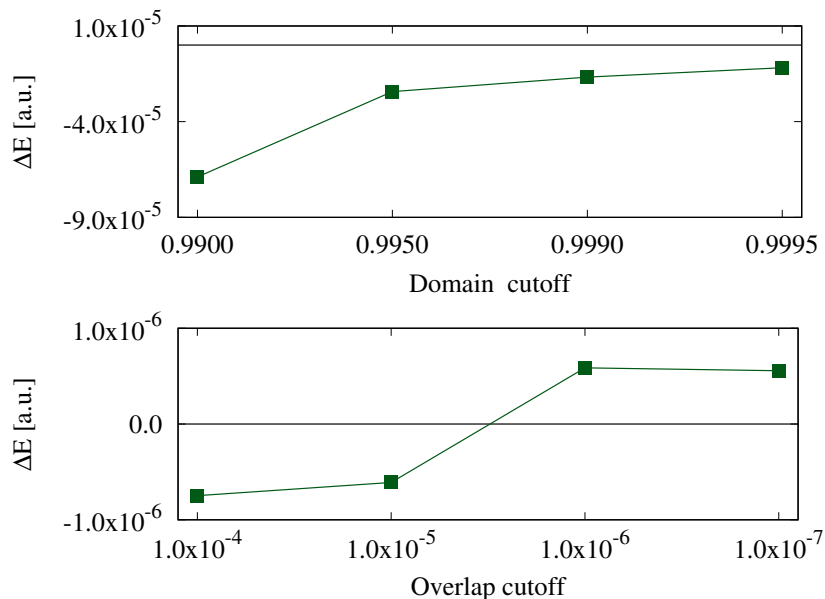
Figure 4.2: Converged long-range Fock exchange energy differences [a.u.] of the $C_{30}H_{62}$ alkane chain with respect to four-center ERI calculations.

In the top of Fig. 4.2 the converged long-range Fock exchange energy difference is plotted as a function of the atomic population sum used for the definition of atomic auxiliary function centers in the LMOs according to Eq. (2.31). The overlap cutoff was 1.0×10^{-8} in these calculations. The bottom of Fig. 4.2 shows the same energy difference now as a function of the overlap cutoff for the definition of the corresponding atomic basis set centers. The atomic population sum was 0.9990 in these calculations. As Fig. 4.2 shows smooth convergence of the energy difference is obtained for the domain cutoff. In case of the overlap cutoff the error turns from small negative to small positive values with decreasing thresholds. The different convergence behaviors in Fig. 4.2 underline once again the variational nature of the density fitting with respect to the auxiliary function expansion, here altered by the domain cutoff value. On the other hand, the overlap cutoff is similar to an integral screening and, therefore, does not possess a variational bound. Altogether, Fig 4.2 demonstrates that our domain and overlap cutoffs are size extensive and can be used for nanosystems. For the here plotted $C_{30}H_{62}$ the energy differences are in the range of 10^{-5} and 10^{-6} a.u. for the atomic

population sum threshold and the overlap cutoff, respectively. Thus, also the absolute values of the long-range Fock exchange energy differences are size extensive thanks to the variational character of the here proposed long-range Fock exchange fitting.

4.2.3 Thermochemical Properties

For further validation of the here discussed range-separated hybrid functional implementation we calculated standard heats of formation as proposed by Curtis et al. [116–119] for the 223 molecules of the G3/99 test set. Here the calculations were performed with the Cartesian def2-TZVPP basis set. For the variational density fitting in DF-DFT and ADFT the GEN-A2* auxiliary function set was employed. In order to calculate ΔH_f^{298K} for a general molecule with formula $A_x B_y C_z$, the following steps must be performed:

1. Calculate the zero-point corrected atomization energy D_0 as:

$$D_0(A_x b_y C_z) = [xE_e(A) + yE_e(B) + zE_e(C)] - E_e(A_x B_y C_z) + E_{ZPE}(A_x B_y C_z) \quad (4.27)$$

2. Calculate the enthalpy of formation at 0 K as:

$$\Delta H_f^{0K}(A_x B_y C_z) = \left[x\Delta H_f^{0K}(A) + y\Delta H_f^{0K}(B) + z\Delta H_f^{0K}(C)\right] - D_0(A_x B_y C_z) \quad (4.28)$$

3. Calculate ΔH^{298K}:

$$\begin{aligned}
\Delta H^{298K} &= \Delta H_f^{0K}(A_x B_y C_z) + H_{298K}(A_x B_y C_z) - H_{0K}(A_x B_y C_z) - \\
&\quad x\left[H_{298K}(A) - H_{0K}(A)\right] - y\left[H_{298K}(B) - H_{0K}(B)\right] - \quad (4.29) \\
&\quad z\left[H_{298K}(C) - H_{0K}(C)\right]
\end{aligned}$$

The $\Delta H_f^{0K}(X)$ and $[\Delta H_{298K}(X) - \Delta H_{0K}(X)]$ for a given atom X as well as the zero point energy corrections were taken from Ref. [116]. The MADs of the calculated standard heats of formations with respect to experiments are show in Table 4.3 for the CAMB3LYP, CAMPBE0, CAMQTP00, CAMQTP01, HSE03, HSE06, LCBLYP, LCPBE and rCAMB3LYP functionals. The second column of Table 4.3 corresponds to the MADs as obtained with standard four-center ERI DFT calculations. These MADs are compared with those obtained from DF-DFT (third column) and ADFT (fourth column) calculations employing the here proposed local density fitted range-separated Fock exchange energy. As Table 4.3 shows the

DF-DFT calculations differ for almost all functionals by less than 0.1 kcal/mol in the MADs
from the DFT reference that employs four-center ERIs. The only exception is CAMQTP01
where we found a MAD of 0.14 kcal/mol between DFT and DF-DFT. With ADFT this differ-
ence increases to about 0.2 kcal/mol. Note, however, that ADFT MADs can be significantly
smaller than their four-center counterparts. Most remarkable in this respect is CAMB3LYP
where the ADFT MAD is around 0.5 kcal/mol smaller than the corresponding DF-DFT and
four-center ERI DFT MADs. This underlines once again the different convergence bounds of
functionals in ADFT and Kohn-Sham DFT. In the particular case of CAMB3LYP, a detailed
analysis showed that this improvement is mainly due to LYP correlation, which produces
larger symmetry breaking in Kohn-Sham DFT than in ADFT. Most certainly this is rooted
in the use of the auxiliary density for the calculation of the LYP correlation in ADFT. Thus,
it is not surprising that also ADFT CAMQTP01, LCBLYP and rCAMB3LYP results im-
prove upon DF-DFT and DFT, albeit less pronounced than for CAMB3LYP. For the PBE
based range-separated hybrid calculations this effect is not seen because PBE correlation
shows almost no symmetry breaking in Kohn-Sham DFT as well as in ADFT.

Table 4.3: MADs [kcal/mol] for the studied range-separated hybrid functionals
of the 223 standard enthalpies of formation of the G3 test set molecules.

	DFT	DF-DFT	ADFT
CAMB3LYP	4.80	4.84	4.32
CAMPBE0	26.10	26.12	26.22
CAMQTP00	17.24	17.15	17.40
CAMQTP01	13.70	13.84	13.61
HSE03	4.90	4.90	5.04
HSE06	6.62	6.61	6.72
LCBLYP	32.53	32.57	32.33
LCPBE	48.90	48.93	48.96
rCAMB3LYP	5.91	5.94	5.85

4.2.4   Static and Dynamic Polarizabilities

In order to validate the newly developed ADPT working equations for global and range sep-
arated hybrid functionals, we compare static and dynamic polarizabilities and static hyper-
polarizabilities of small molecules with four-center ERI reference results. The experimental
geometries were used for this comparison [123]. All calculations were performed with the

aug-cc-pVTZ basis set. For the ADFT and ADPT calculations the GEN-A2* auxiliary function set was employed. The ADPT static polarizabilities were compared with corresponding ADFT finite field results as well as with their coupled cluster singles and doubles (CCSD) counterparts [124, 125]. The calculated dynamical polarizabilities at a frequency of 500 nm were compared with those obtained with the CPKS methodology implemented in the Gaussian 09 code [126]. Static first hyperpolarizabilies obtained by finite field method were also compared with CCSD results from the literature [124, 125].

In order to obtain suitable finite field expressions for static response properties calculation, we used the dipole moment Taylor series expansion [127]

$$\mu_i(\mathcal{E}) = \mu_i(0) + \sum_j \alpha_{ij}\mathcal{E}_j + \sum_{j,k} \beta_{ijk}\mathcal{E}_j\mathcal{E}_k + \frac{1}{6}\sum_{j,k,l} \gamma_{ijkl}\mathcal{E}_j\mathcal{E}_k\mathcal{E}_l + ... \tag{4.30}$$

where $\mathcal{E}_i$ denotes the magnitude of the ith Cartesian component of the electric field, $\mathcal{E}$, $\mu_i(0)$ is the permanent dipole moment of the molecular system in the absence of the external electric field and α_{ij}, β_{ijk} and γ_{ijkl}, are tensor elements of the polarizability, first hyperpolarizability and second hyperpolarizability, respectively. If the molecule is considered to be in a uniform electric field aligned along one of the axis of the system and the dipole moment is evaluated at various field strengths, the following equations can be derived [127, 128]

$$\alpha_{ii}\mathcal{E}_i = \frac{2}{3}[\mu_i(\mathcal{E}_i) - \mu_i(-\mathcal{E}_i)] - \frac{1}{12}[\mu_i(2\mathcal{E}_i) - \mu_i(-2\mathcal{E}_i)] \tag{4.31}$$

$$\alpha_{ij}\mathcal{E}_j = \frac{2}{3}[\mu_i(\mathcal{E}_j) - \mu_i(-\mathcal{E}_j)] - \frac{1}{12}[\mu_i(2\mathcal{E}_j) - \mu_i(-2\mathcal{E}_j)]. \tag{4.32}$$

$$\beta_{iii}\mathcal{E}_i^2 = \frac{1}{3}[\mu_i(2\mathcal{E}_i) - \mu_i(-2\mathcal{E}_j)] - \frac{1}{3}[\mu_i(\mathcal{E}_i) + \mu_i(-\mathcal{E}_i)] \tag{4.33}$$

$$\beta_{ijj}\mathcal{E}_j^2 = \frac{1}{3}[\mu_i(2\mathcal{E}_j) - \mu_i(-2\mathcal{E}_j)] - \frac{1}{3}[\mu_i(\mathcal{E}_j) + \mu_i(-\mathcal{E}_j)] \tag{4.34}$$

Thus, for the calculation of the α components, self-consistent field runs are necessary with field strengths $\pm\mathcal{E}_i$ and $\pm2\mathcal{E}_i$ ($i = x, y, z$). Note that dynamical polarizalibities can not be obtained from finite field calculations. On the other hand, in analytic derivative methods the perturbed density matrix can be obtained via ADPT by McWeeny's SCP theory, as we

discussed in Section 3.4. Employing basis and auxiliary function sets that are independent from the external electric field, we find for the polarizability tensor components [22]

$$\alpha_{ij}(\omega) = -\sum_{\mu,\nu} P_{\mu\nu}^{(i)}(\omega)\langle\mu|r_j\nu\rangle \tag{4.35}$$

Here the $\langle\mu|r_j\,\nu\rangle$ are dipole moment matrix elements and the perturbed density matrix $P_{\mu\nu}^{(i)}(\omega)$ is calculated using Eq. (3.61). From the calculated polarizability components, either by the finite field or analytical methodology, the average polarizability can be obtained as

$$\bar{\alpha} = \frac{1}{3}\left(\alpha_{xx} + \alpha_{yy} + \alpha_{zz}\right) \tag{4.36}$$

The finite field calculation of the $\boldsymbol{\beta}$ components permits the calculation of the average first hyperpolarizability along the direction of the permanent dipole moment, in our particular case the z axis using the EFISH [76] keyword in deMon2k

$$\bar{\beta} = \frac{3}{5}\sum_i \beta_{iiz} \tag{4.37}$$

Static ADPT polarizabilities of 14 small molecules were calculated using Hartree-Fock, the PBE0 global hybrid functional and CAMPBE0, LCPBE and HSE06 range-separated hybrid functionals. In Table 4.4 these results are compared with the corresponding CCSD results from Ref. [124, 125]. As this table shows the analytically calculated ADPT static polarizabilities are generally in excellent agreement with their finite field ADFT counterpart. Deviations are in the range of 0.1 a.u. or smaller that are characteristic for finite field approaches. Thus, we find internal consistency between analytically calculated ADPT static polarizabilities and corresponding ADFT finite field results. The comparison to CCSD results shows large deviations for Hartree-Fock with a MAD of 0.86 a.u. that is significantly reduced by all hybrid functionals except LCPBE. No significant differences between the here studied global and range separated hybrid functionals are found for static polarizabilites.

Table 4.5 compares three-center ERI ADPT with four-center ERI CPHF/CPKS dynamical polarizabilities at the Hartree-Fock, global hybrid (PBE0) and range-separated hybrid (CAMB3LYP and HSE06) level of theory. The external field frequency was set to $\omega = 500$ nm in all calculations.

Table 4.4: Static ADPT polarizabilies [a.u] calculated with Hartree-Fock and different hybrid functionals employing aug-cc-pVTZ/GEN-A2* basis and auxiliary function sets. The MADs are calculated with respect to the CCSD/aug-cc-pVTZ results from Karne et al. [124, 125]. Values in parentheses refer to ADFT finite field results.

| | Functional | | | | | |
	Fock	PBE0	CAMPBE0	LCPBE	HSE06	CCSD
CH_2NH	22.33 (22.34)	22.80 (22.78)	22.55 (22.56)	23.11 (23.12)	22.66 (22.70)	22.56
CH_2O	16.81 (16.81)	17.79 (17.79)	17.60 (17.60)	18.21 (18.21)	17.70 (17.73)	17.73
CH_3F	15.80 (15.80)	16.90 (16.91)	16.78 (16.78)	17.43 (17.43)	16.82 (16.86)	16.18
CH_3NH_2	24.34 (24.35)	25.97 (25.90)	25.57 (25.56)	26.44 (26.43)	25.80 (25.88)	25.73
CH_3OH	19.93 (19.93)	21.36 (21.37)	21.10 (21.10)	21.89 (21.88)	21.25 (21.31)	21.20
CNH	17.54 (17.54)	18.35 (18.36)	18.14 (18.14)	18.69 (18.68)	18.29 (18.32)	18.44
CO	12.41 (12.41)	13.16 (13.16)	13.07 (13.06)	13.50 (13.51)	13.14 (13.15)	13.21
H_2O	8.56 (8.56)	9.70 (9.67)	9.52 (9.52)	10.07 (10.07)	9.59 (9.63)	9.62
H_2S	23.85 (23.85)	24.77 (24.78)	24.34 (24.33)	24.90 (24.89)	24.71 (24.74)	24.60
HCl	16.45 (16.45)	17.21 (17.21)	16.97 (16.97)	17.43 (17.42)	17.18 (17.19)	17.13
HCN	16.82 (16.82)	17.10 (17.11)	16.92 (16.92)	17.28 (17.28)	17.05 (17.10)	16.70
HCP	36.73 (36.74)	36.12 (36.13)	35.63 (35.63)	35.90 (35.90)	36.07 (36.09)	35.54
HF	4.83 (4.83)	5.51 (5.52)	5.47 (5.47)	5.84 (5.83)	5.49 (5.51)	5.47
NH_3	13.02 (13.02)	14.27 (14.29)	13.96 (13.97)	14.64 (14.63)	14.17 (14.26)	14.16
MAD	**0.82 (0.82)**	**0.22 (0.21)**	**0.18 (0.18)**	**0.50 (0.50)**	**0.16 (0.18)**	

Table 4.5: Comparison of dynamic ADPT and CPHF/CPKS polarizabilies [a.u] calculated with Hartree-Fock and different hybrid functionals employing aug-cc-pVTZ/GEN-A2* basis and auxiliary function sets. The MADs refer to the diference between ADPT and CPHF/CPKS. All calculations were performed at $\omega = 500$ nm.

| | Functional | | | | | | | |
| | Fock | | PBE0 | | CAMB3LYP | | HSE06 | |
	ADPT	CPHF	ADPT	CPKS	ADPT	CPKS	ADPT	CPKS
CH_2NH	23.23	23.22	23.70	23.91	23.97	23.99	23.73	23.94
CH_2O	17.31	17.32	18.42	18.56	18.53	18.56	18.41	18.58
CH_3F	16.14	16.15	17.35	17.49	17.54	17.51	17.32	17.50
CH_3NH_2	25.05	25.05	26.84	27.12	27.03	27.02	26.91	27.15
CH_3OH	20.42	20.43	21.97	22.17	22.18	22.15	21.99	22.20
CNH	18.15	18.15	19.11	19.12	19.19	19.20	19.09	19.13
CO	12.77	12.77	13.58	13.58	13.73	13.69	13.60	13.59
H_2O	8.76	8.76	9.92	9.99	10.12	10.07	10.02	10.00
H_2S	24.89	24.89	25.97	25.94	26.02	26.00	25.98	25.99
HCl	16.92	16.93	17.77	17.75	17.89	17.85	17.78	17.78
HCN	17.32	17.32	17.63	17.65	17.84	17.78	17.64	17.66
HCP	39.11	39.12	38.41	38.42	38.61	38.64	38.43	38.49
HF	4.90	4.90	5.62	5.63	5.76	5.71	5.62	5.64
NH_3	13.44	13.45	14.87	14.98	15.06	15.00	14.91	15.00
MAD	**0.00**		**0.09**		**0.04**		**0.09**	

As Table 4.5 shows the ADPT Hartree-Fock and CPHF dynamic polarizabilities match perfectly. This validates our newly developed ADPT working equations. The small differences found for the hybrid functional dynamical polarizabilities can be traced back to the different numerical integration algorithms used in the deMon2k and Gaussian09 codes.

Static ADPT first hyperpolarizabilities of small molecules were calculated using Hartree-Fock, the PBE GGA functional, PBE0 global hybrid functional and CAMPBE0, LCPBE and HSE06 range-separated hybrid functionals. They are compared with the corresponding CCSD results [124, 125] in Table 4.6. As this table shows, the comparison between CCSD results with Hartree Fock and PBE ADFT finite field static hyperpolarizabilities presents large MADs of 10.35 and 10.83 a.u., respectively. With hybrid functionals these MADs are reduced to less than half, with the exception of LCPBE which presents a MAD of 6.05 a.u. Note the similarity to the static polarizability LCPBE results. As Table 4.6 shows the HSE06 functional yields the smallest MAD for first hyperpolarizabilities. Altogether, hybrid functionals improve polarizabilities and first hyperpolarizabilities with respect to CCSD reference data. Here, we have demonstrated that our new developed ADPT working equations can correctly compute electric response properties within the selected basis set quality, regardless of the functional type, and can be used instead of expensive iterative CPKS or CPHF methods. Our first results indicate that ADPT hybrid functional calculations of polarizabilities and hyperpolarizabilities compare favorable with CCSD correlated wave function results. Most certainly more systematic studies are needed for pinpointing appropriate functionals.

Table 4.6: Finite field static first hyperpolarizabilities calculated with Hartree-Fock, PBE and different hybrid functionals employing aug-cc-pVTZ/GEN-A2* basis and auxiliary function sets. The MADs are calculated with respect to the CCSD/aug-cc-pVTZ results from Karne et al. [124, 125]

				Functional			
	Fock	PBE	PBE0	LCPBE	CAMPBE0	HSE06	CCSD
CH$_2$NH	-18.39	-23.09	-13.43	-13.94	-15.67	-16.27	-11.54
CH$_2$O	-51.23	-95.71	-70.57	-68.71	-60.22	-69.02	-57.17
CH$_3$F	-39.48	-63.09	-51.75	-56.10	-49.90	-49.91	-44.35
CH$_3$NH$_2$	-7.60	-40.46	-20.62	-8.19	-9.41	-20.39	-12.43
CH$_3$OH	-28.01	-54.01	-40.88	-39.17	-35.28	-39.84	-31.91
CNH	32.82	22.60	29.79	38.39	34.68	29.51	22.01
CO	-26.45	32.32	28.87	30.54	28.45	28.72	26.30
H$_2$O	-12.50	-20.34	-16.83	-17.07	-14.28	-17.50	-19.07
H$_2$S	-3.49	-16.17	-11.22	-7.34	-5.85	-11.55	-11.32
HCl	-7.71	-16.08	-11.84	-10.61	-9.08	-12.04	-11.55
HCN	-9.77	-9.66	-7.88	-1.82	-5.41	-7.85	-3.98
HCP	46.72	35.50	37.11	39.75	39.89	36.60	32.17
HF	-7.68	-11.64	-10.03	-9.39	-8.41	-10.34	-10.36
NH$_3$	-15.44	-34.32	-25.35	-19.93	-17.13	-25.38	-29.17
MAD	**10.35**	**10.83**	**4.70**	**6.05**	**4.99**	**4.45**	

4.3   Benchmarks

The computational performance of the here discussed range-separated hybrid functional implementations in deMon2k was benchmarked on linear alkane chains (C_nH_{2n+2}, $n \leq 150$), amylose fragments (α-D-glucose)$_n$ with n = 1,2,4,8,16 and graphene sheets with stoichiometric $C_{26}H_{16}$, $C_{40}H_{18}$, $C_{54}H_{20}$, $C_{68}H_{22}$ and $C_{82}H_{24}$. Structure examples of these systems are depicted in Fig. 4.3. We use the LCPBE functional with the cc-pVTZ [129] basis set in combination with the GEN-A2* auxiliary function set for our benchmark calculations. The calculations were performed in serial and parallel using Dual Intel Xeon E5-2650@2.20 GHz 12-core processor with around 4 GB RAM per core.
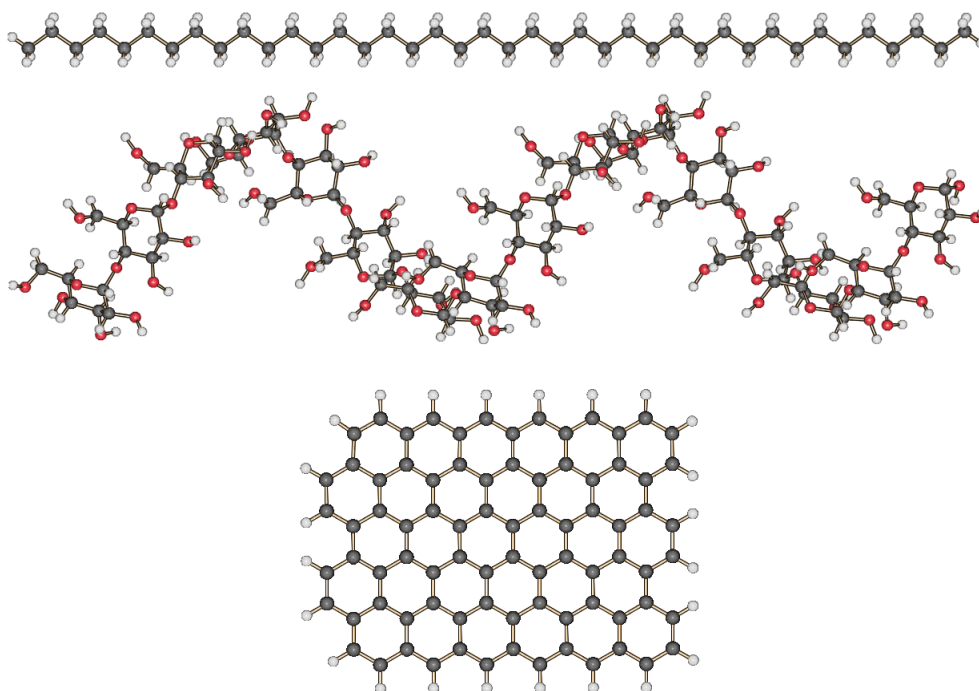
Figure 4.3: Illustrative structure examples of benchmark systems. From top to bottom: Linear $C_{40}H_{82}$ alkane chain, (α-D -glucose)$_{16}$ amylose fragment and hydrogen terminated $C_{82}H_{24}$ graphene lattice

Single point energy calculations of small alkane chains (C_nH_{2n+2}, $n \leq 20$) were also performed in order to compare the SCF step time from our implementation with that from four-center ERI DFT calculations, here NWChem [120]. In Fig. 4.4 the time per SCF cycle, in hours, for serial four-center ERI DFT (green squares) and three-center ERI ADFT energy (blue dots) calculations are shown. Note the difference of factor 100 between the DFT and ADFT

time scales. Thus, points of equal height in Fig. 4.4 indicate a speedup factor of 100. The actual speedup factors are 87, 88, 83, 89 and 87 for C_4H_{10} (290), C_8H_{18} (550), $C_{12}H_{26}$ (810), $C_{16}H_{34}$ (1070) and $C_{20}H_{42}$ (1330), respectively. The numbers in parentheses refer to the number of basis functions in these systems. This enormous improvement in computational performance allows the use of the hybrid ADFT methodology implemented in deMon2k to calculate nanometric systems. We will present some examples in this thesis and will refer to recent corresponding works of others. It is important to emphasize that comparative calculations with larger systems could not be performed because serial calculations with NWChem require a enormous amount of RAM. Thus, in the following discussion we will only analyze timings obtained with our implementation in deMon2k.
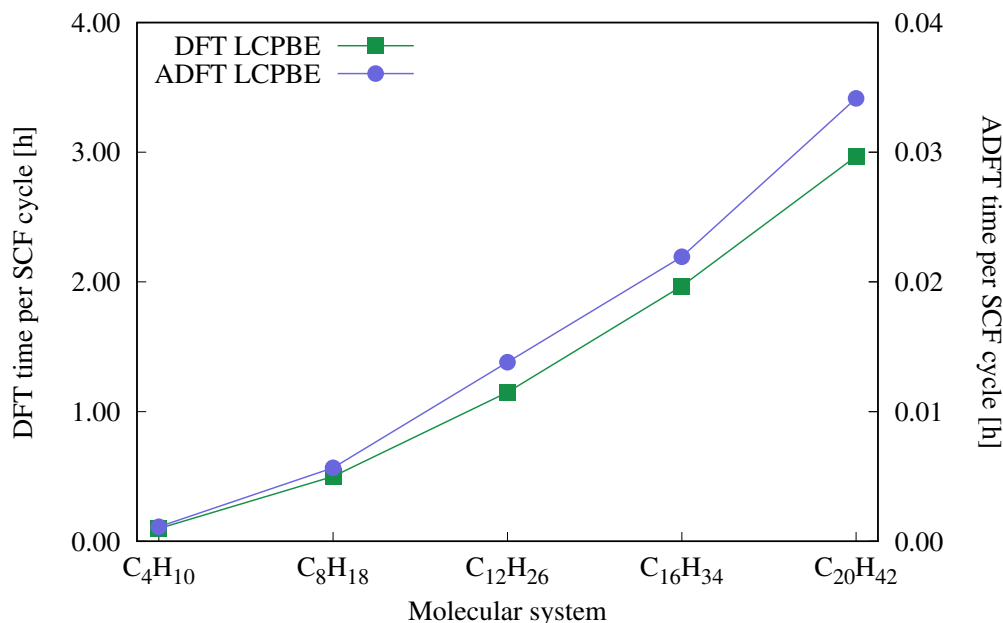
Figure 4.4: Serial CPU timings [h] for one LCPBE SCF step with four-center ERI DFT and three-center ERI ADFT of small linear alkane chains. To guide the eye the data points are connected by lines.

Figure 4.5 depicts serial SCF timings, in hours, versus the number of basis functions for the studied alkane chains, amylose fragments and saturated graphene sheets. The displayed SCF cycle times in Fig. 4.5 are averages obtained from converged single point energy calculations. In these calculations the local Coulomb matrices are inverted by Cholesky decomposition, or if this fails, truncated eigenvalue decomposition (Cholesky/TED). Since our LDF LR Fock exchange energy implementation strongly depends on the localization of MOs, systems with
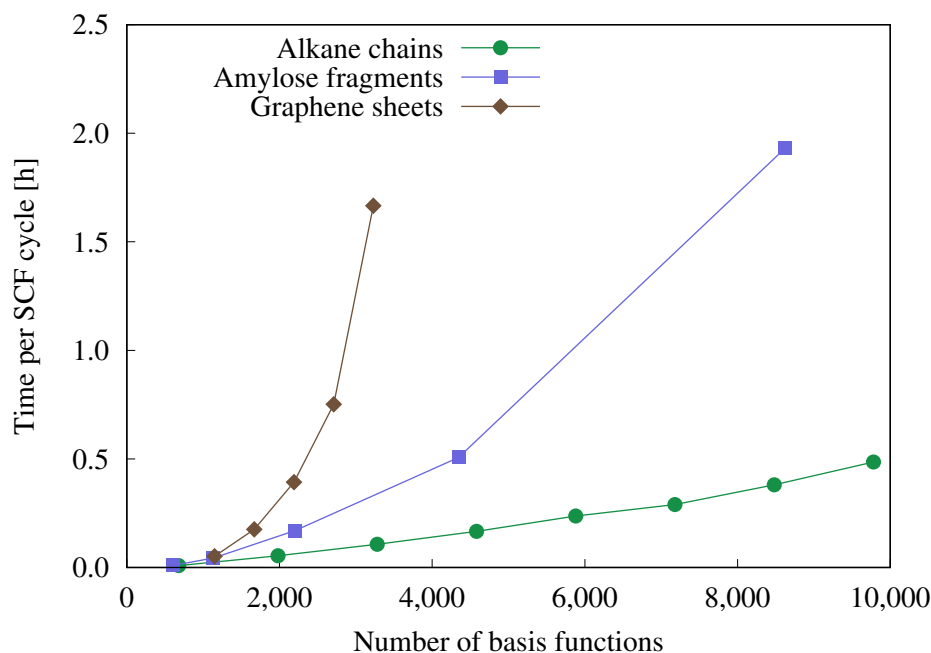
Figure 4.5: Serial CPU timings [h] for one SCF step of linear alkane chains, amylose fragments and saturated graphene sheets. To guide the eye the data points are connected by lines.

tightly localized MOs, such as the alkane chains, show better computational performance than less localized molecular systems, such as the graphene sheets. This is also reflected in the average scalings which are 1.5, 2.0 and 3.3 for the alkane chains, amylose fragments and graphene sheets, respectively. Besides the MO localization problem the larger graphene sheet timings also suffer from ERI batching due to the limited available memory (4 GB). Nevertheless, for the largest benchmarked systems, i.e. the $C_{150}H_{302}$ alkane chain, the (α-D-glucose)$_{16}$ amylose fragment and the $C_{82}H_{24}$ graphene sheet, the time for a serial SCF cycle is less than 0.5 hours, less than 2.0 hours and less than 1.7 hours, respectively.

In order to study the computational performance of our parallel implementation for the calculation of LR Fock exchange we performed the above discussed benchmark calculations also with 24 cores. Fig. 4.6 shows the corresponding averaged serial and parallel timings for one SCF cycle, excluding the time for the Fock potential calculation (green) and for the excluded Fock potential calculation (blue) alone. Note the difference of a factor of 10 between the serial and parallel time scales. Thus, bars of equal height in the serial and parallel plot indicate a speedup factor of 10. As Figure 4.6 shows significant speedups are obtained for all

systems by parallel execution. In particular, the calculations of the Fock potential (blue) with 24 cores show parallel speedup factors between 12 and 20 for the alkane (top row), between 9 and 12 for graphene sheets (bottom row) and between 17 and 20 for the amylose systems (middle row). The corresponding speedup factors are listed in Table C.1 of Appendix C. The reason for the different behavior in the here compared systems is rooted in the extension of the localized MOs. In the studied alkane systems the localized MO extensions are already converged and relatively small compared with the ones of the other two system types. This leads to a fast calculation of the Fock potential. Note, however, that in the calculation times for the Fock potential a serial part for the administration of data is included. The relative contribution of this part to the calculation time grows with increasing system size and reduces the overall parallel performance as the corresponding speedup factors in Figure 4.6 show.

Figure 4.6: Serial and parallel timings per SCF cycle [h] for the SCF iteration (green) and the Fock potential (blue) calculation alone using Cholesky/TED: top row, alkane chains; middle row, amylose fragments; bottom row, graphene sheets.

On the other hand, the localized MO extensions still grow with increasing system size in the graphene sheets. As a result, the proportion of the linear algebra tasks (TED of the Coulomb matrix) increases with system size which in turn reduces the parallel efficiency.

For the amylose systems neither the administrative part nor the linear algebra tasks become dominant and, therefore, a good parallel speedup for the Fock potential calculation is found for all system sizes. As Figure 4.6 shows the speedup factors for the SCF iterations are roughly equal or smaller than for the Fock potential. If the two speedup factors are roughly equal the Fock potential calculation is the computationally most demanding task in each SCF iteration. This is the case for all studied graphene sheets and amylose fragments, except the largest amylose fragment. This indicates that from this system size on other tasks than the Fock potential calculation dominate the SCF iteration time.
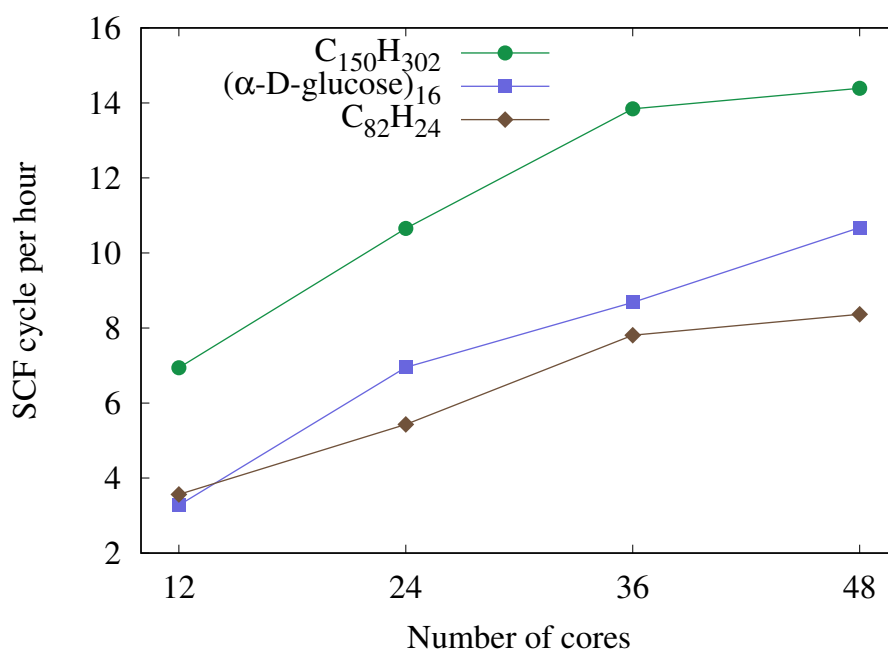
Figure 4.7: Number of SCF cycles per hour versus number of cores for the $C_{150}H_{302}$ alkane chain, $(\alpha\text{-D-glucose})_{16}$ amylose fragment and $C_{82}H_{24}$ saturated graphene sheet. The Cholesky/TED based algorithm was used to compute the Fock potential. To guide the eye the data points are connected by lines.

We also studied the scalability of our parallel implementation with respect to the number of cores in a calculation. To this end, we performed parallel calculations of our largest benchmark systems, namely the $C_{150}H_{302}$ alkane, the $(\alpha\text{-D-glucose})_{16}$ amylose fragment and the $C_{82}H_{24}$ graphene sheet with 12, 24, 36 and 48 cores. The number of SCF cycles per hour versus the number of cores are depicted in Fig. 4.7. For all systems we find a reduction of the CPU time with increasing numbers of cores. However, the efficiency of the parallelization reduces with increasing core numbers, i.e. the slope of the graph reduces. This effect is most

pronounced for the alkane and graphene systems and less for the amylose systems. It directly reflects the behavior of the scaling factors described above. By and large the same results are also obtained for the parallelization of global hybrid functionals and the corresponding parallelization of global and range-separated hybrid functional gradients.

In order to test the performance of the modified Cholesky decomposition, parallel calculations with 24 cores were carried out on the above discussed benchmark systems. Fig. 4.8 shows the corresponding averaged serial and parallel timings similar to Fig. 4.6. These timings along with the corresponding speedup factors are listed in Table C.2 of the Appendix C. Comparison of Fig 4.8 with Fig. 4.6 shows that the switch from Cholesky/TED to modified Cholesky decomposition has only little effect on the timings for the alkane chains and amylose fragments. Because in these systems the LMOs are rather localized most $\mathbf{G}_i$ inversions are successfully calculated with Cholesky decomposition. Thus, we can conclude from this comparison that the modified Cholesky decomposition has similar computational cost as its parent algorithm. The mild performance improvement ($\sim 5\%$) of the modified Cholesky decomposition based algorithm in serial and parallel Fock potential calculations as seen from the comparison of the corresponding entries in Tables C.1 and C.2 is most likely due to the sporadic TEDs in these systems. On the other hand, for the graphene sheets the use of the modified Cholesky decomposition yields large computational savings as the comparison of the corresponding plots in Fig. 4.8 and Fig. 4.6 shows. The quantitative comparison of the serial and parallel Fock potential timings for the graphene sheets in Table C.1 and C.2 reveals that the modified Cholesky decomposition speedups the serial calculations by 20 to 30%, whereas for parallel calculations speedup factors of up to 3 are reached. We attribute this to the fact that some LMOs in the graphene sheets are rather delocalized, due to the extended π-system in these molecules, and, therefore, TEDs are more likely to occur. Because this affects a certain part of the LMOs percentage speedup, as observed in the serial Fock potential calculations with the modified Cholesky decomposition, are expected. However, the large parallel speedups cannot be alone explained by the substitution of TEDs by modified Cholesky decomposition.

To gain more insight into this behavior, we plot in Fig. 4.9 once again the number of SCF cycles per hour versus the number of cores, now, however, for the modified Cholesky
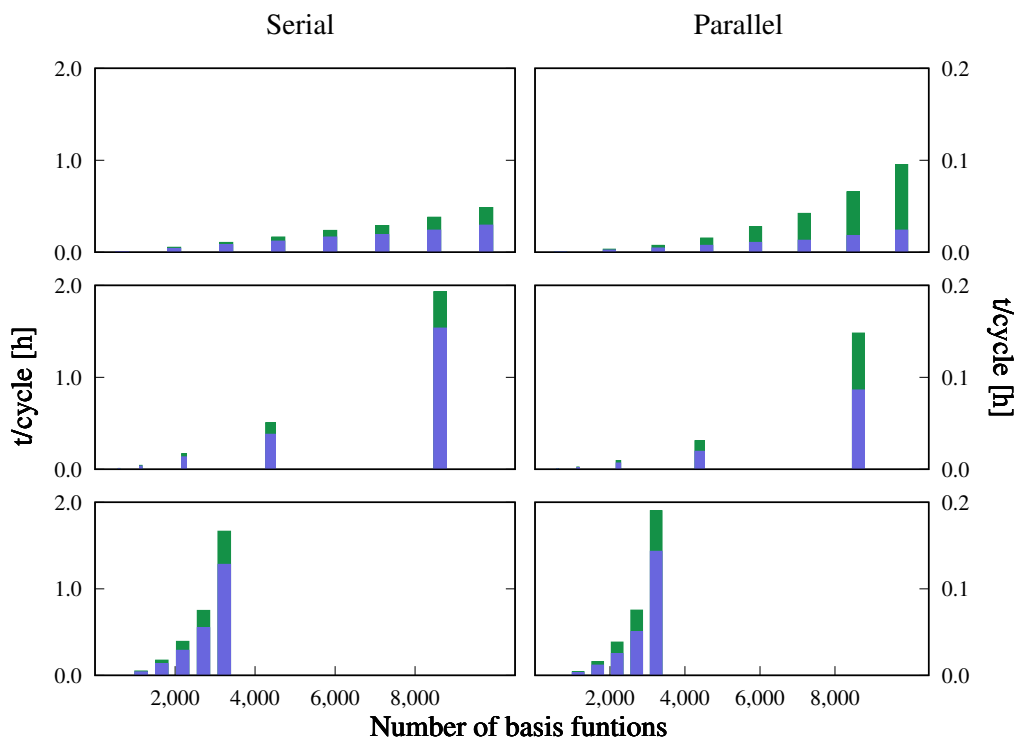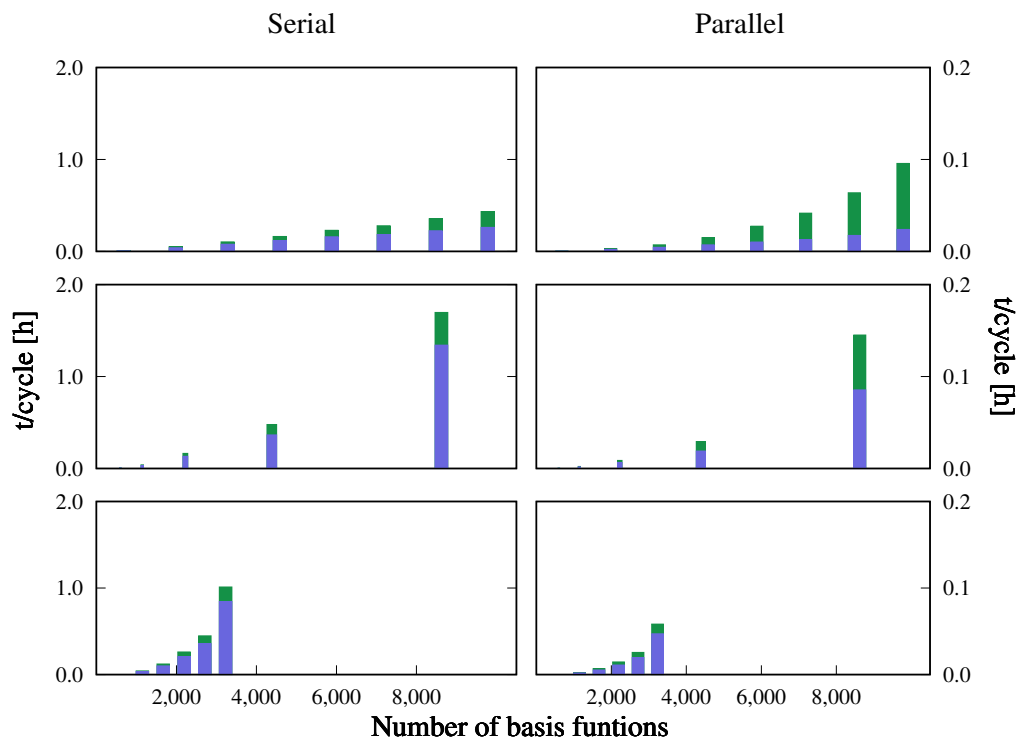
Figure 4.8: Serial and parallel timings per SCF cycle [h] for the SCF iteration (green) and the Fock potential (blue) calculation alone using modified Cholesky decomposition: top row, alkane chains; middle row, amylose fragments; bottom row, graphene sheets.

decomposition based algorithm. Comparison of Fig. 4.9 with 4.7 immediately shows that for all systems, starting form 12 cores, performance is improved when employing the modified Cholesky decomposition. Whereas this improvements is for alkane and amylose systems rather moderated and levels out with increasing number of cores, it is for graphene sheets dramatic and remains to increases with increasing number of cores. This result indicates that the increased use of TEDs in graphene sheet Fock potential calculations introduces a severe workload unbalance that compromises the overall parallel performance. With the implementation of the modified Cholesky decomposition TEDs are avoided, resulting in a more balanced workload between processors which in turn improves the overall parallelization and scaling. This opens up the possibility for hybrid functional calculations on molecules with large delocalized π-systems at the nanometric scale.
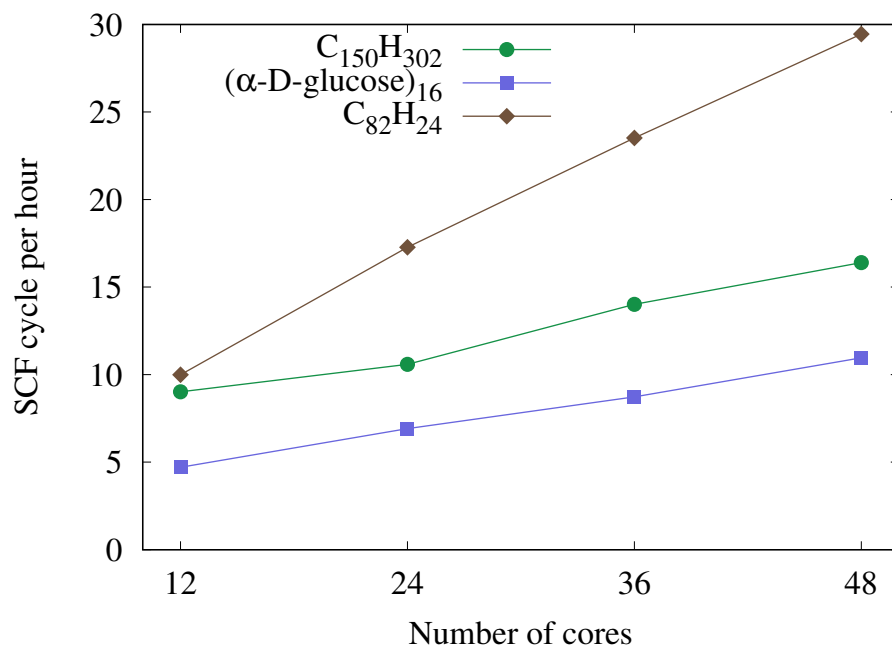
Figure 4.9: Number of SCF cycles per hour versus number of cores for the $C_{150}H_{302}$ alkane chain, $(\alpha\text{-D-glucose})_{16}$ amylose fragment and $C_{82}H_{24}$ saturated graphene sheet. The modified Cholesky decomposition base algorithm was used to compute the Fock potential. To guide the eye the data points are connected by lines.

Chapter 5

Applications

5.1 Activation and Reaction Enthapies

In this section, the performance of range-separated hybrid functionals for the computation of activation and reaction energies, for both small and large molecular systems, is presented.

5.1.1 Hydrocarbon Pericyclic Reactions

To this end, we have studied a set of hydrocarbon pericyclic reactions that were originally proposed by Houk and co-workers for benchmarking the performance of computational methods [44]. Fig. 5.1 depicts schematically the reactions considered in this study. As was pointed out in [44] hydrocarbon pericyclic reactions are particularly well suited for the validation of computed classical activation barriers. In order to compare directly with four-center ERI reference data from the literature all reactant and product structures were fully optimized without symmetry constraints with the B3LYP/6-31G*/GEN-A2* ADFT methodology. For the transition state search a hierarchically two step procedure [130] was used. First, double ended saddle interpolations starting with the optimized reactant and product structures were employed in order to find appropriate start structures for the local transition state optimizations. In a second step the transition states were optimized by an uphill trust region method [131, 132]. For the local quasi-Newton transition state optimizations the start Hessian matrices were calculated. Once the transition state structures were optimized, they were characterized by frequency analyses. To ensure that the obtained transition states indeed connect the reactants and products initially used in the double ended saddle interpolation the intrinsic reaction coordinates (IRCs) were also calculated [133].

83
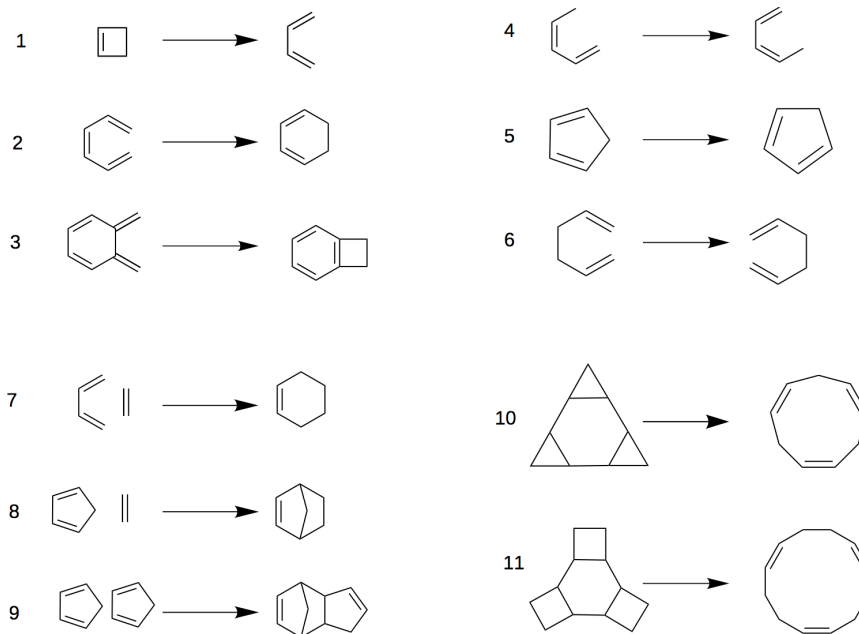
Figure 5.1: Reaction schemes of the pericyclic reactions used for ADFT benchmarking.

Houk et al. [44] studied the first nine reactions from Figure 5.1 at the B3LYP/6-31G* level of theory with a conventional DFT approach and compared the obtained activation energies, $\Delta H_{0K}^{\ddagger}$, and reaction enthalpies, ΔH_{0K}^{rxn}, with carefully selected experimental data adjusted to 0 K. Table 5.1 compares our ADFT results with those from Houk et. al. [44] and the corresponding experimental data. For the zero point energy correction we scaled the B3LYP/6-31G*/GEN-A2* zero point energies by a factor of 0.9804 according to the literature [44]. As Table 5.1 shows the ADFT and conventional four-center ERI DFT activation energies differ usually by 0.1 to 0.2 kcal/mol. The largest deviation of 0.4 kcal/mol is found for reaction 5, the [1,5]-sigmatropic shift of hydrogen in cyclopentadiene. For the corresponding reaction enthalpies slightly larger differences are observed. They are, however, all below or equal to 0.5 kcal/mol. The mean absolute deviation (MAD) from experiment for the activation energies, $\Delta H_{0K}^{\ddagger}$, was reported to 1.7 kcal/mol for the conventional four-center ERI Kohn-Sham approach. The corresponding ADFT MAD is 1.8 kcal/mol. For the six reactions with non-zero reaction enthalpies the MADs from experiment of the conventional Kohn-Sham approach and of ADFT are 4.1 and 3.9 kcal/mol, respectively. Taking into account that these results were obtained from two different programs using default settings the agreement between ADFT and conventional four-center ERI Kohn-Sham activation energies

and reaction enthalpies for the studied pericyclic reactions can be considered quantitative.

Table 5.1: Comparison of ADFT B3LYP/6-31G*/GEN-A2* and correspond-
ing Kohn-Sham DFT B3LYP/6-31G* results from the literature with experi-
mental data [44]. All values are in kcal/mol.

	ADFT		DFT		Experiment	
Reaction	$\Delta H_{0K}^{\ddagger}$	$\Delta H_{0K}^{\mathrm{rxn}}$	$\Delta H_{0K}^{\ddagger}$	$\Delta H_{0K}^{\mathrm{rxn}}$	$\Delta H_{0K}^{\ddagger}$	$\Delta H_{0K}^{\mathrm{rxn}}$
1	34.1	-12.5	33.9	-12.7	31.9	-10.6
2	30.0	-12.9	30.1	-12.5	30.2	-15.3
3	27.1	-14.6	27.3	-14.1	29.1	-10.5
4	36.7	0.0	36.6	0.0	36.7	0.0
5	27.0	0.0	26.6	0.0	23.7	0.0
6	34.0	0.0	34.1	0.0	34.5	0.0
7	24.8	-36.9	24.9	-36.6	23.3	-39.6
8	22.3	-19.0	22.2	-18.6	21.6	-23.2
9	21.1	-11.5	21.1	-11.1	15.1	-19.7

The ADFT B3LYP/6-31G*/GEN-A2* reaction profiles of the here discussed pericyclic reactions are depicted in Fig. 5.2. Note that for the calculations of these reaction profiles the reactants in the bimolecular reactions **7**, **8** and **9** are optimized together to form a pre-reaction complex. The calculated IRCs confirm that only reaction **1** and **7** show intermediates according to cis-trans isomerizations. These intermediates are directly accessible by the employed hierarchically two step transition state search approach. For the calculation of the activation and reaction enthalpies the following comments must be taken into account. In reaction **1** butadiene is calculated in trans configuration for the product energy. The reactant in reaction **2** is calculated as cis-hexa-1,3,5-trien. The reactants and products of reaction **4** and **6** are cis-1,3-pentadiene and 1,5-hexadiene, respectively. The reactants for the cycloaddition reactions **7**, **8** and **9** are separately calculated for the corresponding energies. In reaction **7** butadiene is calculated in trans configuration. For reaction **9** the endo reaction path is considered. Even though our focus is on ADFT B3LYP results which we can compare directly with their four-center ERI counterparts from the literature, we also employed various global and range-separated hybrid functionals in combination with several basis sets in our ADFT study. As exchange-correlation functionals we used B3LYP and PBE0 as examples for global hybrid functionals and CAMB3LYP, LCBLYP and HSE06 as examples for range-separated hybrid functionals.
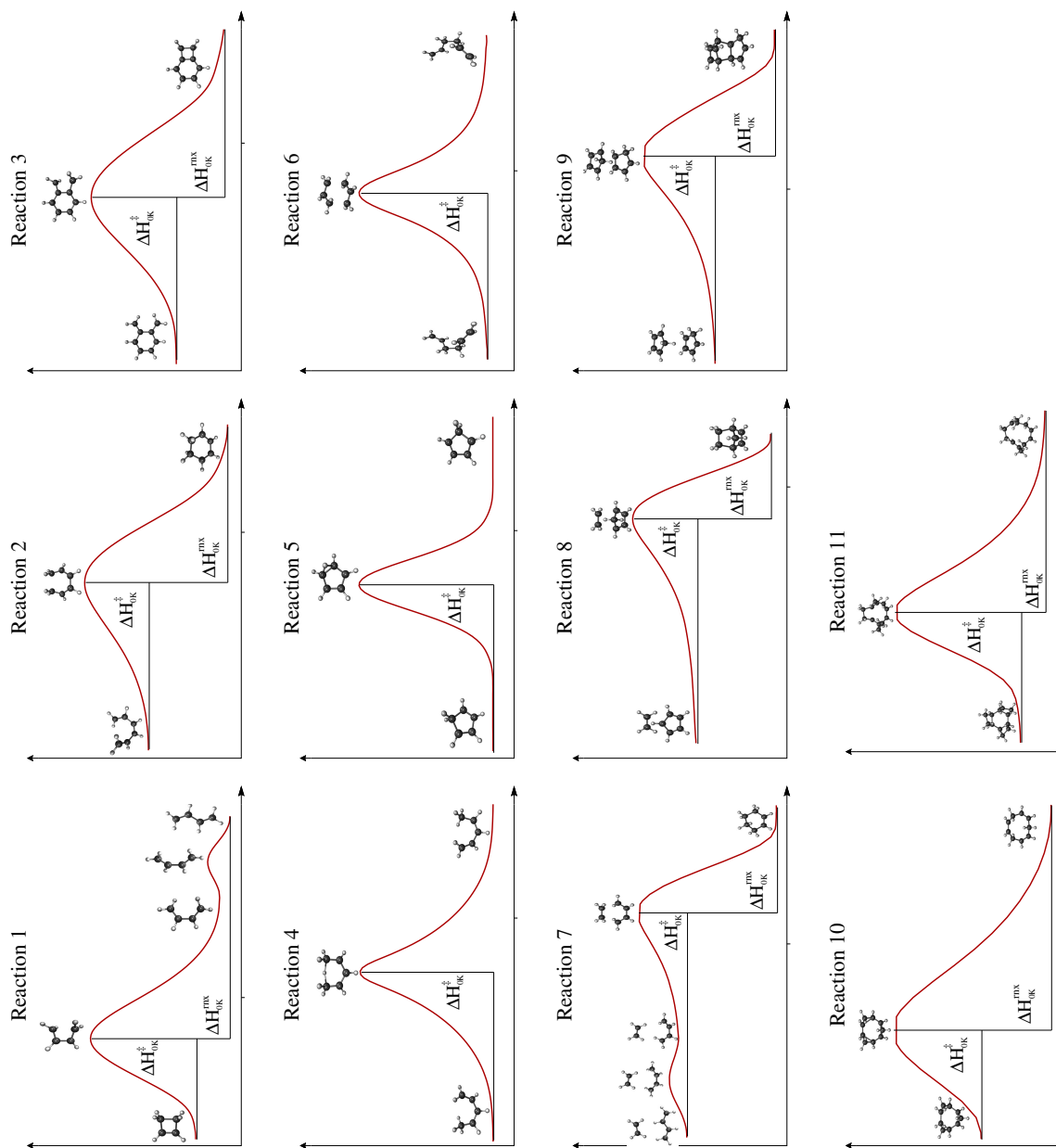
Figure 5.2: ADFT B3LYP/6-31G*/GEN-A2* reaction profiles for the studied pericyclic reactions.

For that purpose, we performed single-point energy calculations employing the B3LYP/6-31G*/GEN-A2* optimized reactant, transition state and product structures. On the other hand, it is well know that GGA optimized structure parameters are usually in good agreement with experimental data. Therefore, we also performed single-point energy calculations employing PBE/DZVP-GGA/GEN-A2* optimized structures. For the zero point energy corrections the unscaled PBE/DZVP-GGA/GEN-A2* zero point energies were taken. The Hartree-Fock optimized 6-31G* [134], the DFT optimized DZVP-GGA [115] and the correlation consistent aug-cc-pVXZ (X = D, T and Q) [135] basis sets were used in combination with the corresponding GEN-A2* auxiliary function sets.

Table 5.2 reports the MADs of the ADFT calculated activation energies and reaction enthalpies with respect to the recommended experimental reference values employing the B3LYP, PBE0, CAMB3LYP, HSE06 and LCBLYP functionals in combination with the 6-31G*, DZVP-GGA and aug-cc-pVXZ (X=D,T,Q) basis sets. As can be seen from Table 5.2 B3LYP/6-31G*/GEN-A2* yields one of the smallest MADs for activation energies. We note that the here obtained 2.2 kcal/mol MAD with ADFT is in perfect agreement with the corresponding Kohn-Sham MAD found by Houk and co-workers [44]. The good performance of B3LYP/6-31G*/GEN-A2* is at least partially due to the used optimized structures from the same level of theory. From the other functionals only PBE0 and HSE06 reach comparable accuracies for the activation energy MADs. In particular PBE0 activation energy MADs of the here studied pericyclic reactions show a very systematic improvement with basis set size. Convergence is nearly reached with the aug-cc-pVTZ basis with a MAD of 2.8 kcal/mol. Further increase of the basis set to aug-cc-pVQZ improves the MAD only marginally to 2.7 kcal/mol. With the HSE06 functional this MAD is already reached with the DFT optimized DZVP-GGA basis set. On the other hand, the range-separated CAMB3LYP and LCBLYP functionals perform rather poor for the activation energies of the here studied reactions.

Surprisingly Table 5.2 shows that B3LYP/6-31G*/GEN-A2* performs not best for the reaction enthalpies despite the fact that the structures were optimized at this level of theory. Even more disturbing is the fact that the ADFT B3LYP reaction enthalpies deteriorate significantly with increasing basis set size. We note that this observation is in qualitative agreement with results from Houk and co-workers employing conventional Kohn-Sham methodology. A sim-

ilar trend is also seen for the activation energies, albeit much less pronounced. On the other hand, PBE0 and HSE06 show systematic improvements in the reaction energy MADs with increasing basis set size. As for the activation energies near basis set convergence is reached for PBE0 and HSE06 with the aug-cc-pVTZ basis with MADs of 2.5 and 2.4 kcal/mol, respectively. In view of the rather disappointing performance of the range-separated CAMB3LYP hybrid functional for activation energies, it is surprising that this functional performs best for the reaction energies of the 11 pericyclic reactions with a MAD of 1.4 kcal/mol employing the CAMB3LYP/DZVP-GGA/GEN-A2* level of theory.

Table 5.2: MADs from experiment of ADFT activation energies and reaction enthalpies (in parenthesis) for single point energy calculation with different density functional and basis set employing B3LYP/6-31G*/GEN-A2* optimized reactant, transition state and product structures. All values are in kcal/mol.

BASIS	Functional				
	B3LYP	PBE0	CAMB3LYP	HSE06	LCBLYP
6-31G*	2.2 (3.0)	4.1 (6.0)	4.9 (2.4)	3.5 (4.1)	5.7 (8.1)
DZVP-GGA	2.6 (4.3)	3.5 (4.4)	5.1 (1.4)	2.7 (2.7)	5.1 (6.3)
aug-cc-pVDZ	2.2 (4.7)	3.3 (4.1)	4.5 (1.5)	2.7 (2.6)	4.6 (5.1)
aug-cc-pVTZ	3.4 (7.1)	2.8 (2.5)	5.5 (3.3)	2.7 (2.4)	4.3 (2.6)
aug-cc-pVQZ	3.3 (7.2)	2.7 (2.3)	5.4 (3.2)	2.7 (2.6)	4.2 (2.5)

So far, our analysis clearly demonstrates that hybrid functionals, here PBE0 and HSE06, are most appropriate for the reliable calculation of activation and reaction enthalpies. However, these functionals are computationally very demanding for structure optimization of nanosystems. A possible solution to this problem is a composite approach [136, 137] in which ADFT GGA structure optimizations and frequency analyses are combined with single point global and range-separated ADFT hybrid calculations. Such an approach has already been successfully employed for relative energy calculations of large carbon fullerenes [137] on the nanometer length scale. Table 5.3 list the MADs of the ADFT calculated activation energies and reaction enthalpies with respect to the recommended reference values employing now PBE/DZVP-GGA/GEN-A2* optimized structures. For the activation energies, B3LYP performs again best, either with the 6-31G* or aug-cc-pVDZ basis set. As the comparison of Table 5.3 with Table 5.2 shows the change of the structure optimization method has only little effect on the MADs of the activation energies. The same is also true for the corresponding

reaction enthalpy MADs.

Table 5.3: MADs from experiment of ADFT activation energies and reaction enthalpies (in parenthesis) for single point energy calculation with different density functional and basis set employing PBE/DZV-GGA/GEN-A2* optimized reactant, transition state and product structures. All values are in kcal/mol.

	Functional				
BASIS	B3LYP	PBE0	CAMB3LYP	HSE06	LCBLYP
6-31G*	2.2 (2.7)	4.4 (6.4)	5.0 (2.9)	3.7 (4.4)	5.8 (8.6)
DZVP-GGA	2.5 (4.2)	3.7 (4.6)	4.9 (1.4)	2.9 (2.9)	5.1 (6.5)
aug-cc-pVDZ	2.1 (4.5)	3.6 (4.2)	4.4 (1.3)	2.9 (2.7)	4.8 (5.5)
aug-cc-pVTZ	3.0 (6.7)	3.0 (2.8)	5.2 (2.8)	2.6 (2.2)	4.3 (3.1)
aug-cc-pVQZ	2.9 (6.7)	3.0 (2.7)	5.2 (2.7)	2.7 (2.2)	4.2 (3.0)

Altogether, this study suggests that the ADFT approaches PBE0/aug-cc-pVXZ/GEN-A2* (X=T,Q) and HSE06/aug-cc-pVTZ/GEN-A2* are best suited for the overall description of the studied pericyclic reactions.

5.1.2   Diels-Alder Reactions on C_{60}

As discussed in the previous section, pericyclic reactions are usually rearrangement reactions wherein the transition state of the molecule has a cyclic geometry, and the reaction progresses in a concerted fashion. The most famous example is the Diels-Alder reaction which occurs between a conjugated diene and a, usually conjugated, dienophile. It was formulated by Diels and Alder in 1928 [138] and due to its importance in synthetic organic chemistry rewarded them the Nobel Prize in Chemistry in 1950.

Fullerenes are a large class of allotropes of carbon and have attracted considerable attention in different fields of science since their discovery. The structures of the two most commonly used fullerenes, C_{60} and C_{70}, have been determined since long time [139–141]. The shape of C_{60} is very closed to spherical, the C atoms forming a truncated icosahedron resembling the shape of a soccer ball with a cage diameter of 7.1 Å. Fig. 5.3 shows the structure of C_{60} which has I_h symmetry with equivalent carbon atoms and follows the isolated pentagon rule (IPR). Therefore, it has two different types of C-C bonds, namely, the [6,6] bonds in hexagon-hexagon ring junctions and the [5,6] bonds in the connection between a hexagon and a pentagon. The two different C-C bond types are depicted in Fig. 5.3, too. The bond lengths of [6,6] and [5,6] junctions are 1.401 Å and 1.458 Å, respectively [142, 143].
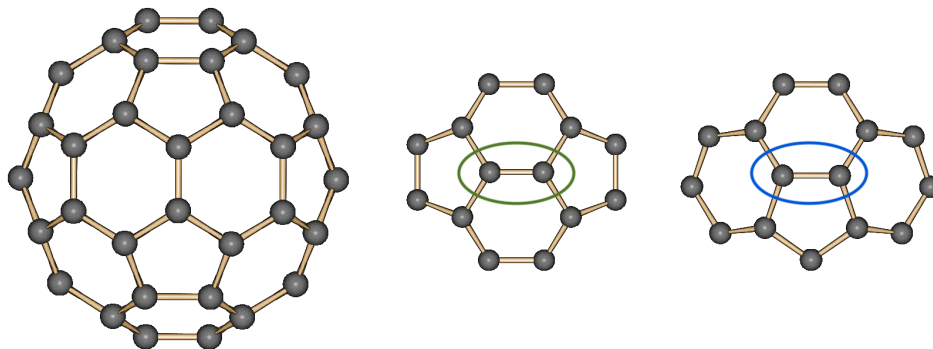
Figure 5.3: Structure of the C_{60} fullerene cage and the two types of ring junctions in a pyracylenic unit [6,6] (green circle) and corannulenic unit [5,6] (blue circle).

For the Diels-Alder reaction between cyclopentadiene as diene and C_{60} as dienophile, Pang and Wilson [144] reported an activation energy of 6.9 kcal/mol. For the corresponding retro Diels-Alder reaction of C_{60} and cyclopentadiene Giovane et al. [145] reported an activation energy of 26.7 kcal/mol. From the combination of these two activation energies a reaction energy of around -19.8 kcal/mol can be estimated. Due to structure of C_{60} three different configurations for the Diels-Alder addition of cyclopentadiene are possible as depicted in Fig. 5.4. They are named **66**, **56-1** and **56-2** according to addition over the pyracylenic or coranulenic bonds.

66   **56-1**   **56-2**
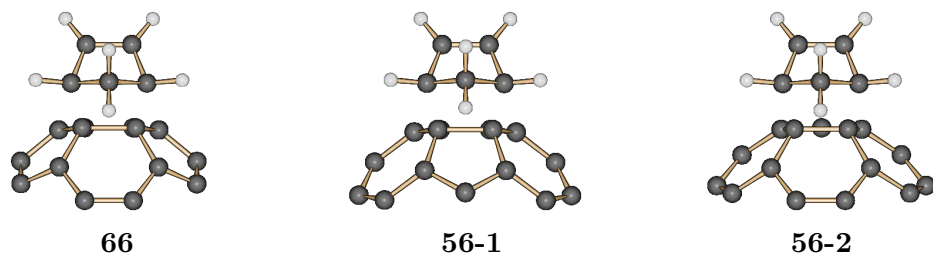
Figure 5.4: Three possible configuration for the Diels-Alder addition of cyclopentadiene with C_{60} over the [6,6] (**66**) and [5,6] (**56-1** and **56-2**) bonds.

In order to perform an ADFT theoretical study of the Diels-Alder reaction of cyclopentadiene with C_{60} we follow the same strategy as for the study of the pericyclic reactions. First we optimize the structures of the reactants, products and transition states at PBE/DZVP-GGA/GEN-A2* level of theory. The optimized structures were characterized by frequency analysis. The double ended saddle interpolation was then used to obtain the initial structures of the transition states which in turn were optimized by a local uphill trust region method.

Finally, the IRC was computed. The C_{60} optimized bond lengths are 1.408 Å and 1.459 Å for the [6,6] and [5,6] bonds, respectively. Thus, the computed bond lengths differ by less than 0.01 Å from the corresponding experimental values. They are also in good quantitative agreements with the results from Yang et al. [146] who found at the M06-2X/6-31G* level of theory optimized bond lengths of 1.387 Å abd 1.451 Å for the [6,6] and [5,6] bonds in C_{60}, respectively.

The PBE/DZVP-GGA/GEN-A2* optimized transition states and products of the Diels-Alder reaction between cyclopentadiene and C_{60} are shown in Fig. 5.5. The calculated distance between C_{60} and cyclopentadiene in the **66** bond Diels-Alder addition for the transition state and product are 2.25 Å and 1.60 Å, respectively. These results compare favorably with those reported by Yang et. al. [146] of 2.22 Å for the transition state and 1.58 Å for the product by employing the M06-2X/6-31G* methodology. Similar agreements are found for the **56-1** and **56-2** Diels-Alder reaction of cyclopentadiene with C_{60}.
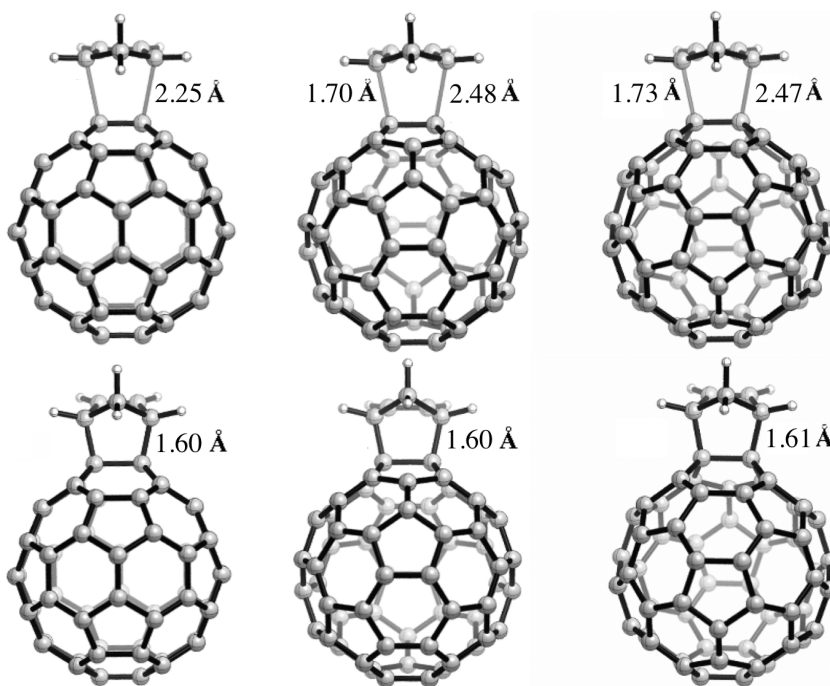
Figure 5.5: PBE/DZVP-GGA/GEN-A2* optimized transition states structures (top) and products structures (bottom). From left to right **66**, **56-1** and **56-2** addition. Relevant bond lengths are also given.

Having the reactants, products and transition states optimized, we can calculate the activation and reaction energies for the different Diels-Alder cycloadditions of cyclopentadiene with

C_{60}. The obtained activation energies, E_a, and reaction energies, E_{rxn}, are listed in Table 5.4 along with the corresponding experimental results. Previous experimental and theoretical investigations revealed that the [6,6] bond is shorter and has a larger π-electron density, resulting in its higher dienophil reactivity than the [5,6] bonds [144–150]. This is confirmed by our results for the **66** addition which shows the smallest activation energy of 8.9 kcal/mol for the cycloaddition of cyclopentadiene with C_{60}. We also note that the corresponding transition state (Fig. 5.5 top left) has equal bond distances between cyclopentadiene and C_{60} which is caracteristic for a truly concerted reaction. On the other hand, the activation energies for the **56** additions are much larger and the corresponding transition states ares much more asymmetric. Whereas the PBE/DZVP-GGA/GEN-A2* activation energy for the **66** addition of cyclopentadiene with C_{60} is in fair quantitative agreement with experiment, the corresponding reaction energy is significantly too small and only in qualitative agreement with experiment. Nevertheless, our results confirm the experimental finding that cycloaddition of cyclopentadiene with C_{60} takes place over the [6,6] bond along the reaction path depicted in Fig. 5.6.

Table 5.4: PBE/DZVP-GGA/GEN-A2* activation and reaction energies of the three different Diels-Alder addition of cyclopentadiene with C_{60}. See Fig. 5.4 for the labeling. All values are in kcal/mol.

| | Exp. | Sites of cycloadition | | |
		66	**56-1**	**56-2**
E_a	6.9	8.9	18.7	17.2
E_{rxn}	-19.8	-12.4	3.9	4.2

To investigate the influence of the DFA on the activation energy and reaction energy for the **66** addition of cyclopentadiene with C_{60} we performed ADFT and DF-DFT single-point energy calculations using the B3LYP hybrid functional and the M06-2X [151] hybrid meta-GGA functional, respectively. These calculations were performed with the PBE/DZVP-GGA/GEN-A2* optimized geometries. In both cases the 6-31G* basis set was employed in combination with the GEN-A2* auxiliary functions set in order to compare directly with literature values. Table 5.5 lists the activation and reaction energies for the **66** Diels-Alder reaction of cyclopentadiene with C_{60}. Values in parenthesis refer to literature results [146, 147]. Our B3LYP/6-31G*/GEN-A2* activation energy differs by less than 0.1 kcal/mol
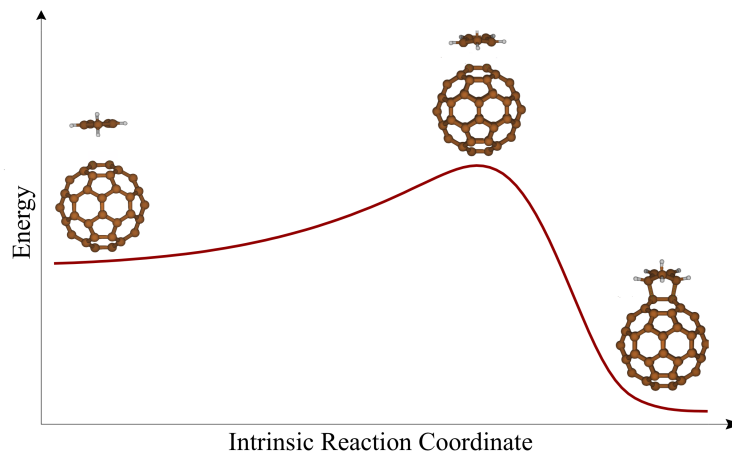
Figure 5.6: Intrinsic reaction coordinate for the Diels-Alder reaction of cyclopentadiene with C_{60}. Note concerted nature of transition state.

from the one reported by Osuna et al. [147] employing the B3LYP/6-31G* four-center ERI Kohn-Sham methodology. Similar, our DF-DFT M06-2X/6-31G* activation energy matches perfectly with the one from Yang et al. [146] using a four center ERI code. For the reaction energies larger differences are observed. While the M06-2X/6-31G* DF-DFT and four-center ERI DFT reaction energy differ by less than 1.0 kcal/mol the ADFT B3LYP/6-31G* reaction energy is more than 3.0 kcal/mol lower than its four-center ERI counterpart. Note, however, that the ADFT reaction energy is closer to experiment. In any case, neither the B3LYP/6-31G* nor the M06-2X/6-31G* results improve significantly over the PBE/DZVP-GGA ones given in Table 5.4.

Table 5.5: B3LYP/6-31G*/GEN-A2* and M06-2X/6-31G*/GEN-A2* activation and reaction energies for the **66** Diels-Alder reaction of cyclopentadiene with C_{60}. Values in parentheses refer to literature results from Ref. [147] for B3LYP and Ref. [146] for M06-2X. All values are in kcal/mol.

	Exp.	B3LYP	M06-2X
E_a	6.9	17.9 (18.0)	6.5 (6.5)
E_{rxn}	-19.8	-9.8 (-6.6)	-27.9 (-27.1)

To investigate further how functionals and basis sets influence the energetic of this Diels-Alder reaction we performed composite calculations of the form DFA/aug-cc-pVTZ/GEN-A2*//PBE/ DZVP-GGA/GEN-A2*. Here DFA refers to the functional used for the single point energy calculation on top of the PBE/DZVP-GGA/GEN-A2* optimized structures. These approaches are motivated by the success of the PBE0/aug-cc-pVTZ/GEN-A2*//PBE/

DZVP-GGA/GEN-A2* composite approach for the calculation of large fullerenes [137] and for the study of hydrocarbon pericyclic reactions [136].

Table 5.6 reports calculated activation and reaction energies computed with the GGA PBE fucntional, B3LYP and PBE0 global hybrid functionals and the M06-2X meta-GGA hybrid functional. As the comparison of this table with Table 5.4 shows, the increase in the basis set size does not improve the activation energy or reaction energy obtained with the PBE functional. We attribute this to the composite approach itself which carries an intrinsic error in the range of 1.0 kcal/mol due to the different basis sets used for structure optimization and energy calculation [137]. The comparison of the B3LYP entries in Table 5.5 and 5.6 reveal that also this functional does not benefit from the enlarged basis set in the energy calculation. Note the agreement with the corresponding results for the pericyclic reactions. This further supports the assumption that B3LYP is indeed optimized for the 6-31G* basis set. On the other hand, enlarging the basis set size for energy calculations is beneficial for M06-2X as the comparison of the corresponding entries of Table 5.5 and 5.6 reveal. Whereas the already very good activation energy is only slightly improved, namely from 6.5 to 7.1 kcal/mol (vs. 6.9 kcal/mol experimentally), the improvement in the reaction energy is significant. Here the error to experiment is reduced from 8.1 to 4.7 kcal/mol. We also note that the PBE0/aug-cc-pVTZ/GEN-A2*//PBE/DZVP-GGA/GEN-A2* composite approach yields results comparable to the M06-2X one, now, however, with improved accuracy for the reaction energy and diminished accuracy for the activation energy.

Table 5.6: Calculated activation and reaction energies using the PBE GGA functional, the B3LYP and PBE0 global hybrid functionals and M06-2X hybrid meta-GGA functional for the Diels-Alder cycloadition of cyclopentadiene with C_{60}. All values are in kcal/mol.

	Exp.	PBE	B3LYP	PBE0	M06-2X
E_a	6.9	10.8	20.5	12.4	7.1
E_{rxn}	-19.8	-11.5	-3.9	-18.7	-24.5

The calculated activation and reaction energies for the Diels-Alder reaction between cyclopentadiene and C_{60} using the CAMB3LYP, CAMPBE0, HSE06, LCBLYP and LCPBE range-separated hybrid functionals are listed in Table 5.7. This table shows that the use of range-separated hybrid functionals does not improve the results. The best calculated activation energy is obtained with the CAMPBE0 functional that, however, severally overestimates

the corresponding reaction energy by around 15 kcal/mol. This overestimation of the reaction energy is also found for the LCPBE functional. On the other hand, the CAMB3LYP and HSE06 functionals severely underestimate the experimental reaction energy as can be seen from Table 5.7. In general, the performance of the range-separated hybrid functionals for the Diels-Alder addition of cyclopentadiene with C_{60} is rather disappointing. None of them come close to the accuracies for activation and reaction energies obtained with PBE0 and M06-2X. In particular, HSE06 that showed best overall performance for small pericyclic reactions is failing for the here discussed Diels-Alder reaction.

Table 5.7: Calculated activation and reaction energies using the CAMB3LYP, CAMPBE0, HSE06, LCBLYP and LCPBE range-separated hybrid functionals for the Diels-Alder reaction of cyclopentadiene with C_{60}. All values are in kcal/mol.

	Exp.	CAMB3LYP	CAMPBE0	HSE06	LCBLYP	LCPBE
E_a	6.9	20.33	8.38	16.39	13.54	5.63
E_{rxn}	-19.6	-10.62	-35.03	-10.85	-22.53	-33.81

In conclusion, we find that only the M06-2X meta-GGA and PBE0 global hybrid functionals yield semi-quantitative results for the here studied cycloaddition of cyclopentadiene with C_{60}. Enlarging basis set size for energy calculations with hybrid functionals is generally advisable, except for B3LYP which seems to be optimized for the 6-31G* basis set. The proposed composite approach [137] consisting of GGA structure optimizations and single point hybrid energy calculations is also applicable for the calculation of chemical reactions. Once an appropriate functional is pinpointed, it is straightforward with the here presented methodology to perform full structure optimizations at the hybrid level employing large basis sets. In particular, this investigation underlines the need for more systematic reaction studies of nanosystems with a wide variety of (hybrid) functionals in order to find appropriate theoretical methodologies. With the newly developed variational fitting for global and range-separated Fock exchange such studies of chemical reactions on large molecular systems are now readily available.

5.2   Polarizabilities of Small Molecules

The molecular polarizability describes the tendency of a molecule to deform or polarize in response to an applied electric field. As such, this quantity governs key intra- and inter-

molecular interactions such as induction and dispersion, plays a key role in determining the spectroscopic signatures of molecules and is an essential ingredient in polarizable force fields and other empirical models for collective interactions [152]. Therefore, there is an increasing demand for reliable static and dynamic polarizability calculations of molecules. To this end, we have calculated the static and dynamic polarizability of a set of small molecules and compare our results with experimental data. For all calculations the aug-cc-pVTZ basis sets in combination with the GEN-A2* auxiliary function sets were used. For all molecules the experimental structures [123] are employed

In Table 5.8 we compare average static polarizabilities obtained from Hartree-Fock, BLYP and PBE GGA functionals, B3LYP and PBE0 global hybrid functionals as well as CAMB3LYP, CAMPBE0, HSE06, LCBLYP and LCPBE range-separated hybrid functionals with corresponding experimental data. As can be seen from this table, Hartree-Fock calculations yield a rather large MAD of 1.41 a.u. due to the systematic underestimating of the experimental polarizabilities. This result is in perfect agreement with the literature [153]. The MADs of the BLYP and PBE GGA functionals are 0.62 and 0.36 a.u., respectively. Table 5.8 shows that the polarizabilities calculated with GGAs usually overestimate the corresponding experimental data. The observed polarizability overestimation by the BLYP functional has already been reported [154]. The corresponding MAD obtained with the the B3LYP and PBE0 global hybrid functional are 0.20 and 0.48 a.u., respectively. Here, the B3LYP fucntional shows an improvement with respect to the MAD obtained with Hartree-Fock and GGAs while PBE0 does not. CAMPBE0 and HSE06 range-separated hybrid functionals do not improve substantially the GGA MADs and are far from the B3LYP MAD. The CAMB3LYP and LCBLYP functionals improves the MAD of the PBE functional and show a MAD very closed to the one obtained with B3LYP. The smallest MAD of 0.13 a.u. corresponds to the long-range corrected LCPBE functional as it is shown in Table 5.8.

ADFT dynamic polarizabilities of 10 small molecules were calculated at the Hartree-Fock, GGA (BLYP and PBE), global hybrid (B3LYP and PBE) and range-separated hybrid (CAMB3LYP, CAMPBE0, LCBLYP, LCPBE and HSE06) level of theory. Again the aug-cc-pVTZ/GEN-A2* basis sets and auxiliary functions sets were used.

Table 5.8: Comparison of static Hartree-Fock, GGA, hybrid and range-separated hybrid ADPT polarizabilities [a.u.] of small molecules with experiment. For all molecules the experimental structures are used.

	Fock	BLYP	PBE	B3LYP	PBE0	CAMB3LYP	CAMPBE0	HSE06	LCBLYP	LCPBE	Exp
HF	4.75	5.88	5.96	5.63	5.43	5.54	5.38	5.42	5.74	5.76	5.40^a
CH_4	15.99	17.21	17.05	17.04	16.60	16.87	16.58	16.46	16.96	17.09	17.27^b
CH_3F	15.57	17.61	17.47	17.11	16.70	16.89	16.54	16.61	17.06	17.19	17.32^b
HCl	16.45	18.11	17.68	17.64	17.07	17.34	16.85	17.02	17.36	17.35	17.54^c
H_2S	23.61	25.72	25.20	25.21	24.29	24.62	24.04	24.17	24.54	24.62	24.66^d
CH_2F_2	15.89	18.63	18.56	17.92	17.53	17.71	17.36	17.47	18.06	18.21	18.20^b
OCS	33.10	35.07	34.56	34.35	33.84	34.20	33.64	33.78	34.50	34.26	34.33^b
SO_2	23.55	26.38	26.08	25.49	25.06	25.24	24.70	25.01	25.55	25.49	25.49^e
CF_4	16.81	20.32	20.20	19.35	18.96	19.18	18.75	18.93	19.72	19.77	19.53^b
CS_2	55.32	56.22	55.48	55.61	54.86	55.61	54.83	54.75	56.01	55.42	55.38^b
MAD	**1.41**	**0.62**	**0.36**	**0.20**	**0.48**	**0.27**	**0.65**	**0.55**	**0.24**	**0.13**	

[a] Static value from refractive index dispersion [155]
[b] Static value from refractive index dispersion [156]
[c] Depolarized light scattering at $\lambda = 638$ nm [157]
[d] Extrapolated static value from dispersion of dynamic average polarizability [158]
[e] Static value from refractive index and Rayleigh scattering dispersion [158]

Table 5.9: Comparison of dynamic Hartree-Fock, GGA, global hybrid and range-separated hybrid ADPT polarizabilities [a.u.] of small molecules with experiment. For all molecules the experimental structures are used.

	Fock	BLYP	PBE	B3LYP	PBE0	CAMB3LYP	CAMPBE0	HSE06	LCBLYP	LCPBE	Exp
NH_3	13.15	15.85	15.63	15.21	14.53	14.72	14.16	14.40	14.74	14.89	14.98[a]
H_2O	8.61	10.80	10.59	10.14	9.76	9.96	9.64	9.71	10.22	10.26	9.92[b]
N_2	11.68	12.52	12.38	12.18	12.04	12.16	12.02	12.02	12.35	12.30	11.92[a]
CO	12.54	13.90	13.87	13.52	13.32	13.45	13.23	13.29	13.72	13.71	13.34[a]
N_2O	18.86	20.45	20.21	19.98	19.66	19.94	19.62	19.64	20.23	20.13	20.24[a]
CO_2	16.00	18.06	17.88	17.54	17.22	17.45	17.10	17.20	17.75	17.72	17.75[a]
Cl_2	30.22	31.99	31.61	31.33	30.81	31.07	30.48	30.74	31.19	31.05	31.11[a]
C_2H_4	29.08	29.64	29.15	29.30	28.61	28.98	28.35	28.48	28.86	28.73	28.48[a]
C_2H_6	27.92	30.27	30.06	29.60	29.09	29.29	29.01	28.87	29.48	29.78	30.16[a]
C_6H_6	70.76	73.38	72.62	72.46	71.23	71.57	70.39	70.90	71.49	71.32	70.18[a]
MAD	**1.16**	**0.88**	**0.62**	**0.52**	**0.44**	**0.40**	**0.47**	**0.45**	**0.38**	**0.31**	

[a] Depolarized light scattering at $\lambda = 638$ nm [157]
[b] Depolarization ratio from Rayleigh scattering at $\lambda = 514.5$ nm [158]

The dynamical polarizabilities were calculated at the experimental wavelength as indicated in Table 5.9 which compares the calculated results with corresponding experimental data. Similar to the static polarizabilities (Table 5.8) Hartree-Fock dynamic polarizabilities tend to underestimate the experimental values. With Hartree-Fock a MAD of 1.16 a.u. is obtained. This result is improved using BLYP and PBE GGA functionals. The corresponding MADs are 0.88 and 0.66 a.u., respectively. The obtained GGA MADs are improved employing the B3LYP (0.52 a.u.) and PBE0 (0.44 a.u.) global hybrid functionals. The CAMPBE0 and HSE06 range-separated hybrid functionals yield similar MADs as the PBE0 functional, while CAMB3LYP and LCBLYP functionals improve these results by approximately 0.05 a.u. The LCPBE functional with a MAD of 0.31 a.u. improves even more the here studied dynamic polarizabilities of small molecules. The calculated static and dynamic polarizabilities with LCPBE are in excellent agreement with experiment. Note that LCPBE compared worst of all range-separated hybrid functionals with CCSD/aug-cc-pVTZ reference data (see Table 4.4). This might indicate that CCSD/aug-cc-pVTZ is either still not sufficiently well correlated or that the used aug-cc-pVTZ basis is not flexible enough to yield highly accurate static and dynamic polarizabilities. Thus, further studies, where reliable experimental data are used as reference, are needed. These results confirm that range-separated hybrid functionals can yield highly accurate static and dynamic polarizabilities that compare favorable, or even outperform, correlated wave-function approaches.

5.3   X-ray Photoelectron Spectroscopy

Core-level shifts in X-ray Photoemission Spectroscopy (XPS) are commonly used to obtain information on the chemical environment of specific atoms in a given system. From a computational perspective they are often decomposed into initial and final state contributions and this was also the aim of ESCA (Electron Spectroscopy for Chemical Analysis) [159], i.e. to obtain information on the initial charge distribution and oxidation state of the probed atom as well as its chemical environment and conformation. The ethyl trifluoroacetate (CF_3-CO-O-CH_2-CH_3), also known as the ESCA molecule, is the most illustrative showcase for core level shifts. Historically the molecule had been synthesized in order to give an illustrative example of what could be learned from core photoelectron spectroscopy [159]. It contains four

carbon atoms in different chemical environments. The carbon 1s binding energy decreases from the CF_3 end onwards as can be seen from Fig. 5.7.
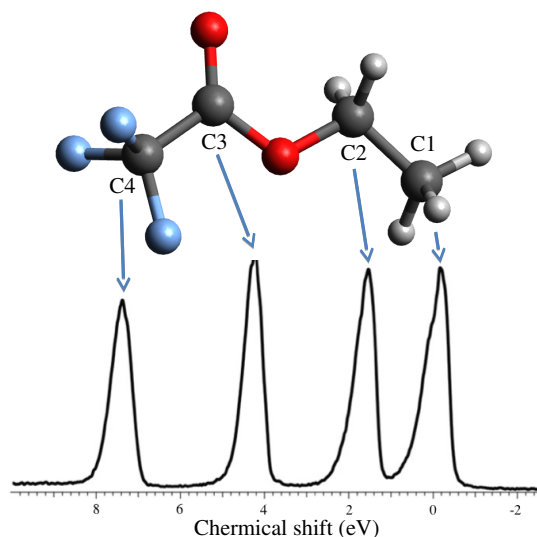
Figure 5.7: C 1s photoelectron spectrum of ethyltrifluoroacetate taken from Ref. [160] . Color legend: violet - Fluorine, grey - Carbon, red - Oxygen, white - Hydrogen.

It is well know that when computing shifts as a total energy difference, the initial state cancels out and the shift is obtained as the energy difference between the different core-hole states. In the actual experimental set-up there is only one initial electronic state also for a molecule or system with many inequivalent atomic sites. This has led to a proposal to interpret experimental XPS shifts in terms of the different final states using the Z+1 approximation [161]. The inner-most core-level, 1s, of an atom is spherically symmetric and largely screens two positive charges of the nucleus. Removing one electron from this level effectively increases the nuclear charge felt by the valence electrons by one unit, i.e. transforming the atom to the next on the right in the periodic table; this is the Z+1 approximation.

The calculations on the ESCA molecule were performed with ADFT methodology implemented in the deMon2k program. The PBE, BLYP, B3LYP, PBE0, LCBLYP, LCPBE0, CAMB3LYP and CAMPBE0 were used as exchange-correlation functionals. The XPS shifts were computed in two ways: (i) as total energy differences between explicit core-hole states in a SCF procedure and (ii) as total energy differences between the valence-ionized molecule with the selected atom replaced by its Z+1 counterpart (e.g. carbon replaced by nitrogen).

In the latter case the core level of the Z+1 atom was fully occupied. By systematically increasing the basis sets we obtained converged results with the all-electron aug-cc-pVTZ basis set which in turn was employed for all here reported molecular calculations. In the core-hole calculations quasi-relativistic effective core potentials (QECPs) [162] were used for the non-ionized carbon atoms leaving four valence electrons and no core-electrons on these sites. The structures of the anti-anti and anti-gauche conformers of the ESCA molecule were optimized at PBE/aug-cc-pVTZ/GEN-A2* level of theory. The obtained minimum structures showed in the Fig. 5.8 were confirmed by frequency analysis.
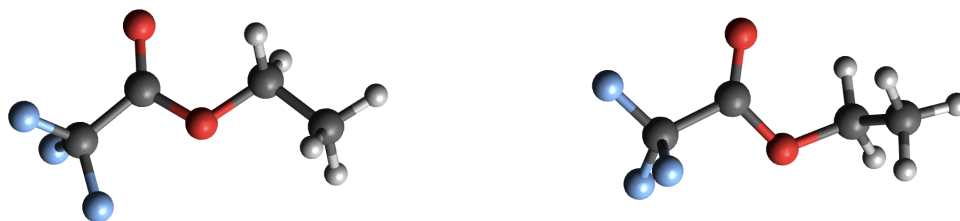
Figure 5.8: PBE/aug-cc-pVTZ/GEN-A2* optimized structures of the anti-anti (left) and anti-gauche (right) conformers of the ESCA molecule.

Table 5.10 reports averaged core-level shifts of the ESCA molecule computed with GGA and global hybrid functionals as the energy difference between the neutral ground state and the core-ionized molecule at the respective site. The structures are PBE/aug-cc-pVTZ/GEN-A2* optimized and averaged results refer to a 56:44 mixture of the anti-anti and anti-gauche conformers as suggested by gas phase electron diffraction (GED) analysis of the ESCA molecule [163]. In parenthesis we also report the corresponding values obtained with the Z+1 approximation. The GGA results show rather large deviations of 0.2 0.6 eV from the experimental reference. Using global hybrid functionals this deviation is reduced to around 0.2 eV. These results are in perfect agreement with the ones reported by Van den Bossche et al. [45]. Concerning the Z+1 approximation, Table 1 shows that independent of the functional the results obtained by changing carbon to nitrogen differ by less than 0.1 eV from the explicitly calculated ones. This shows that interpreting the shifts within the Z+1 approximation is within the intrinsic accuracy of global hybrid functionals for core-level shift calculations and that the conceptually simple Z+1 final-state picture holds very well.

Table 5.11 reports averaged core-level shifts computed with range-separated hybrid function-

Table 5.10: Calculated averaged core level shifts using the PBE and BLYP GGA functionals and the PBE0 and B3LYP global hybrid functionals. Values in parenthesis refer to the Z+1 approximation. All values are in eV. The experimental data are taken from Ref. [160].

	Exp.	PBE	BLYP	PBE0	B3LYP
C1	0.00	0.00 (0.00)	0.00 (0.00)	0.00 (0.00)	0.00 (0.00)
C2	1.72	1.54 (1.56)	1.51 (1.53)	1.66 (1.68)	1.61 (1.63)
C3	4.33	3.77 (3.74)	3.85 (3.79)	4.27 (4.23)	4.27 (4.20)
C4	7.46	6.78 (6.86)	6.86 (6.90)	7.27 (7.38)	7.27 (7.35)

als using the optimized structures from above. Agreement with experiment can be further improved with the CAM range-separated hybrid functionals. In particular, the CAMB3LYP results show the best agreement with experiment. For this functional, the largest deviation between explicitly calculated core level shifts and the Z+1 approximation is 0.12 eV, which is still below the maximum deviation between experiment and theory. Note also the excellent agreement between the CAMB3LYP Z+1 approximation and experiment with all core-level shifts within 0.05 eV of the experimental value.

Table 5.11: Calculated core level shifts using range-separated hybrid functionals LCPBE, LCBLYP, CAMPBE0 and CAMB3LYP. Values in parenthesis use the Z+1 approximation. The experimental data are taken from Ref. [160]. All values are in eV.

	Exp.	LCPBE	LCBLYP	CAMPBE0	CAMB3LYP
C1	0.00	0.00 (0.00)	0.00 (0.00)	0.00 (0.00)	0.00 (0.00)
C2	1.72	1.68 (1.68)	1.67 (1.67)	1.75 (1.77)	1.67 (1.68)
C3	4.33	4.29 (4.17)	4.45 (4.26)	4.62 (4.51)	4.49 (4.37)
C4	7.46	7.22 (7.26)	7.37 (7.35)	7.56 (7.64)	7.46 (7.50)

In order to study structure relaxation effects within the Z+1 approximation, CAMB3LYP/aug-cc-pVTZ/GEN-A2* optimizations were performed for the anti-anti and anti-gauche conformers of the ESCA molecule and their core-ionized or Z+1 approximated counterparts. The optimized structures of the C1, C2 and C3 (see Fig. 5.7) core-ionized or Z+1 approximated conformers are topologically identical to the non-ionized structures with bond length changes below 0.01 Å. The agreement between the structures optimized with the explicit core hole and the Z+1 approximation is in the same range, i.e. with differences below 0.01 Å. For the C4 core-ionized structure, a much larger relaxation effect is found as shown in Figure 5.8 and also previously reported in the literature [160]. Here the C3-C4 bond lengths stretch

considerably with respect to the anti-anti and anti-gauche reference structures after core ionization as can be seen from Fig. 5.9. This structural deformation results in a linear CO_2 unit from the ether and carbonyl oxygens, with bonds weakly to the CF_3 moiety over the central carbon atom. In the explicit core-hole calculations C3-C4 bond lengths of 2.81 and 2.80 Å are found for the anti-anti and anti-gauche conformers, respectively. With the Z+1 approximation, these bond distances increase to 2.93 and 2.92 Å. These results are in fair agreement with the calculations from Travnikova et al. [160] who found bond distances in the range of 2.9 Å.
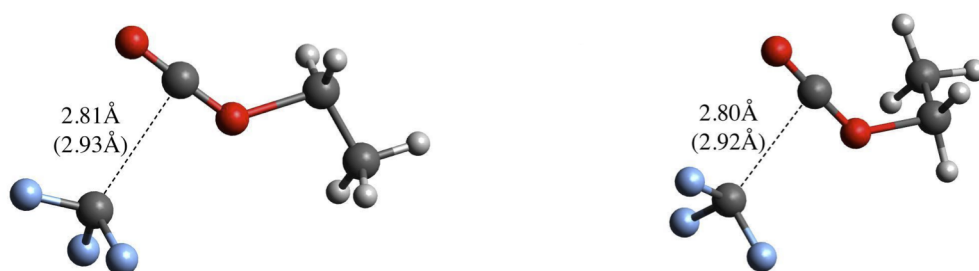
Figure 5.9: CAMB3LYP/aug-cc-pVTZ/GEN-A2* optimized structures of the ESCA molecule on the left the anti-anti C4 core-ionized state and on the right anti-gauche C4 core-ionized state. Values in parenthesis correspond to optimized structures with the Z+1 approximation.

From the above discussion we can conclude that independent of the functional, the Z+1 approximation yields results very closed to the explicitly calculated core excitation and provides a chemically intuitive understanding of shifts in XPS peak positions in terms of differences in chemical bonding between the initial molecule and the core-ionized atom replaced by the next atom to the right in the periodic table. Furthermore, the Z+1 approximation is less computationally expensive than the explicit core-hole calculation. In addition, the Z+1 approximation has been successfully used for surface-core-level shifts (SCLS) for the close-packed surfaces of second-row transition metals [164]. We also note that the here proposed methodology for the calculation of core-level excitations with global and range-separated hybrid functionals can be straightforward extended to nanosystems.

Chapter 6
Conclusions and Pespectives

This thesis reports the implementation, validation, benchmarking and application of range-separated hybrid functionals in the framework of density fitted Kohn-Sham (DF-DFT) and auxiliary density functional theory (ADPT). From this work the following conclusions can be drawn.

The newly developed variational fitted long-range exact exchange algorithm was successfully validated against conventional four-center ERI algorithms. This validation shows that long-range four-center ERIs can be approximated by variational Fock potential fitting without loss of accuracy [106]. On the basis of these results, a computationally efficient implementation of range-separated hybrid functionals free of four-center ERIs is presented. The accuracy in the energy calculations and structure optimizations of the here implemented functionals are in excellent agreement with their four-center ERI Kohn-Sham DFT counterparts. The corresponding serial benchmark calculations show significant speedups (~ 80) for one SCF step in comparison to four-center ERI implementation in NWChem. Moreover, an efficient and scalable parallelization is presented. In particular, we demonstrate that the parallel performance benefits from the use of the modified Cholesky decomposition instead of the TED of the Coulomb matrix. Our analysis shows that the improved parallel scaling results from a more homogeneous workload balance due to the modified Cholesky decomposition of the Coulomb matrix.

The successful extension of the ADPT working equations for global and range separated hybrid functionals opens an avenue for the systematic study of response properties of large molecular systems using these functionals. The here presented comparison of static and dynamic polarizabilities of small molecules with available experimental data demonstrates the need of range-separated hybrid functionals for these property calculations. The CAMPBE0

and HSE06 functionals show the best match with CCSD polarizabilities and hyperpolarizabilities. However, comparison with experimental data indicates that LCPBE is best suited for static and dynamic polarizability calculations. We attribute this to the CCSD/aug-cc-pVTZ reference data that include larger intrinsic errors with respect to experimental reference data than some of the used range-separated hybrid functionals employing aug-cc-pVTZ/GEN-A2* basis and auxiliary function sets. Although, these results are obtained with a preliminary proof-of-principle implementation, they guide the path to first-principle calculations of non-linear optical properties of nanosytems.

In this thesis we have also investigated the performance of range-separated hybrid functionals for the calculation of activation and reaction energies. The calculated activation and reaction energies of small pericyclic hydrocarbon reactions show that hybrid functionals improve in general the results from GGAs. In particular, we show that composite approaches, consisting of GGA structure optimization and single point hybrid energy calculations, are well suited for the study of pericyclic reactions. Best results are obtained with the PBE0 global hybrid functional and the HSE06 range-separated hybrid functional. Unfortunately, it is not straightforward to extrapolate the results from small pericyclic reactions to corresponding nanosystem reactions as our study of the [4+2] Diels-Alder cycloaddition of cyclopentadiene with C_{60} showed.

The Z+1 approximation was employed as a more chemical intuitive picture for the simulation of X-ray photoemission spectroscopy. The calculation of the explicit core-hole excitation as well as the alternatively Z+1 approximation for the ESCA molecule evidenced that the use of hybrid functionals is needed for an accurate description of X-ray photoelectron spectra.

Immediate perspectives resulting from this thesis are the following:

1. **Extension of ADPT for global and range separated functionals to open shell**
   The newly derived ADPT working equations are restricted to closed-shell systems. Although, the extension to open-shell is rather straightforward care has to be taken in the corresponding implementation. In particular, the localization of α and β MOs needs further consideration. This might result in a new localization approach that is more suitable for the variational fitting of Fock potential than the current 2 step algorithm [34].

2. Parallelization of new ADPT working equations

In order to perform large scale polarizability calculations, it is mandatory to implement an efficient parallel scheme for the calculation of the perturbation vector $\overset{\bullet}{\mathbf{b}}{}^{(\lambda)}(\omega)$ in the global and range-separated ADPT equation system.

3. Perturbation theory for magnetic interactions

Magnetic shieldings and spin-spin coupling constants are interesting molecular properties that can be calculated as response properties to the perturbation with an external or internal magnetic field. For LDA and GGA these properties can be calculated within the ADPT framework [165]. Note the missing response in the shielding tensor calculations at this level of theory. With the newly developed ADPT equations these magnetic response calculations can be extended to global and range-separated hybrid functionals.

4. Static and dynamic polarizabilities of oligothiophenes

In a previous work [166] we showed that the dynamical polarizabilities of oligothiophenes can be correctly described with GGAs only until four units, i.e. the tetramer. For the following two polymers, pentamer and hexamer, this level of theory failed to reproduce the experimental dynamical polarizabilities. A detailed analysis revealed that the GGA poles of the dynamical polarizabilities of these systems were too closed to the frequency at which the experiment was performed. Thus, the wrong position of the GGA dynamical polarizability poles is responsible for the failure at this level of theory. From the literature it is well known that hybrid functionals enlarge the energy differences between occupied and unoccupied MOs. Thus, we assume that the position of the dynamical polarizability pole will move away, which in turn will yield better agreement to experiment than at GGA level of theory.

5. Cycloaddition reactions of polyacenes with fullerenes

Further systematic studies are needed to pinpoint hybrid functionals that yield reliable results with the here discussed composite approach for chemical reactions at the nanometric scale. Experimental activation and reaction energies of cycloadditions between fullerenes and polyacenes like cyclopentadiene, dimethylanthracene and others are available. However, only very few theoretical investigations of such reactions can

be found in the literature due to the associate computational demand. We hope that the developments outlined in this thesis will contribute to change this situation in the near future.

Negative Definiteness of Range-Separated Operators

We wish to show that the error functional

$$\epsilon_2^{\text{RS}} = -\sum_{i,j}^{occ} \iint \left[\rho_{ij}(\mathbf{r}) - \tilde{\rho}_{ij}(\mathbf{r})\right] g(\mathbf{r} - \mathbf{r}') \left[\rho_{ij}(\mathbf{r}') - \tilde{\rho}_{ij}(\mathbf{r}')\right] d\mathbf{r}\, d\mathbf{r}' \tag{A.1}$$

is negative semidefinite. In Eq (A.1) $g(\mathbf{r} - \mathbf{r}')$ is a multiplicative operator depending on the distance between the positions of two electrons. If we write

$$f_{ij}(\mathbf{r}) = \rho_{ij}(\mathbf{r}) - \tilde{\rho}_{ij}(\mathbf{r}) \tag{A.2}$$

the error functional may be rewritten in the form

$$\epsilon_2^{\text{RS}} = -\sum_{i,j}^{occ} \iint f_{ij}(\mathbf{r})\, g(\mathbf{r} - \mathbf{r}')\, f_{ij}(\mathbf{r}')\, d\mathbf{r}\, d\mathbf{r}' \tag{A.3}$$

To proceed, we assume that $g(\mathbf{r} - \mathbf{r}')$ has a well-defined three dimensional Fourier transform, $G(\mathbf{k})$, given by

$$\begin{aligned} G(\mathbf{k}) &= \int g(\mathbf{r} - \mathbf{r}')\, e^{-i\mathbf{k}\cdot\mathbf{r}}\, d\mathbf{r} \\ &= e^{-i\mathbf{k}\cdot\mathbf{r}'} \mathcal{F}_G(k) \end{aligned} \tag{A.4}$$

Based on Eq. (A.4) we can represent $g(\mathbf{r} - \mathbf{r}')$ in terms of its inverse Fourier transform

$$\begin{aligned} g(\mathbf{r} - \mathbf{r}') &= \frac{1}{2\pi} \int G(\mathbf{k}) e^{i\mathbf{k}\cdot\mathbf{r}} d\mathbf{k} \\ &= \frac{1}{2\pi} \int e^{-i\mathbf{k}\cdot\mathbf{r}'} \mathcal{F}_G(k) e^{i\mathbf{k}\cdot\mathbf{r}} d\mathbf{k} \end{aligned} \tag{A.5}$$

Here $\mathcal{F}_G$ was written as a function of $k = |\mathbf{k}|$ because it only depends on the norm of the distance, i.e. $r = |\mathbf{r} - \mathbf{r}'|$. The corresponding Fourier transform of $f_{ij}(\mathbf{r})$ is given as

$$F_{ij}(\mathbf{k}) = \int f_{ij}(\mathbf{r})\, e^{-i\mathbf{k}\cdot\mathbf{r}}\, d\mathbf{r} \tag{A.6}$$

Substituting (A.5) into (A.3) yields

$$
\epsilon_2^{\mathrm{RS}} = -\sum_{i,j}^{occ} \iint f_{ij}(\mathbf{r}) \left[\frac{1}{2\pi} \int e^{-i\mathbf{k}\cdot\mathbf{r}'} \mathcal{F}_G(k) e^{i\mathbf{k}\cdot\mathbf{r}} d\mathbf{k} \right] f_{ij}(\mathbf{r}') \, d\mathbf{r} \, d\mathbf{r}' \tag{A.7}
$$

$$
= -\frac{1}{2\pi} \sum_{i,j}^{occ} \int \mathcal{F}_G(k) \left[\int f_{ij}^*(\mathbf{r}) e^{-i\mathbf{k}\cdot\mathbf{r}} d\mathbf{r} \right]^* \left[\int f_{ij}(\mathbf{r}') e^{-i\mathbf{k}\cdot\mathbf{r}'} d\mathbf{r}' \right] d\mathbf{k} \tag{A.8}
$$

$$
= -\frac{1}{2\pi} \sum_{i,j}^{occ} \int \mathcal{F}_G(k) \, F_{ij}^*(\mathbf{k}) \, F_{ij}(\mathbf{k}) \, d\mathbf{k} \tag{A.9}
$$

$$
= -\frac{1}{2\pi} \sum_{i,j}^{occ} \int \mathcal{F}_G(k) \, |F_{ij}(\mathbf{k})|^2 \, d\mathbf{k} \tag{A.10}
$$

The condition $\mathcal{F}_G > 0$ for $k > 0$ is, according to Bochner's theorem [167], equivalent to the statement that $g(\mathbf{r} - \mathbf{r}')$ is a positive-definite function. Thus, it is sufficient to calculate the Fourier transform of $g(\mathbf{r} - \mathbf{r}')$ and confirm that it is positive for $k > 0$. Table A.1 lists the calculated [168] Fourier transforms of the global, long-range and short range Coulomb operators used in this thesis. In each case, the transforms are strictly positive for $k > 0$.

Table A.1: Fourier transforms for the global, long-range, and short-range Coulomb operators.

Operator	Fourier transform
$\dfrac{1}{\|\mathbf{r} - \mathbf{r}'\|}$	$\dfrac{1}{2\pi k}$
$\dfrac{\mathrm{erf}(\omega\|\mathbf{r} - \mathbf{r}'\|)}{\|\mathbf{r} - \mathbf{r}'\|}$	$\dfrac{1}{2\pi k} e^{-\frac{k^2}{4\omega^2}}$
$\dfrac{\mathrm{erfc}(\omega\|\mathbf{r} - \mathbf{r}'\|)}{\|\mathbf{r} - \mathbf{r}'\|}$	$\dfrac{1}{2\pi k} \left[1 - e^{-\frac{k^2}{4\omega^2}} \right]$

Since $F_{ij}(\mathbf{k})$ is square and $\mathcal{F}_G$ is positive then the sum appearing in Eq. (A.4) is positive definite. Thus, it follows that ϵ_2^{RS} is negative semidefinite, vanishing only for $f_{ij}(\mathbf{r}) = 0$ for every point in space. This derivation follows the same line of arguments as for the positive definiteness proof of range-separated four-center ERIs using the Schwartz inequality [168].

Energy Gradients of $C_{54}H_{20}$

While the parallelization of the potential and energy gradient calculations for the variational fitted Fock exchange was investigated, it was found that hydrogen-terminated graphene sheets needed many optimization steps to reach convergence or did not converge at all. The convergence of the total energy and maximum absolute gradient (MAG) component for the $C_{54}H_{20}$ graphene sheet is plotted in Fig. B.1. For this calculation the standard ERI setting of deMon2k, i.e. the direct calculation of the near-field and far-field ERIs according to the default asymptotic atomic radii, are used. As Fig B.1 shows this setting yields an almost random behavior of the MAG component during the structure optimization. As a result, no convergence in the structure optimization was achieved within 200 optimization steps.
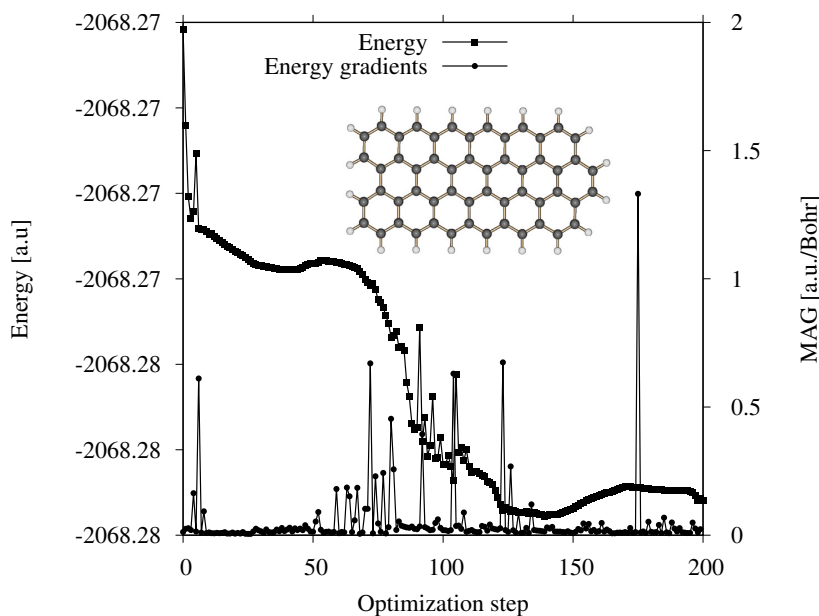

Figure B.1: Total energy [a.u.] and maximum absolute gradient (MAG) component [a.u./Bohr] convergence of the $C_{54}H_{20}$ computed using the original default setting for the asymptotic atomic radii for far-field ERIs.

At this point it is important to note that changing the ERI setting to DIRECT [76], i.e. treating all ERIs as near-field ERIs, yields a smooth structure convergence for $C_{54}H_{20}$. Therefore, we conclude that the far-field ERIs are the reason for the erratic behavior of the MAG component in the structure optimization. Closer inspection revealed that the standard setting for the asymptotic atomic radii is problematic for variational fitted Fock gradients. A straightforward solution is to double these radii for Fock gradients. Fig B.2 shows energy and MAG convergence for the $C_{54}H_{20}$ structure optimization with these doubled asymptotic radii. As this figure shows a smooth structure optimization reaching convergence within 35 geometry steps is now obtained. This optimization is very similar to the one obtained with the ERIs DIRECT setting. Therefore, we established this setting of asymptotic radii as new default in deMon2k.
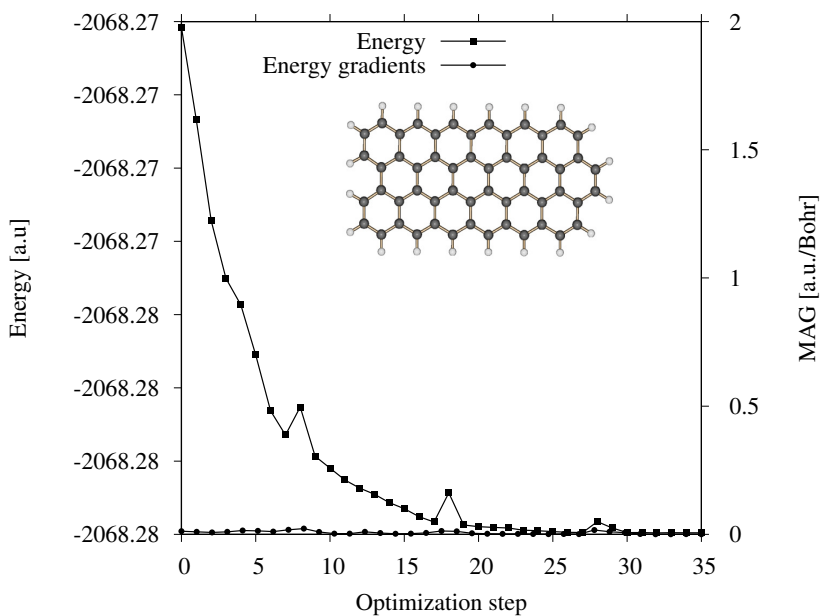

Figure B.2: Total energy [a.u.] and maximum absolute gradient (MAG) [a.u./Bohr] component convergence of the $C_{54}H_{20}$ computed with doubled asymptotic atomic radii for the far-field ERI derivatives.

Serial and Parallel Timing Tables

Table C.1: Serial and parallel timings per SCF cycle [s] for the SCF iteration and the Fock potential calculation along with the corresponding parallel speedup factors, S_p. The entries are ordered according to the number of basis functions, N_{bas}, in the benchmarks systems. The Fock exchange contributions were calculated with the combination of Cholesky decomposition and TED for the inversion of the local Coulomb matrix, $\mathbf{G}_i$, for each LMO.

	N_{bas}	SCF Serial	SCF Parallel	S_p	Fock potential Serial	Fock potential Parallel	S_p
Alkane chains	680	30.8	2.0	15.4	24.1	1.4	17.4
	1980	195.0	12.3	15.9	152.0	8.5	17.9
	3280	384.2	26.7	14.4	291.8	16.9	17.3
	4580	599.2	55.8	10.7	438.8	26.7	16.4
	5880	854.2	100.2	8.5	599.3	38.4	15.6
	7180	1043.4	152.3	6.9	686.9	47.0	14.6
	8480	1371.5	236.7	5.8	869.2	65.0	13.4
	9780	1748.5	343.4	5.1	1062.3	86.6	12.3
Amylose fragments	600	32.8	2.2	15.1	25.5	1.5	17.0
	1135	156.7	9.3	16.8	124.1	6.6	18.8
	2205	612.6	34.6	17.7	488.3	24.7	19.8
	4345	1823.2	112.0	16.3	1373.8	70.5	19.5
	8625	6954.0	533.7	13.0	5528.3	310.7	17.8
Graphene sheets	1150	185.2	16.1	11.5	144.4	11.9	12.2
	1670	631.8	57.2	11.0	488.4	42.9	11.4
	2190	1415.1	138.4	10.2	1045.6	91.0	11.5
	2710	2705.0	271.4	10.0	1985.2	181.6	10.9
	3230	5997.0	685.4	8.7	4618.0	516.5	8.9

Table C.2: Serial and parallel timings per SCF cycle [s] for the SCF iteration and the Fock potential calculation along with the corresponding parallel speedup factors, S_p. The entries are ordered according to the number of basis functions, N_{bas}, in the benchmarks systems. The Fock exchange contributions were calculated using the Eq. (4.25) which employs the modified Cholesky decomposition.

	N_{bas}	SCF Serial	SCF Parallel	S_p	Fock potential Serial	Fock potential Parallel	S_p
Alkane chains	680	28.5	1.8	15.7	22.2	1.2	17.8
	1980	187.4	11.7	16.0	145.6	8.0	18.1
	3280	370.4	25.7	14.4	280.1	16.3	17.2
	4580	584.0	54.2	10.8	427.0	25.8	16.6
	5880	824.0	98.9	8.3	575.8	37.0	15.6
	7180	1004.3	150.0	6.7	657.4	45.7	14.4
	8480	1281.1	229.6	5.6	807.6	62.8	12.9
	9780	1560.4	344.6	4.5	942.2	86.1	10.9
Amylose fragments	600	29.1	1.8	16.0	22.8	1.3	18.1
	1135	145.4	8.2	17.8	117.0	6.1	19.2
	2205	588.6	31.5	18.7	475.0	23.7	20.0
	4345	1721.5	105.6	16.3	1312.4	68.3	19.2
	8625	6111.5	522.7	11.7	4831.4	307.9	15.7
Graphene sheets	1150	149.5	8.7	17.1	120.3	6.6	18.3
	1670	440.1	24.8	17.7	358.5	19.2	18.7
	2190	940.7	52.4	18.0	747.4	39.7	18.8
	2710	1612.0	91.9	17.5	1286.2	70.3	18.3
	3230	3643.7	209.9	17.4	3040.0	169.9	17.9

Bibliography

[1] P. Hohenberg and W. Kohn, *Phys. Rev.* **136**, B864 (1964).

[2] W. Kohn and L. J. Sham, *Phys. Rev.* **140**, A1133 (1965).

[3] M. Casida, "Time-dependent density-functional response theory for molecules", in *Recent Advances in Density Functional Methods (Part I)*, Vol. 1, edited by D. P. Chong (World Scientific, 1995) Chap. 5, pp. 155–192.

[4] A. M. Köster, J. U. Reveles, and J. M. del Campo, *J. Chem. Phys.* **121**, 3417 (2004).

[5] P. Calaminici, A. Álvarez-Ibarra, D. Cruz-Olvera, V.-D. Domínguez-Soria, R. Flores-Moreno, G. U. Gamboa, G. Geudtner, A. Goursot, D. Mejía-Rodríguez, D. R. Salahub, B. Zuñiga Gutierrez, and A. M. Köster, "Auxiliary Density Functional Theory: From Molecules to Nanostructures", in *Handbook of Computational Chemistry*, edited by J. Leszczynski, A. Kaczmarek-Kedziera, T. Puzyn, M. G. Papadopoulos, H. Reis, and M. K. Shukla (Springer International Publishing, Cham, 2017), pp. 795–860.

[6] V. D. Dominguez-Soria, P. Calaminici, and A. Goursot, *J. Chem. Phys.* **127**, 154710 (2007).

[7] P. Calaminici, G. Geudtner, and A. M. Köster, *J. Chem. Theory Comput.* **5**, 29 (2009).

[8] B. Champagne, E. A. Perpète, S. J. A. van Gisbergen, E.-J. Baerends, J. G. Snijders, C. Soubra-Ghaoui, K. A. Robins, and B. Kirtman, *J. Chem. Phys.* **109**, 10489 (1998).

[9] S. J. A. van Gisbergen, P. R. T. Schipper, O. V. Gritsenko, E. J. Baerends, J. G. Snijders, B. Champagne, and B. Kirtman, *Phys. Rev. Lett.* **83**, 694 (1999).

[10] N. N. Matsuzawa, A. Ishitani, D. A. Dixon, and T. Uda, *J, Phys, Chem. A* **105**, 4953 (2001).

[11] M. E. Casida and D. R. Salahub, *J. Chem. Phys.* **113**, 8918 (2000).

[12] H. Appel, E. K. U. Gross, and K. Burke, Phys. Rev. Lett. **90**, 043005 (2003).

[13] A. Dreuw, J. L. Weisman, and M. Head-Gordon, *J. Chem. Phys.* **119**, 2943 (2003).

[14] H. Sekino, Y. Maeda, M. Kamiya, and K. Hirao, *J. Chem. Phys.* **126**, 014107 (2007).

[15] D. Jacquemin, E. A. Perpète, M. Medved, G. Scalmani, M. J. Frisch, R. Kobayashi, and C. Adamo, *J. Chem. Phys.* **126**, 191108 (2007).

[16] D. Jacquemin, E. A. Perpète, O. A. Vydrov, G. E. Scuseria, and C. Adamo, *J. Chem. Phys.* **127**, 094102 (2007).

[17] J. R. Hammond, N. Govind, K. Kowalski, J. Autschbach, and S. S. Xantheas, *J. Chem. Phys.* **131**, 214103 (2009).

[18] Y. Tawada, T. Tsuneda, S. Yanagisawa, T. Yanai, and K. Hirao, *J. Chem. Phys.* **120**, 8425 (2004).

[19] R. J. Bartlett and M. Musiał, *Rev. Mod. Phys.* **79**, 291 (2007).

[20] P. Verma, A. Perera, and R. J. Bartlett, *Chem. Phys. Lett.* **524**, 10 (2012).

[21] J. Gerratt and I. M. Mills, *J. Chem. Phys.* **49**, 1719 (1968).

[22] S. P. Karna and M. Dupuis, *J. Comput. Chem.* **12**, 487 (1991).

[23] R. Flores-Moreno and A. M. Köster, *J. Chem. Phys.* **128**, 134105 (2008).

[24] J. Carmona-Espíndola, R. Flores-Moreno, and A. M. Köster, *J. Chem. Phys.* **133**, 084102 (2010).

[25] J. Carmona-Espíndola, R. Flores-Moreno, and A. M. Köster, *Int. J. Quantum Chem.* **112**, 3461.

[26] D. Mejía-Rodríguez, R. I. Delgado-Venegas, P. Calaminici, and A. M. Köster, *J. Chem. Theory Comput.* **11**, 1493 (2015).

[27] B. I. Dunlap, J. W. D. Connolly, and J. R. Sabin, *J. Chem. Phys.* **71**, 4993 (1979).

[28] J. W. Mintmire and B. I. Dunlap, *Phys. Rev. A* **25**, 88 (1982).

[29] J. W. Mintmire, J. R. Sabin, and S. B. Trickey, *Phys. Rev. B* **26**, 1743 (1982).

[30] E. Schwegler, M. Challacombe, and M. Head-Gordon, *J. Chem. Phys.* **106**, 9708 (1997).

[31] C. Ochsenfeld, C. A. White, and M. Head-Gordon, *J. Chem. Phys.* **109**, 1663 (1998).

[32] R. Polly, H.-J. Werner, F. Manby, and P. Knowles, *Mol. Phys.* **102**, 2311 (2004).

[33] A. Sodt and M. Head-Gordon, *J. Chem. Phys.* **128**, 104106 (2008).

[34] D. Mejía-Rodríguez and A. Köster, *J. Chem. Phys.* **141**, 124114 (2014).

[35] S. Manzer, E. Epifanovsky, and M. Head-Gordon, *J. Chem. Theory Comput.* **11**, 518 (2015).

[36] R. Kendall and H. Früchtl, *Theor. Chem. Acc.* **97**, 158 (1997).

[37] S. Hamel, M. Casida, and D. Salahub, *J. Chem. Phys.* **114**, 7342 (2001).

[38] F. Weigend, *Phys. Chem. Chem. Phys.* **4**, 4285 (2002).

[39] A. M. Köster, *J. Chem. Phys.* **104**, 4114 (1996).

[40] A. M. Köster, *J. Chem. Phys.* **118**, 9943 (2003).

[41] A. Alvarez-Ibarra and A. M. Köster, *J. Chem. Phys.* **139**, 024102 (2013).

[42] J. Zheng, Y. Zhao, and D. G. Truhlar, *J. Chem. Theory Comput.* **5**, 808 (2009).

[43] D. Mejía-Rodríguez, X. Huang, J. M. del Campo, and A. M. Köster, "Hybrid Functionals with Variationally Fitted Exact Exchange", in *Concepts of Mathematical Physics in Chemistry: A Tribute to Frank E. Harris - Part A*, Vol. 71, edited by J. R. Sabin and R. Cabrera-Trujillo, Advances in Quantum Chemistry (Academic Press, 2015) Chap. 4, pp. 41–67.

[44] V. Guner, K. S. Khuong, A. G. Leach, P. S. Lee, M. D. Bartberger, and K. N. Houk, *J. Phys. Chem. A* **107**, 11445 (2003).

[45] M. Van den Bossche, N. M. Martin, J. Gustafson, C. Hakanoglu, J. F. Weaver, E. Lundgren, and H. Grönbeck, *J. Chem. Phys.* **141**, 034706 (2014).

[46] M. Born and P. Jordan, *Z. Physik* **34**, 858 (1925).

[47] D. Hilbert, J. v. Neumann, and L. Nordheim, *Math. Ann.* **98**, 1 (1928).

[48] M. Born and R. Oppenheimer, *Annalen der Physik* **389**, 457 (1927).

[49] L. H. Thomas, *Math. Proc. Camb. Philos. Soc.* **23**, 542 (1927).

[50] E. Fermi, *Rend. Accad. Naz. Lincei,* 602 (1927).

[51] P. A. M. Dirac, *Math. Proc. Camb. Philos. Soc.* **26**, 376385 (1930).

[52] E. Wigner and F. Seitz, *Phys. Rev.* **43**, 804 (1933).

[53] E. Teller, *Rev. Mod. Phys.* **34**, 627 (1962).

[54] J. Slater and K. Johnson, *Phys. Rev. B* **5**, 844 (1972).

[55] S. H. Vosko, L. Wilk, and M. Nusair, *Can. J. Phys.* **58**, 1200 (1980).

[56] A. D. Becke, *Phys. Rev. A* **38**, 3098 (1988).

[57] C. Lee, W. Yang, and R. G. Parr, *Phys. Rev. B* **37**, 785 (1988).

[58] J. Perdew, K. Burke, and M. Ernzerhof, *Phys. Rev. Lett.* **77**, 3865 (1996).

[59] S. K. Ghosh and R. G. Parr, *Phys. Rev. A* **34**, 785 (1986).

[60] A. D. Becke and M. R. Roussel, *Phys. Rev. A* **39**, 3761 (1989).

[61] J. Sun, A. Ruzsinszky, and J. P. Perdew, *Phys. Rev. Lett.* **115**, 036402 (2015).

[62] J. Sun, R. C. Remsing, Y. Zhang, Z. Sun, A. Ruzsinszky, H. Peng, Z. Yang, A. Paul, U. Waghmare, X. Wu, M. L. Klein, and J. P. Perdew, *Nat. Chem.* **8**, 831 (2016).

[63] R. Sharp and G. Horton, *Phys. Rev.* **90**, 317 (1953).

[64] J. Talman and W. Shadwick, *Phys. Rev. A* **14**, 36 (1976).

[65] J. B. Krieger, Y. Li, and G. J. Iafrate, *Phys. Rev. A* **45**, 101 (1992).

[66] J. B. Krieger, Y. Li, and G. J. Iafrate, *Phys. Rev. A* **46**, 5453 (1992).

[67] M. Betzinger, C. Friedrich, S. Blügel, and A. Görling, *Phys. Rev. B* **83**, 045105 (2011).

[68] M. Betzinger, C. Friedrich, A. Görling, and S. Blügel, *Phys. Rev. B* **85**, 245124 (2012).

[69] S. Kurth and J. P. Perdew, *Int. J. Quantum Chem.* **77**, 814 (2000).

[70] C. C. J. Roothaan, *Rev. Mod. Phys.* **23**, 69 (1951).

[71] C. C. J. Roothaan, *Rev. Mod. Phys.* **32**, 179 (1960).

[72] A. Köster, G. Geudtner, A. Álvarez-Ibarra, P. Calaminici, M. Casida, J. Carmona-Espíndola, V. Domínguez, R. Flores-Moreno, G. Gamboa, A. Goursot, T. Heine, A. Ipatov, A. de la Lande, F. Janetzko, J. del Campo, D. Mejía-Rodríguez, J. U. Reveles, J. Vásquez-Pérez, A. Vela, B. Zuniga-Gutierrez, and D. Salahub, *deMon2k*, The Intenational deMon Developers, Cinvestav, México. Version 6.0, 2018.

[73]   H. Sambe and R. Felton, *J. Chem. Phys.* **62**, 1122 (1975).

[74]   M. E. Casida, C. Daul, A. Goursot, A. M. Köster, L. G. M. Pettersson, E. Proynov, A. St-Amant, D. R. Salahub, H. Duarte, N. Godbout, J. Guan, C. Jamorski, M. Leboeuf, V. Malkin, O. Malkina, F. Sim, and A. Vela, *deMonKS*, The deMon software, Montreal, Canada, Version 3.4, 2006.

[75]   A. Alvarez-Ibarra, "Asymptotic Expansion of Molecular Integrals in Self-Consistent Auxiliary Density Functional Methods", PhD thesis (Cinvestav, 2013).

[76]   A. M. Köster, G. Geudtner, G. U. Gamboa, A. Alvarez-Ibarra, P. Calaminici, R. Flores-Moreno, A. Goursot, A. de la Lande, D. Mejia-Rodriguez, T. Mineva, L. G. M. Pettersson, J. M. Vasquez-Perez, and B. Zuniga-Gutierrez, *The deMon User' Guide*, Version 5.0, Edited by S.B. Trickey and D.R. Salahub (Cinvestav, Mexico, 2018).

[77]   W. H. Press, S. A. Teukolsky, W. T. Vetterling, and B. P. Flannery, *Numerical Recipes in FORTRAN; The Art of Scientific Computing*, 2nd (Cambridge University Press, New York, NY, USA, 1993).

[78]   J. N. Pedroza-Montero, J. L. Morales, A. Alvarez-Ibarra, P. Calaminici, and A. M. Köster, *J. Chem. Theory Comput.* under revision.

[79]   V. Fock, *Zeitschrift für Physik* **61**, 126 (1930).

[80]   D. Mejía-Rodríguez, "Low-Order Scaling Methods for Auxiliary Density Functional Theory", PhD thesis (Cinvestav, 2015).

[81]   F. Aquilante, T. Pedersen, A. Merés, and H. Koch, *J. Chem. Phys.* **125**, 174101 (2006).

[82]   S. F. Boys, *Rev. Mod. Phys.* **32**, 296 (1960).

[83]   J. M. Foster and S. F. Boys, *Rev. Mod. Phys.* **32**, 300 (1960).

[84]   B. Zuniga-Gutierrez and A. M. Köster, *Mol. Phys.* **114**, 1026 (2016).

[85]   V. D. Domínguez-Soria, G. Geudtner, J. L. Morales, P. Calaminici, and A. M. Köster, *J. Chem. Phys.* **131**, 124102 (2009).

[86]   A. Savin, "On degeneracy, near-degenaracy and density functional theory", in *Recent Developments and Applications of Modern Density Functional Theory*, Vol. 4, edited by J. M. Seminario, Theoretical and Computational Chemistry (Elsevier, 1996) Chap. 9, pp. 327–357.

[87]   H. Iikura, T. Tsuneda, T. Yanai, and K. Hirao, *J. Chem. Phys.* **150**, 3540 (2001).

[88]   T. Yanai, D. P. Tew, and N. C. Handy, *Chem. Phys. Lett.* **393**, 51 (2004).

[89]   P. Verma and R. J. Bartlett, *J. Chem. Phys.* **140**, 18A534 (2014).

[90]   Y. Jin and R. J. Bartlett, *J. Chem. Phys.* **145**, 034107 (2016).

[91]   A. J. Cohen, P. Mori-Sánchez, and W. Yang, *J. Chem. Phys.* **126**, 191109 (2007).

[92]   M. A. Rohrdanz and J. M. Herbert, *J. Chem. Phys.* **129**, 034107 (2008).

[93]   M. A. Rohrdanz, K. M. Martins, and J. M. Herbert, *J. Chem. Phys.* **130**, 054112 (2009).

[94]   J. Heyd, G. E. Scuseria, and M. Ernzerhof, *J. Chem. Phys.* **118**, 8207 (2003).

[95]   J. Heyd, G. E. Scuseria, and M. Ernzerhof, *J. Chem. Phys.* **124**, 219906 (2006).

[96]   A. V. Krukau, O. A. Vydrov, A. F. Izmaylov, and G. E. Scuseria, *J. Chem. Phys.* **125**, 224106 (2006).

[97]   U. Reveles, "Geometry Optimization in LCGTO-DFT Methods with Auxiliary Functions", PhD thesis (Cinvestav, 2004).

[98]   J. M. del Campo, "Exploring Chemical Reactivity With Auxiliary Density Functional Theory", PhD thesis (Cinvestav, 2008).

[99]   P. Pulay, *Mol. Phys.* **17**, 197 (1969).

[100] R. McWeeny, *Phys. Rev.* **126**, 1028 (1962).

[101] G. Diercksen and R. McWeeny, *J. Chem. Phys.* **44**, 3554 (1966).

[102] R. McWeeny and G. Diercksen, *J. Chem. Phys.* **49**, 4852 (1968).

[103] T. Eirola and O. Nevanlinna, *Linear Algebra Appl.* **121**, 511 (1989).

[104] U. M. Yang and K. A. Gallivan, *Appl. Numer. Math.* **19**, 287 (1995).

[105] E. Besalú and R. Carbó-Dorca, *J. Math. Chem.* **49**, 1769 (2011).

[106] F. A. Delesma, G. Geudtner, D. Mejía-Rodríguez, P. Calaminici, and A. M. Köster, *J. Chem. Theory Comput.* **14**, 5608 (2018).

[107] C. Köppl and H.-J. Werner, *J. Chem. Theory Comput.* **12**, 3122 (2016).

[108] N. J. Higham, "Cholesky Factorization", in *Accuracy and Stability of Numerical Algorithms* (Society for Industrial and Applied Mathematics, 2002) Chap. 10, pp. 195–212.

[109] S. H. Cheng and N. J. Higham, *SIAM J. Matrix Anal. Appl.* **19**, 1097 (1998).

[110] C. Ashcraft, R. G. Grimes, and J. G. Lewis, *SIAM J. Matrix Anal. Appl.* **20**, 513 (1998).

[111] N. J. Higham, *Linear Algebra Its Appl.* **103**, 103 (1988).

[112] J. N. Pedroza-Montero, "Iterative Density Fitting for ab-initio Nanoscale Simulations", PhD thesis (Cinvestav, in preparation).

[113] E. Anderson, Z. Bai, C. Bischof, S. Blackford, J. Demmel, J. Dongarra, J. Du Croz, A. Greenbaum, S. Hammarling, A. McKenney, and D. Sorensen, *LAPACK users' guide*, Third (Society for Industrial and Applied Mathematics, Philadelphia, PA, 1999).

[114] F. Weigend and R. Ahlrichs, *Phys. Chem. Chem. Phys.* **7**, 3297 (2005).

[115] P. Calaminici, F. Janetzko, A. M. Köster, R. Mejía-Olvera, and B. Zuñiga-Gutierrez, *J. Chem. Phys.* **126**, 044108 (2007).

[116] L. A. Curtiss, K. Raghavachari, P. C. Redfern, and J. A. Pople, *J. Chem. Phys.* **106**, 1063 (1997).

[117] L. A. Curtiss, P. C. Redfern, K. Raghavachari, and J. A. Pople, *J. Chem. Phys.* **109**, 42 (1998).

[118] L. A. Curtiss, K. Raghavachari, P. C. Redfern, V. Rassolov, and J. A. Pople, *J. Chem. Phys.* **109**, 7764 (1998).

[119] L. A. Curtiss, K. Raghavachari, P. C. Redfern, and J. A. Pople, *J. Chem. Phys.* **112**, 7374 (2000).

[120] M. Valiev, E. Bylaska, N. Govind, K. Kowalski, T. Straatsma, H. J. J. Van Dam, W. D., J. Nieplocha, E. Apra, T. Windus, and W. de Jong, *Comput. Phys. Commun.* **181**, 1477 (2010).

[121] M. E. Mura and P. J. Knowles, *J. Chem. Phys.* **104**, 9848 (1996).

[122] A. D. Becke, *J. Chem. Phys.* **88**, 2547 (1988).

[123] W. M. Haynes, D. R. Lide, and T. J. Bruno, *CRC handbook of chemistry and physics: a ready-reference book of chemical and physical data* (CRC Press, Boca Raton, Florida, 2016).

[124] A. S. Karne, N. Vaval, S. Pal, J. M. Vásquez-Pérez, A. M. Köster, and P. Calaminici, *Chem. Phys. Lett.* **635**, 168 (2015).

[125] A. S. Karne, N. Vaval, S. Pal, J. M. Vásquez-Pérez, A. M. Köster, and P. Calaminici, *Chem. Phys. Lett.* **636**, 228 (2015).

[126] M. J. Frisch, G. W. Trucks, H. B. Schlegel, G. E. Scuseria, M. A. Robb, J. R. Cheeseman, G. Scalmani, V. Barone, G. A. Petersson, H. Nakatsuji, X. Li, M. Caricato, A. Marenich, J. Bloino, B. G. Janesko, R. Gomperts, B. Mennucci, H. P. Hratchian, J. V. Ortiz, A. F. Izmaylov, J. L. Sonnenberg, D. Williams-Young, F. Ding, F. Lipparini, F. Egidi, J. Goings, B. Peng, A. Petrone, T. Henderson, D. Ranasinghe, V. G. Zakrzewski, N. R. J. Gao, G. Zheng, W. Liang, M. Hada, M. Ehara, K. Toyota, R. Fukuda, J. Hasegawa, M. Ishida, T. Nakajima, Y. Honda, O. Kitao, H. Nakai, T. Vreven, K. Throssell, J. A. M. Jr., J. E. Peralta, F. Ogliaro, M. Bearpark, J. J. Heyd, E. Brothers, K. N. Kudin, V. N. Staroverov, T. Keith, R. Kobayashi, K. R. J. Normand, A. Rendell, J. C. Burant, S. S. Iyengar, J. Tomasi, M. Cossi, J. M. Millam, M. Klene, C. Adamo, R. Cammi, J. W. Ochterski, R. L. Martin, K. Morokuma, O. Farkas, J. B. Foresman, and D. J. Fox, *Gaussian 09*, Gaussian, Inc., Wallingford CT, 2016.

[127] H. A. Kurtz, J. J. P. Stewart, and K. M. Dieter, *J. Comput. Chem.* **11**, 82 (1990).

[128] P. Calaminici, K. Jug, and A. M. Köster, *J. Chem. Phys.* **109**, 7756 (1998).

[129] R. A. Kendall, T. H. J. Dunning, and R. J. Harrison, *J. Chem. Phys.* **96**, 6796 (1992).

[130] J. M. del Campo and A. M. Köster, *J. Chem. Phys.* **129**, 024107 (2008).

[131] J. M. Bofill, *J. Comput. Chem.* **15**, 1 (1994).

[132] P. Culot, G. Dive, V. H. Nguyen, and J. M. Ghuysen, *Theoret. Chim. Acta* **82**, 189 (1992).

[133] K. Fukui, *Acc. Chem. Res.* **14**, 363 (1981).

[134] P. C. Hariharan and J. A. Pople, *Theoret. Chim. Acta* **28**, 213 (1973).

[135] T. H. Dunning, *J. Chem. Phys.* **90**, 1007 (1989).

[136] J. R. Gómez-Pérez, F. A. Delesma, P. Calaminici, and A. M. Köster, *J. Mol. Model.* **24**, 223 (2018).

[137] S. E. Pérez-Figueroa, P. Calaminici, and A. M. Köster, *J. Phys. Chem. A* **123**, 4565 (2019).

[138] O. Diels and K. Alder, *Justus Liebigs Ann. Chem.* **460**, 98 (1928).

[139] H. Kroto, S. O. J.R. Heath, R. Curl, and R. Smalley, *Nature* **318**, 162 (1985).

[140] H. W. Kroto, A. W. Allaf, and S. P. Balm, *Chem. Rev.* **91**, 1213 (1991).

[141] S. Iijima, *Nature* **354**, 56 (1991).

[142] K. Hedberg, L. Hedberg, D. S. Bethune, C. A. Brown, D. H. C., R. Johnson, and M. de Vries, *Science* **254**, 410 (1991).

[143] S. Liu, Y.-J. Lu, M. M. Kappes, and J. A. Ibers, *Science* **254**, 408 (1991).

[144] L. S. K. Pang and M. A. Wilson, *J. Phys. Chem.* **97**, 6761 (1993).

[145] L. M. Giovane, J. W. Barco, T. Yadav, A. L. Lafleur, J. A. Marr, J. B. Howard, and V. M. Rotello, *J. Phys. Chem.* **97**, 8560 (1993).

[146] T. Yang, R. Fukuda, R. Cammi, and M. Ehara, *J. Phys. Chem. A* **121**, 4363 (2017).

[147] S. Osuna, J. Morera, M. Cases, K. Morokuma, and M. Solà, *J. Phys. Chem. A* **113**, 9721 (2009).

[148] W. Śliwa, *Fullerene Sci. and Technol.* **5**, 1133 (1997).

[149] G. H. Sarova and M. N. Berberan-Santos, *Chem. Phys. Lett.* **397**, 402 (2004).

[150] J. Mestres, M. Duran, and M. Solà, *J. Phys. Chem.* **100**, 7449 (1996).

[151] Y. Zhao and D. G. Truhlar, *Theor. Chem. Acc.* **120**, 215 (2008).

[152] E. Heid, A. Szabadi, and C. Schröder, *Phys. Chem. Chem. Phys.* **20**, 10992 (2018).

[153] R. R. Zope, T. Baruah, M. R. Pederson, and B. I. Dunlap, *Int. J. Quantum Chem.* **108**, 307 (2008).

[154] S. A. McDowell, R. D. Amos, and N. C. Handy, *Chem. Phys. Lett.* **235**, 1 (1995).

[155] A. J. Perkins, *J. Phys. Chem.* **68**, 654 (1964).

[156] M. A. Spackman, *J. Phys. Chem.* **93**, 7594 (1989).

[157] N. J. Bridge, A. D. Buckingham, and J. W. Linnett, *Proc. R. Soc. of London Ser. A* **295**, 334 (1966).

[158] W. F. Murphy, *J. Chem. Phys.* **67**, 5877 (1977).

[159] K. Siegbahn, C. Nordling, A. Fahlman, R. Nordberg, K. Hamrin, J. Hedman, G. Johansson, T. Bergmark, S.-E. Karlsson, I. Lindgren, and B. Lindberg, *ESCA, Atomic, Molecular and Solid State Structure Studied by Means of Electron Spectroscopy* (Almqvist and Wiksell, Uppsala, 1967).

[160] O. Travnikova, K. J. Børve, M. Patanen, J. Söderström, C. Miron, L. J. Sæthre, N. Mårtensson, and S. Svensson, *J. El. Spec. Rel. Phenom.* **185**, 191 (2012).

[161] N. Måtensson and A. Nilsson, *J. El. Spec. Rel. Phenom.* **75**, 209 (1995).

[162] D. Andrae, U. Häußermann, M. Dolg, H. Stoll, and H. Preuß, *Theor. Chim. Acta* **77**, 123 (1990).

[163] M. E. Defonsi Lestard, M. E. Tuttolomondo, E. L. Varetti, D. A. Wann, H. E. Robertson, D. W. H. Rankin, and A. Ben Altabef, *J. Raman Spectrosc.* **40**, 2053 (2009).

[164] F. A. Delesma, M. VandenBossche, H. Grönbeck, P. Calaminici, A. M. Köster, and L. G. M. Pettersson, *ChemPhysChem* **19**, 169 (2018).

[165] B. Zuniga-Gutierrez, G. Geudtner, and A. M. Köster, *J. Chem. Phys.* **134**, 124108 (2011).

[166] J. N. Pedroza-Montero, F. A. Delesma, R. I. Delgado-Venegas, P. Calaminici, and A. M. Köster, *Theor. Chem. Acc.* **135**, 230 (2016).

[167] S. Bochner (Princeton University Press, title = Lectures on Fourier Integrals, 1959).

[168] T. H. Thompson and C. Ochsenfeld, *J. Chem. Phys.* **147**, 144101 (2017).